NANODIAMOND MACROELECTRODES AND ULTRAMICROELECTRODE ARRAYS FOR BIO-ANALYTE DETECTION

By

Supil Raina

Dissertation

Submitted to the Faculty of the

Graduate School of Vanderbilt University

in partial fulfillment of the requirements

for the degree of

DOCTOR OF PHILOSOPHY

in

Interdisciplinary Materials Science

December, 2011

Nashville, Tennessee

Approved:

Professor Weng P. Kang

Professor Jimmy L. Davidson

Professor Sharon M. Weiss

Professor Bharat L. Bhuva

Professor Deyu Li

To my loving wife Angela,

To my dearest parents, Mr. Surrinder and Mrs.Santosh Raina and sister, Sunhali

ACKNOWLEDGEMENTS

I would first like to thank and express my deepest gratitude to my advisor and mentor, Dr. Weng Poo Kang, for providing me an opportunity to perform this research and complete my graduate studies at Vanderbilt University. He has been instrumental in my growth as a scientist and a human being; he has been a source of inspiration and always provided motivation to excel. I would like to thank Dr. Jim Davidson for his support and encouragement; and for providing fresh insight to further enhance my dissertation.

I would also like to thank Professors Bharat Bhuva, Deyu Li and Sharon Weiss for serving on my PhD committee and providing valuable technical suggestions. In addition, I am thankful to all my present and ex-colleagues and faculty members associated with the Vanderbilt Diamond Microelectronics group for their help and support throughout my graduate studies: Dr. William Hofmeister, Dr. Bo Choi, Mick Howell, Dr. Patrick Taylor, Dr. Karthik Subramanian, Dr. Yong Mui Wong, Dr. Siyu Wei, Dr. Puteri Hamari, Rohit Takalkar, Nikkon Ghosh, Shao-Hua Hsu, William Paxton, Serkan Akbulut and Mesut Yilmaz. I also want to acknowledge the support provided, since my first day at Vanderbilt University, by Sarah Ross-Satterwhite, Program Coordinator of the Materials Science program and Lauren Fox, for her help with logistics and administrative responsibilities.

Finally, I would like to thank the Graduate School for their financial support, especially the Travel Grants which enabled me to participate and present my research work at various scientific forums. Also, I must express my gratitude to the Department of Defense for their research grants that allowed me to complete my graduate studies.

TABLE OF CONTENTS

LIST OF TABLES

LIST OF FIGURES

LIST OF SYMBOLS

α ..... Charge transfer coefficient

ΔE_p ..... Peak-peak separation

φ ..... Work function

ν..... Scan Rate

ϑ..... Frequency of incident x-ray

A..... Active area of the electrode

Ar ..... Argon

Au..... Gold

C..... Concentration

C_d..... Differential Capacitance

CH_4..... Methane

Cr(VI)..... Hexavalent Chromium

D..... Diffusion coefficient

E'^{o}..... Formal redox potential

E_B ..... Electron Binding Energy

eV ..... Electron Volt

F ..... Faraday's constant

$Fe(CN)_6^{3-/4-}$ ..... Ferri/Ferrocyanide redox couple

h..... Planck's constant

H_2 ..... Hydrogen

HF ..... Hydrogen Fluoride

H_2O_2 ..... Hydrogen Peroxide

i_c ..... Capacitive current

i_p ..... Peak Faradaic current

Ir ..... Iridium

$IrCl_6^{-2/-3}$ ..... Iridium Hexachloride

iR_u or iR ..... Potential drop due to uncompensated solution resistance

K_a ..... Acid dissociation constant

k^o_{app} ..... Apparent Rate Constant

KCl ..... Potassium Chloride

K_2HPO_4 ..... Potassium Phosphate

m_e ..... mass of electron

n ..... Number of electrons transferred

nA ..... Nano Amperes

NaCl ..... Sodium Chloride

Na_2HPO_4 ..... Sodium Phosphate

NO ..... Nitric Oxide

O_2 ..... Oxygen

pA ..... Pico Amperes

Pt ..... Platinum

q(t) ..... Charge as function of time

R ..... Gas constant

RC ..... Resistance- Capacitance, Time Constant

$Ru(NH_3)_6^{+2/+3}$ ..... Ruthenium Hexamine

Si ..... Silicon

SiO_2 ..... Silicon Dioxide

Si_3N_4 ..... Silicon Nitride

τ ..... Time constant

v ..... Electron velocity

LIST OF ABBREVIATIONS

3D..... Three- Dimensional

AA..... Ascorbic Acid

BDD..... Boron doped diamond

CA..... Chronoamperometry

CV..... Cyclic Voltammogram or Cyclic Voltammetry

CNS..... Central Nervous System

CNT..... Carbon Nano Tube

COMT..... catechol-O-methyltransferase

CSF..... Cerebrospinal Fluid

DA..... Dopamine

DAC..... Dopaminechrome

DAQ..... Dopamine-o-quinone

DHA..... Dehydroascorbate

DHPG..... 3,4-dihydroxyphenylglycol

DOPAC..... 3,4- dihydroxyphenylacetic acid (Dopamine metabolite)

DPV..... Differential Pulse Voltammetry

EPI..... Epinephrine

FSCV..... Fast Scan Cyclic Voltammetry

HVA..... Homovanillic Acid

IDA..... Interdigitated Electrode Array

IR..... Infra-Red

LDAC..... Leucodopaminechrome

L-DOPA..... 3,4-dihydroxyphenylalanine (Dopamine precursor)

L.O.D. ..... Limit of Detection

MAO ..... monoamine oxidase

MEA ..... Microelectrode Array

MHPG 3-methoxy-4-hydroxyphenylglycol

MWCNT ..... Multi Walled Carbon Nano Tube

NE ..... Norepinephrine

PBS ..... Phosphate Buffered Saline

PECVD ..... Plasma Enhanced Chemical Vapor Deposition

RC ..... Resistance- Capacitance, Time Constant

RF ..... Radio Frequency

RIE ..... Reactive Ion Etch

rpm ..... Revolutions per minute

SAM ..... Self Assembled Monolayer

sccm ..... Standard cubic centimeter per minute

SEM ..... Scanning Electron Microscope

SOG ..... Spin On Glass

S/N ..... Signal to Noise Ratio

3D ..... Three- Dimensional

UA ..... Uric Acid

UMEA ..... Ultramicroelectrode Array

UV ..... Ultra-violet

XPS ..... X-Ray Photoelectron Spectroscopy

CHAPTER I

INTRODUCTION

1.1 Thin film Diamond

Carbon is the most commonly used electrode material for electroanalytical chemistry [1,2]. It is available in a variety of forms: graphite, glassy carbon, carbon fiber, nanotubes, and amorphous powders. These traditional carbon electrodes are important in electrochemistry because of low cost, simple preparation methods, possibility of achieving large surface area, and a relatively wide potential window of water stability [1,2]. Despites these advantages, they have several drawbacks such as fouling due to surface adsorption limiting their long term stability, inability to detect compounds that oxidize at high anodic potentials, not suitable for use in aggressive environments [1,2].

Another carbon allotrope, diamond, specifically conductive diamond films, has found wide-spread use as an electrode material due to superior properties such as [1,2]:

a) Low and stable background current over wide potential range.
b) Wide working potential window in aqueous media.
c) Relatively rapid electron-transfer kinetics for several redox systems without any conventional pretreatment.
d) Weak molecular adsorption.
e) Dimensional stability and corrosion resistance.

1.2 Cyclic Voltammetry

Electroanalysis involves the measurement of an electrical signal (e.g., potential, current, or charge) associated with the oxidation or reduction of a redox analyte dissolved in solution, and relating this signal to the analyte concentration [3]. Cyclic Voltammetry is an electroanalytical technique in which the potential is varied linearly with time and the currents arising from the faradaic and non-faradaic process at the working electrode are recorded. The information is expressed using a current vs. potential curve, also known as a Cyclic Voltammogram (CV) [4,5]. Figure 1.1(a) shows the cyclic potential sweep, where the potential is first increased linearly with time to a maximum value, the switching potential E_λ, followed by a reverse sweep to the initial value. The rate of change of potential with time is known as scan rate (ν). Based on the mass-transport mechanism at the working electrode surface, the CVs can have different shapes. Figure 1.1(b) is an example of a CV with an oxidation and reduction peak caused by the formation of a diffusion layer near the electrode [4,5]. In this example, product A is reduced to $A^{\bullet-}$ in the forward sweep and $A^{\bullet-}$ is oxidized to A on the reverse sweep.

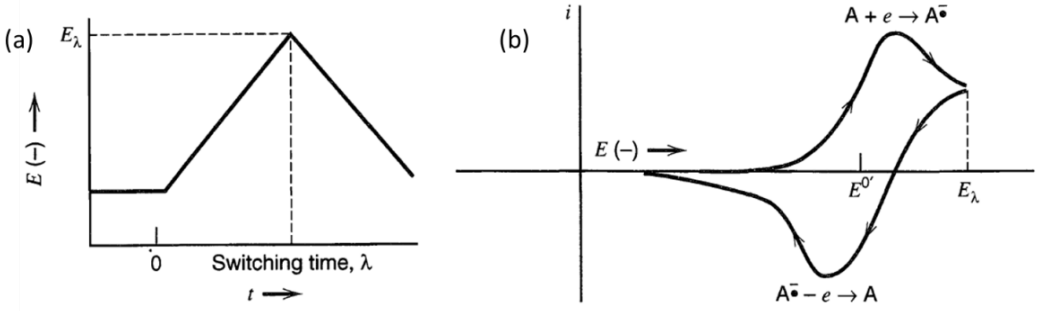

Figure 1. 1(a) Cyclic voltammetry linear potential sweep; (b) Resulting cyclic voltammogram. [4].

Cyclic voltammetry has become a very popular technique for electrochemical studies of many chemical systems because it can provide both qualitative and quantitative information in a relatively short time. It allows direct information such as the formal redox potential ($E^{\prime o}$) of the electroactive species, the stability of the oxidized and reduced forms, the reversibility of the electrochemical reaction, evaluation of the media effect upon the redox reaction, information on thermodynamics of the redox reaction, the electron transfer number (n), kinetic rate constants of the heterogeneous electron-transfer reactions, types of coupled chemical mechanism, and adsorption processes [4,5].

1.3 Ultramicroelectrodes

Ultramicroelectrodes (UMEs) are electrodes with at least one dimension, the characteristic dimension, less than 25μm [6]. Miniaturization of working electrodes not only has obvious practical advantages but also opens several new possibilities. UMEs offer many advantages over macroelectrodes [6-8]:

a) Enhanced rates of mass transport of electroactive species due to radial diffusion to the UME surface allowing rapid attainment of steady state currents and thereby providing excellent temporal resolution.
b) The double-layer capacitance is also lowered which results in a smaller RC time constant in the electrochemical cells. Lower capacitance improves the S/N ratio of the UMEs.
c) The currents observed at UMEs typically lie in the pA to nA range. Due to this, the ohmic drop (*iR*) values are also reduced. Lower *iR* drop minimizes CV distortion allowing their application in less conductive media.

d) The small size of UMEs provides excellent spatial resolution allowing exploration of microscopic domains. This also allows their use for electroanalysis in small volume samples.

Despite having multiple advantages, UMEs do have a major drawback. Due to the small size, the limiting currents are very small which limits the range of measurement. This may require additional instrumentation for signal amplification.

1.4 Objectives of the Research

The purpose of this research is to develop reliable macro- and ultra-micro-electrode array electrochemical biosensor which can be used to identify, quantify, and monitor essential bio-analytes such as Dopamine, Ascorbic Acid and Uric Acid by using CVD nanodiamond films without the need of electrode surface functionalization or modifications, making real-time detection possible.

Boron doped diamond electrodes, although very robust, are not as versatile or effective in detecting different species in a multi-component system such as the one being examined as part of this research. Conventional techniques such as microdialysis and high performance liquid chromatography are relatively slow, require high level of technical knowledge and well-trained staff, and cannot be used for real-time bio-sensing applications.

There has been some work done on nanodiamond macroelectrodes' properties and potential applications. However, this research on nanodiamond based UMEAs is one of the first of its kind. Moreover, to my knowledge, there is no published work on the use of

nitrogen incorporated nanodiamond UMEAs in background subtracted fast-scan cyclic voltammetry (FSCV) for detection of dopamine.

This study is focused on the following:

- Development of a consistent process technique for the deposition nitrogen-incorporated nanodiamond films;
- Identification and optimization of the material properties contributing to the enhanced bio-analyte sensing capabilities of the nanodiamond electrodes;
- Evaluation of multiple fabrication processes for nanodiamond UMEAs;
- Identification of drawbacks and development of well-controlled nanodiamond micropatterned scheme for realizing nanodiamond ultra microelectrode arrays with excellent consistency;
- Electrochemical characterization and analysis of the nanodiamond macro- and ultra-micro-electrode array for detection of DA in the presence of interference such as AA and UA;
- Perform FSCV characterization using nanodiamond UMEA to detect and quantify DA with high sensitivity.

1.5 Organization of the Dissertation

There are five chapters in this dissertation and they are organized as follows:

- ***Chapter I*** provides an introduction to properties of thin-film diamond as an electrode material, the electrochemical technique of cyclic voltammetry and advantages of using ultramicroelectrodes over macroelectrodes. The objectives of the research are stated and the organization of the dissertation is presented.
- ***Chapter II*** consists of a review of physical and electrochemical properties of diamond and ultramicroelectrode arrays (UMEAs) fabricated from different electrode materials such as carbon, metals and boron-doped diamond. Roles of various bio-analytes and their electrochemistry have been discussed. Alternative non-electrochemical detection/monitoring techniques and their drawbacks have also been included.
- ***Chapter III*** describes fabrication and material characterization of nitrogen incorporated nanodiamond film macroelectrodes used in this research, the experimental set-up and results from electrochemical characterization of potassium ferrocyanide, dopamine, ascorbic acid and uric acid. Effect of the input gas mixture, i.e., hydrogen, methane and nitrogen on the physical and electrochemical properties of nanodiamond film macroelectrodes has also been studied.
- ***Chapter IV*** describes the UMEA fabrication processes developed for this research, material characterization and the electrochemistry of pyramidal, planar and columnar nanodiamond UMEAs. Results for electrochemical detection of dopamine by planar UMEA using fast scan cyclic voltammetry (FSCV) have also

been examined. Analysis and discussion of the experimental results are also presented.

- ***Chapter V*** wraps up the dissertation in form of the conclusions and recommendations for future work.

CHAPTER II

LITERATURE REVIEW

2.1 Diamond Structure

Diamond is a carbon allotrope with several properties which make it an interesting material for a wide range of applications. Some of these properties include high thermal conductivity, excellent optical transmission (from IR to UV), highest known strength, hardness and breakdown field, extremely resistant to neutron radiation [9,10].

The electronic configuration of carbon in the ground state is $1s^2 2s^2 2p^2$. However, this configuration does not account for the tetrahedral symmetry seen in diamond. One e^- from the 2s orbital is promoted to the unoccupied $2p_z$ orbital, thereby creating a new hybridized sp^3 structure from 1 s orbital and 3 p orbitals [9,10]. These orbitals are covalently bonded to the orbitals of 4 other carbon atoms to form a regular tetrahedron with equal angles to each other of $109^o28'$ seen in figure 2.1(a). The most common crystalline form of diamond is cubic which can be visualized as two inter-penetrating face centered cubic lattices, one with the origin at 0,0,0 and the other at ¼, ¼, ¼ , with parallel axes [9-12]. Figure 2.1(b) shows the cubic unit cell of diamond with the lattice constant of 0.357 nm [9-11]. The covalent bond length between the carbon atoms is 0.154 nm and high bond energy of 711kJ/mol [9,10]. Each diamond unit cell has 8 atoms: ⅛ x 8 at the corners, ½ x 6 at the face centers and 4 inside the cube [9]. Diamond has the highest atom density of any material (0.293 g-atom/cm^3), making it the hardest material of all substances [9].

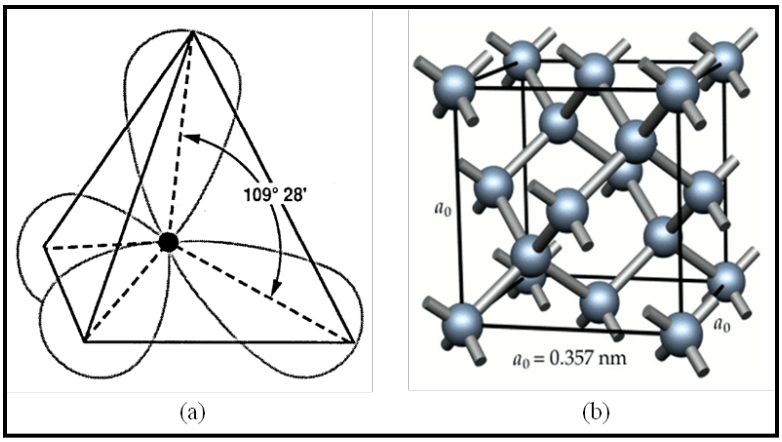

Figure 2. 1(a) The diamond tetrahedron [9]; (b) The diamond unit cell [11].

2.2 Diamond Electrochemistry

Ever since the work of Pleskov in 1987 on photoelectrochemistry using semi-conducting diamond electrodes, research on diamond electrochemistry has grown manifold [13]. Diamond has several attractive properties conducive for electrochemical applications including the high over-potential for oxygen and hydrogen evolution [2, 13-14]. This creates a wide potential window, approximately 3.5V, which is useful to study a larger variety of electrochemical reactions as compared to conventional metallic electrodes like Pt and Au. Figure 2.2 shows a graphical comparison between the background scans in 0.2M H_2SO_4 at 100mV/s using a diamond and a platinum working electrode, which also acts as a catalyst for H_2 evolution [14].

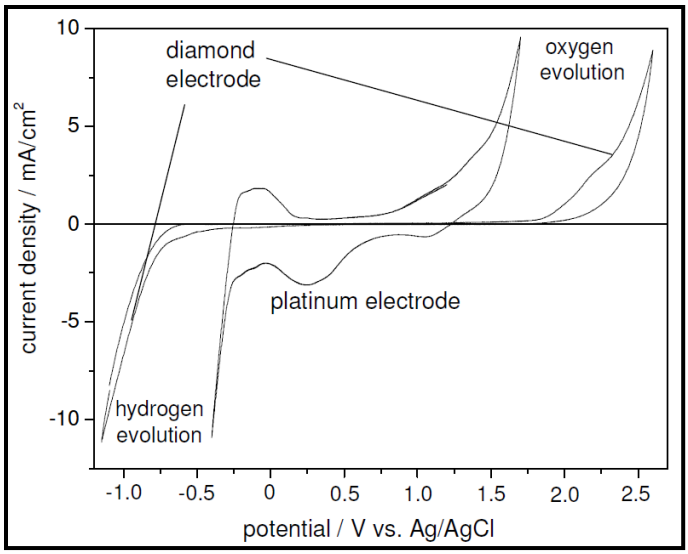

Figure 2. 2 Cyclic voltammograms recorded in 0.2M H_2SO_4 at 100mV/s using diamond and platinum working electrodes. Diamond exhibits a wider potential window, a featureless background and lower capacitive current than platinum [14].

Diamond electrodes exhibit low and stable background currents. Figure 2.3 shows a comparison of the temporal stability of the background current and signal/background current ratio for diamond and glassy carbon electrodes [15]. One possible reason is low density of electronic states near the Fermi level which would mean a reduced accumulation of counter balancing ions and water dipoles at the diamond-electrolyte interface resulting in reduced background currents [14, 16]. Another reason suggested for lower capacitance is the hydrogen termination of the diamond surface. However, mild electrochemical anodic oxidative treatment which leads to oxygen terminated surface did not show a notable increase in the double layer capacitance indicating the limited impact of oxygen containing surface groups [14,17]. Hydrogen-terminated diamond films exhibit reversible to quasi-reversible electron transfer kinetics for inorganic redox analytes such as $Fe(CN)_6^{-3/-4}$, $Ru(NH_3)_6^{+2/+3}$, and $IrCl_6^{-2/-3}$[14,17,18].

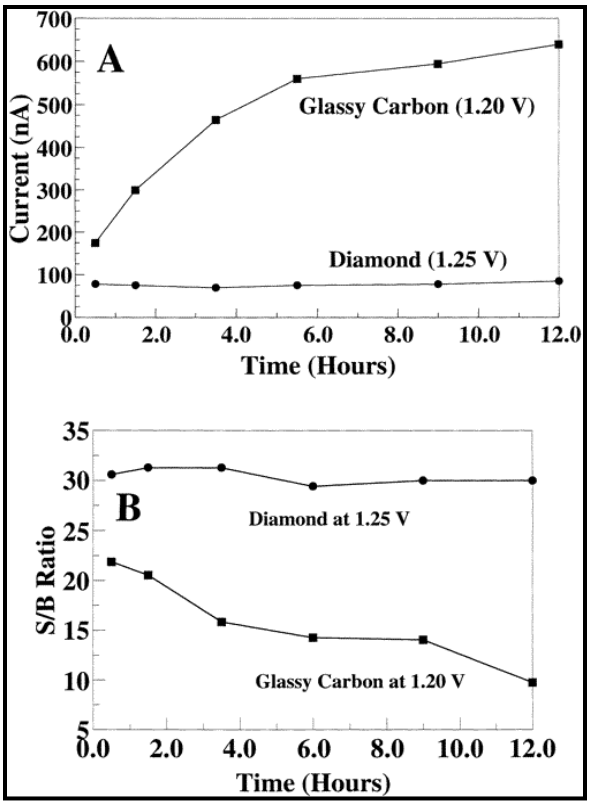

Figure 2. 3 (a) Background current versus time profiles for (●) diamond at 1.25 V and (■) glassy carbon at 1.20 V in 0.1 M phosphate buffer, pH 7.2. Flow rate 1.0 ml/min. (b) S/B ratios versus time for (●) diamond and (■) glassy carbon during exposure to 0.1mM N_3^- in 0.1M phosphate buffer, pH 7.2. Figure is reproduced from [15].

Besides inorganic redox analytes, numerous biological molecules, e.g., glucose, histamine, serotonin, dopamine, ascorbate, amino acids, cytochrome, etc. have also been detected using doped diamond electrodes because of its biocompatibility and resistance to fouling[18,19,20,21]. Examples of other electrochemical applications of diamond electrodes include destruction of organic and inorganic contaminants in polluted water [22-25]. Thin-film diamond coated niobium and mixed metal-oxide coated titanium anodes are used for high current application in zinc, nickel and chromium electro-deposition baths and production of hexavalent chromium Cr(VI), respectively [26-27]. Because of their high oxygen overvoltage in aqueous electrolytes, doped-diamond

electrodes can be used for electro-synthesis of strong oxidizing agents such as ozone and permanganate [28-30]. Diamond thin-films have also been used in electrochemical energy storage systems such as electrochemical double layer capacitors and lithium ion batteries [31-32].

2.3 Ultramicroelectrode Arrays

Microelectrodes have several benefits over macroelectrodes by virtue of their size. Their advantages include lower capacitance and iR_u losses, enhanced temporal and spatial resolution, usability in highly resistive media, increased signal to noise ratio [33-34]. Carbon fibers, carbon nanotubes, noble metals like gold and platinum are widely used as microelectrodes in multiple configurations.

Based on the array design, MEAs can be classified as random MEAs or ordered MEAs [33]. Random MEAs are characterized by a statistical distribution of electrodes that maybe of identical or dissimilar dimension and shape. The main advantage of such arrays is the ease of fabrication. However, these arrays are geometrically ill-defined which can lead to overlapping of individual diffusion layers and thereby complicate data interpretation. On the other hand, ordered arrays consist of individual microelectrodes with well controlled sizes and regular spacing. Ordered arrays can be fabricated using conventional silicon microfabrication technology.

The response of ordered MEAs working at the same potential depends on the dimensions of the individual microelectrodes and the thickness of the diffusion layer with respect to the microelectrode [33-34]. Diffusion layer is the region where a concentration gradient exists between the electrode surface and the bulk solution [33-34]. At very short

time scale, as in fast scan cyclic voltammetry (FSCV), the diffusion layer thickness is relatively smaller than the radii of the microelectrodes and semi-infinite linear diffusion (planar diffusion) is dominant, as seen in figure 2.4(a). Under these conditions the cyclic voltammogram is peak shaped and the current is given by the Cottrell equation (equation 2. 1):

$$\boldsymbol{i(t) = \frac{nFAC^{*}\sqrt{D_O}}{\sqrt{\pi t}}} \qquad \boldsymbol{(2.1)}$$

where: n= number of e^- transferred per mole of analyte, F= Faraday's constant (96500 C/mol), A= active area of the array (cm^2), D_O= diffusion constant (cm^2/s), C*= bulk concentration of the solution (mol/cm^3) and t= time (s). At intermediate time scale, the diffusion layer thickness grows larger than the microelectrode dimension (r) at which point, hemispherical diffusion is present and steady state conditions are observed, as seen in figure 2.4(b). However, the diffusion layer thickness is still $\leq$ d (microelectrode spacing). The steady state limiting current for an array of microdisks of radius r is given by equation 2.2:

$$\boldsymbol{i_{steady\ state} = 4nFD_O\ C^{*}r} \qquad \boldsymbol{(2.2)}$$

At larger time scales, the individual diffusion layers overlap creating pseudo planar diffusion conditions. Under these conditions, the array behaves like a planar electrode where the current is proportional to the entire array area, including the insulating regions in between the microelectrodes and with peak shaped cyclic voltammograms, evident in figure 2.4(c).

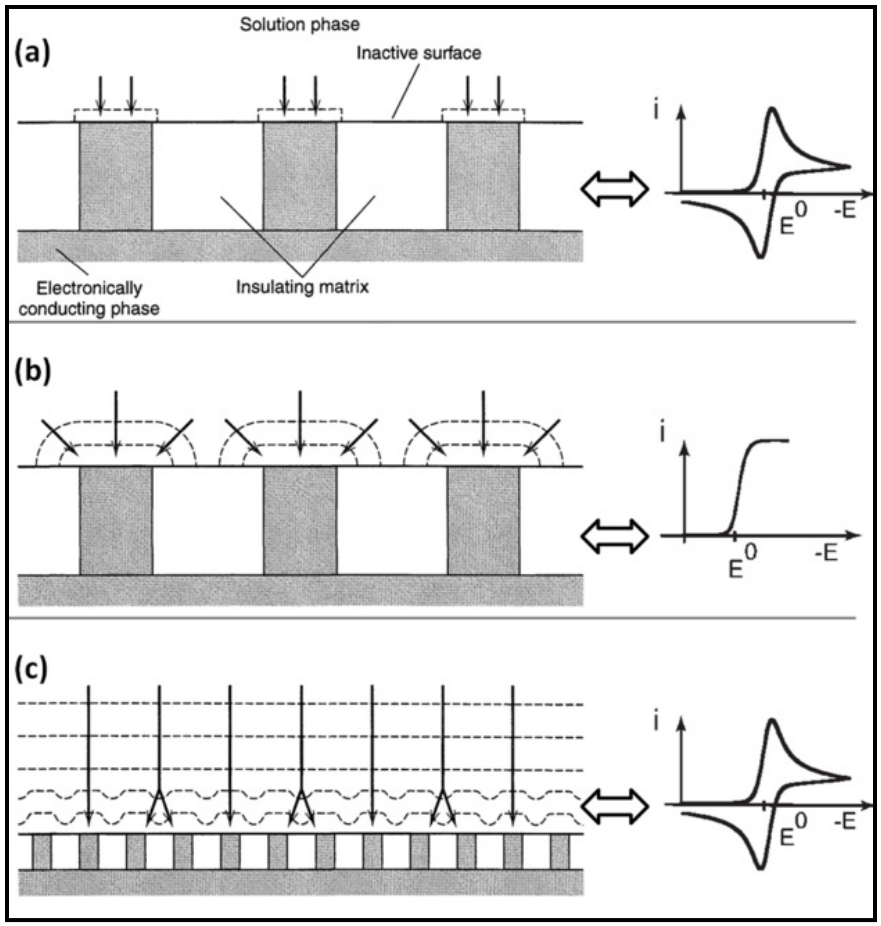

Figure 2. 4 Evolution of the diffusion profile at the surface of an ordered microelectrode array and the corresponding cyclic voltammograms. (a) Short time scale- planar diffusion; (b) Intermediate time scale- hemispherical diffusion and (c) Large time scale- planar diffusion [34].

2.3.1 Carbon Ultramicroelectrode Arrays

Carbon microelectrodes/microprobes, especially carbon fibers, have been popular because they are biologically compatible and not toxic to cells, their electrochemical behavior is well understood and they are available with diameters less than 10µm making them suitable for implantation with minimal tissue damage [35-37]. Despite having limitations like higher background currents and deactivation due to fouling, carbon fibers can be used with or without surface modification and/or functionalization to detect a wide

variety of bio-analytes [38]. Researchers have been able to achieve enhanced sensitivity and selectivity by application of techniques such as overoxidation, flame etching, electrochemical etching, coating with substances like Nafion, 4-sulfobenzene, MWCNTs suspended in dimethylformamide, Nafion with o-phenylenediamine [35,39-43]. Signal from an individual microelectrode/microprobe can be amplified by using an array of such microelectrodes.

Zhang et. al. developed a microdisk array of individually addressable carbon fiber electrodes and achieved enhanced spatial and temporal resolution for detection of neurotransmitter release [44]. The arrays were fabricated by pulling the tip of a multi-barrel glass capillary containing a carbon fiber (2.5μm diameter) in each capillary, followed by polishing to form a planar carbon microdisk surface. The resulting sensors were utilized to examine subcellular heterogeneity in exocytosis from single cells, with resolution as low as 5μm [44].

Several other techniques for fabricating carbon microdisk electrode arrays have also been reported. Some include placing of carbon fibers in epoxy resin, filling up pores of microporous host membrane (3, 8 and 13μm) with carbon paste, fabricating random graphite MEA by mixing graphite powder with epoxy resin and mounting on glass tubing [45-49].

Jin et. al. started by drawing a small amount of mercury into a glass capillary(300μm) and then inserted about 45 carbon fibers (8μm) at the other end. A low-viscosity adhesive was used at one end of the capillary to seal the carbon fibers to it while a copper wire was inserted from the other end to create a contact with the carbon fibers

via the mercury junction. This microelectrode array was used for determination of bovine serum albumin as well simultaneous determination of adenine and guanine [50-51].

Other carbon forms have also been successfully used to fabricate microelectrodes and MEAs. Zachek et. al. fabricated MEA (50µm x 10µm) composed of pyrolyzed carbon via photolithography and exposure to high temperatures (1000^{o}C) enabling decoupled detection of dopamine and oxygen [52]. Yan et. al. fabricated a sensor capable of detecting 3,4- dihydroxyphenylacetic acid (DOPAC) by functionalizing single-walled CNTs adsorbed on a glassy carbon electrode with cyclophane [53]. Xu et. al. developed a glucose sensor from carbon post- microarrays by a two-step route including formation of posts of photoresist (SU-8) under UV exposure and pyrolysis of SU-8 [54]. Fiaccabrino et. al. used RF sputtering to deposit a carbon film on a Si/Si_3N_4 substrate and photolithographically outlined an interdigitated electrode array (IDA) followed by a reactive ion etch [55]. The IDA was employed for detection of dopamine and acetaminophen.

2.3.2 Metal Ultramicroelectrode Arrays

Gold is one of the most frequently used materials for microarray fabrication. Wu et. al. fabricated a gold circular microarray by wrapping a piece of gold mini-grid (approximately 3x5 mm, thickness ranging from 3µm-6µm and width of about 12µm) around pre-cast cylinders approximately 3, 4, 5 and 6mm in diameter [56]. Bond et. al. made an individually addressable 10x10 gold microarray electrode by embedding gold wires in epoxy resin layer-by-layer [56].

Work done by Walt et. al. involved deposition of a 1-µm layer of gold nanoparticles around the surface of 25-µm-diameter optical glass fibers individually [58]. A self-assembled monolayer (SAM) was then formed by immersing the gold-coated fibers into ethanolic solutions containing 11-mercapto-1-undecanol to prevent electrical contact with neighboring ring electrodes. A ring-shaped gold microelectrode array was finally achieved by randomly embedding the above SAM/gold/fibers into an insulating epoxy.

Sheu and co-workers used conventional silicon microfabrication technology to fabricate an individually addressable 5x5 array of gold microdisk electrodes (30µm diameter) [59-60]. The gold MEA was coated with collagen followed by plating with PC12 cells and then used for in-situ temporal detection of dopamine exocytosis.

Pai and co-workers fabricated high surface-area 3D gold microelectrodes suitable for incorporation into lab-on-a-chip devices [61]. The structure of the gold microelectrodes was formed by applying a patterned silicon mold, heat, and pressure to the gold electrodes, resulting in square pillars with 20µm sides and a depth of 18µm. The electrodes exhibited improved limits of detection for catechol and good stability over 8 months of use.

At gold electrodes, thiol adsorption is a common problem. In brain tissue, glutathione is present at relatively high concentrations and will rapidly passivate the electrode [62]. This drawback can be overcome by using protective polymer films such as Nafion at the cost of a slower response [62].

In addition to gold, platinum and iridium are also used as working electrode materials or as a substrate for other active electrode materials. Pt, Ir and Au UMEAs have

been fabricated using standard photolithographic techniques, with Si/SiO_2/metal structures [63]. This technique provides excellent control over the final electrode structure and can be adapted to suit specific applications. Variation in the process can be introduced by using different passivation layers such as SiO_2 or Si_3N_4 or polyimide, by using reactive ion-etch (RIE) in lieu of wet etch to define the final UMEA structure [63-64]. Metal UMEAs have the common drawback of a narrow working potential window which may limit their application to reductive electrochemical reactions [63].

2.3.3 Diamond Ultramicroelectrode Arrays

Diamond UMEA combines the excellent material properties of diamond such as relatively low background currents, wide working potential window, dimensional stability, biocompatibility and resistance to fouling via adsorption with the advantages of the small geometry which include enhanced analyte flux, low capacitance and iR_u loss, excellent spatial resolution [1-2, 6-8].

Boron doped diamond (BDD) has been widely studied for electrochemical applications and several UMEAs have been fabricated for various applications. Fujishima et. al fabricated a BDD array by using a structured Si substrate on which BDD was deposited [65]. After this, the surface was spin coated with a polyimide film, which is then mechanically polished until the diamond tips are just exposed. The BDD array consisted of 200 microdisks with diameters between 25 and 30μm, each separated by a distance of 250μm. Steady state currents were observed for detection of important bio-analytes, ascorbic acid (AA) as well as DOPAC.

Rychen's BDD array was fabricated by first growing a BDD film onto which a Si_3N_4 insulating layer (0.5µm thick) was deposited [66]. Standard photolithographic techniques were used to define the array structure followed by RIE of Si_3N_4, thus effectively creating a recessed BDD array. The final structure consisted of a hexagonal array of 106 BDD disks which are 5µm in diameter, separated by 150µm with a coplanar BDD counter electrode. However, the Si_3N_4 layer may not be stable under harsh conditions such as sonoelectrochemistry (use of ultrasound in electrochemical experiments) or elevated temperatures and pressures [67]. Measurements of sulfate and peroxodisulfate were performed with the BDD array [66].

Madore et al. have reported on a BDD-MEA fabricated by using CVD diamond deposition and photolithographic techniques producing microdisk electrodes, which were 5µm in diameter and separated by 100µm [68]. This device was used for trace-metal analysis.

An all diamond microelectrode array was fabricated by Compton et. al. where a hexagonal unit cell pattern is micro-machined by using a combination of PECVD diamond growth process and laser ablation shaping technique [69]. After growing 500µm thick layer of BDD, UV laser ablation was employed to create a hexagonal array of tapered diamond columns with diameters 10-25µm, heights of 15-50µm and a spacing of 10x the diameter. A layer of intrinsic diamond was grown over the array and then partially removed by a lapidary technique to expose the conducting BDD array in a non-conducting diamond matrix. The BDD microelectrode array was modified with silver and used for detection and measurement of hydrogen peroxide (H_2O_2) which is also an important bio-analyte [70].

Soh and co-workers fabricated BDD UMEAs with a SiO_2 insulating matrix for electroanalytical applications [71-72]. Conventional photolithography was used to define the array design on an oxidized (2μm SiO_2), highly doped n-type silicon substrate. The oxide was wet-etched in the exposed areas to form a mold which was then selectively filled with BDD grown by PECVD process. The devices thus fabricated consisted of a 24x84 array with 20μm edge length and 20μm spacing; and a 10x23 array, with 20μm edge length and 100μm spacing [71]. Another variation to this process involved growing 0.5μm thick thermal oxide, followed by sputtering 0.5μm thick layer of molybdenum which acts a sacrificial layer to protect the underlying SiO_2 insulating layer during PECVD diamond growth process. The resulting devices had rectangular UMEs (dimensions: 80μmx2μm) and spacing of 20μm and 100μm [72]. A steady state response consistent with hemi-spherical diffusion limited mass transport was observed for detection of $Fe(CN)_6^{4-}$ and DA [72].

Carabelli and co-workers used a nanocrystalline BDD MEA device for studying high-time resolution of quantal catecholamine secretion from chromaffin cells [73]. The fabrication process involved growing a layer (200nm) of intrinsic nanodiamond film on a single crystal sapphire wafer, followed by another layer (350nm) of quasi-metallic boron doped nanodiamond film. The device layout was defined by a 3 mask microfabrication process and an O_2/Ar plasma etch to remove the exposed nanodiamond. The electrochemically active areas were exposed by patterning a SU-8 (an epoxy based negative photoresist) passivation layer, thus creating an individually addressable 4x4 array with 20μm diameter recessed micro-disks separated by 40μm.

2.4 Electrochemical Detection of Bio-analytes

Electrochemistry provides scientists with valuable tools to identify and quantify different bio-analytes in the human body, specifically, the central nervous system [62,74]. This is possible due to the fact that these target molecules are electrochemically active, i.e., they can be oxidized and reduced which is accompanied by charge transfer. Electrochemical techniques have been used to detect targets such as simple inorganic ions, catecholamine and indolamine neurotransmitters and their metabolites, glutamate, nitric oxide (NO), glucose, lactate, ascorbate, urate, hydrogen peroxide (H_2O_2), oxygen (O_2), and pH [20-21,35,39,40,42-44,52-53,60,63,72-74]. Reactions associated with some of these species can be seen in figure 2.5 [74].

Traditional electroanalytical techniques cannot be used for detection of non-electroactive species. However, those that can be oxidized by an enzymatic reaction can be measured electrochemically by coupling the enzyme reaction with electrochemical detection [62,74]. These species include amino acid neurotransmitters such GABA (γ-aminobutyric acid) and its precursor, glutamate as well as acetylcholine and its precursor choline [62,74]. Glucose and lactate, compounds which are important in energy production in the brain, have also been detected with this indirect electrochemical approach [62,74]. For example, the reactions involved in detection of glutamate include the reduction of glutamate oxidase (enzyme) which in turn gets oxidized to produce hydrogen peroxide (H_2O_2). The enzyme is immobilized in thin films on the electrode surface. Hydrogen peroxide then diffuses to the electrode surface and is oxidized. This reaction can be detected electrochemically and the rate of H_2O_2 production is directly related to the concentration of glutamate [74].

$$Glutamate + GluOx\ (Ox) \rightarrow\ \alpha - ketoglutarate + NH_3 +\ GluOx(Red)$$

$$GluOx(Red) +\ O_2 \rightarrow GluOx(Ox) +\ H_2O_2$$

$$At\ the\ electrode\ surface: H_2O_2\ \rightarrow 2H^+ +\ O_2 +\ 2e^-$$

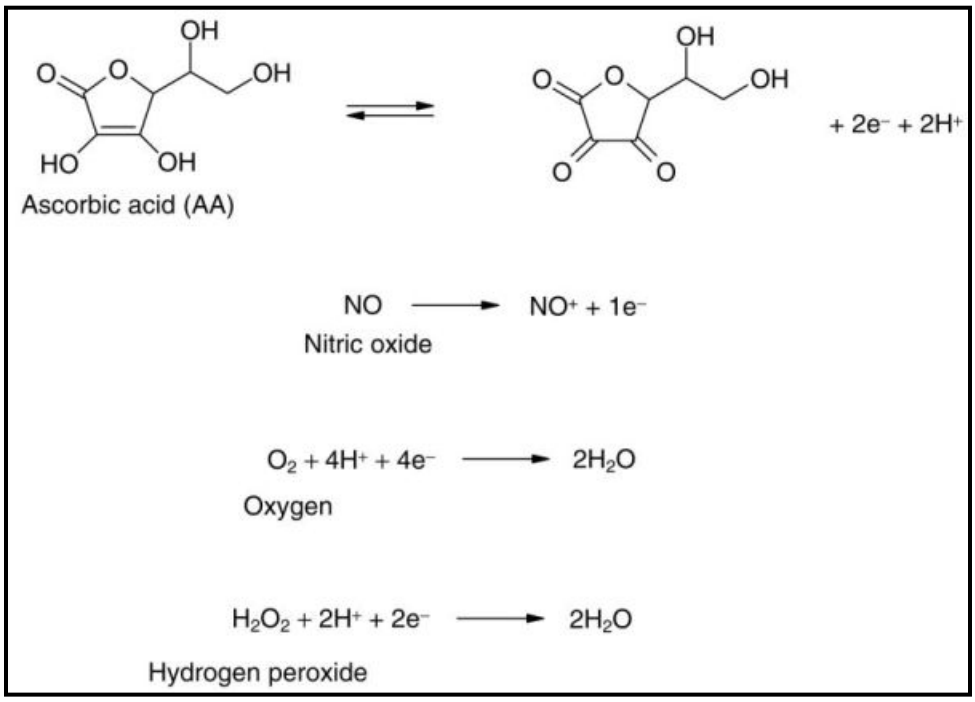

Figure 2. 5 Electrochemical reactions involving some of the electroactive species found in the mammalian brain- ascorbic acid, nitric oxide, oxygen and hydrogen peroxide [74].

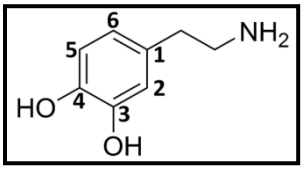

Figure 2. 6 Molecular structure of dopamine showing the –OH groups in positions 3 and 4 of the benzene ring with the -NH_2 containing side chain at position 1.

2.4.1 Neurotransmitters and interferant molecules

Neurotransmitters are chemicals that are secreted by neurons and relay messages to target cells. The family of catecholamine neurotransmitters consists of electrochemically active compounds such as dopamine (DA), epinephrine (adrenalin) (EPI) and norepinephrine (noradrenalin) (NE) [62,74-77]. Catechol is the name given to an aromatic ring with two hydroxyl groups (-OH) attached to adjacent groups, 3 and 4 positions of the rings in case of catecholamines. The number 4 carbon is opposite the side chain containing the amine group ($-NH_2$) as seen in figure 2.6 via the structure of dopamine [79]. Many of their metabolites are also electroactive.

Dopamine, the precursor of norepinephrine, has biological activity in the periphery, most particularly in the kidney, and serves as a neurotransmitter in several important pathways in the central nervous system (CNS) [75-77]. Norepinephrine is a neurotransmitter in the brain as well as in postganglionic, sympathetic neurons [75,77]. Epinephrine, formed by the N-methylation of norepinephrine, is a hormone released from the adrenal gland, and it stimulates catecholamine receptors in a variety of organs [75,77]. Small amounts of epinephrine are also found in the CNS, particularly in the brainstem [75,77].

DA is a central player in the brain "reward" system. Proposed roles for DA in the reward system include the mediation of hedonia (pleasure), a messenger of incentive salience (wanting) and as an error signal that promotes the learning associated with goal directed behavior (62). This system is activated by natural rewards such as food, drink and sex, as well as by addictive drugs like cocaine and amphetamines etc. [76,78]. DA is also involved in motor and cognitive functions. Low DA levels have been associated with

Parkinson's disease which is characterized by uncontrollable and shaky body movements. While with schizophrenia, where a patient is unable to relate to reality the way the majority of the people do, an excess of DA is released in the body [75-76, 78].

One of the key functions of norepinephrine is to regulate blood pressure by stimulating blood vessels to constrict when the blood pressure drops below a certain level [79]. High levels of NE release have been associated with aggression in animals, healthy adults and patients with depression and mania while decrease in NE levels have been observed in patients with generalized anxiety disorder and post-traumatic stress disorder [79]. Epinephrine, levels in the body are much lower than that of NE and its function in the central nervous system is not fully understood [79]. However, as a hormone, epinephrine increases heart rate, contracts blood vessels and dilates air passages [80,81]. It also stimulates glycogenolysis, conversion of glycogen to glucose, in the liver and muscle and triggers lipolysis, breakdown of lipids, to increase energy production by the cells in the body [80, 81].

Catecholamines are derived in a biosynthetic pathway from tyrosine (62,75,77). The hydroxylation of tyrosine with the enzyme tyrosine hydroxylase produces L-DOPA (3,4-dihydroxyphenylalanine). The L-DOPA formed is converted to DA (dopamine) by the enzyme dopadecarboxylase. Norepinephrine is formed after the transfer of a hydroxyl group onto the β-position of the side chain via dopamine- β-hydroxylase. The amine of norepinephrine can be methylated by phenylethanolamine-N-methyltransferase. In this pathway, the rate limiting step is the conversion of tyrosine to L-DOPA. A schematic of the synthesis of catecholamines can be seen in figure 2.7 [75].

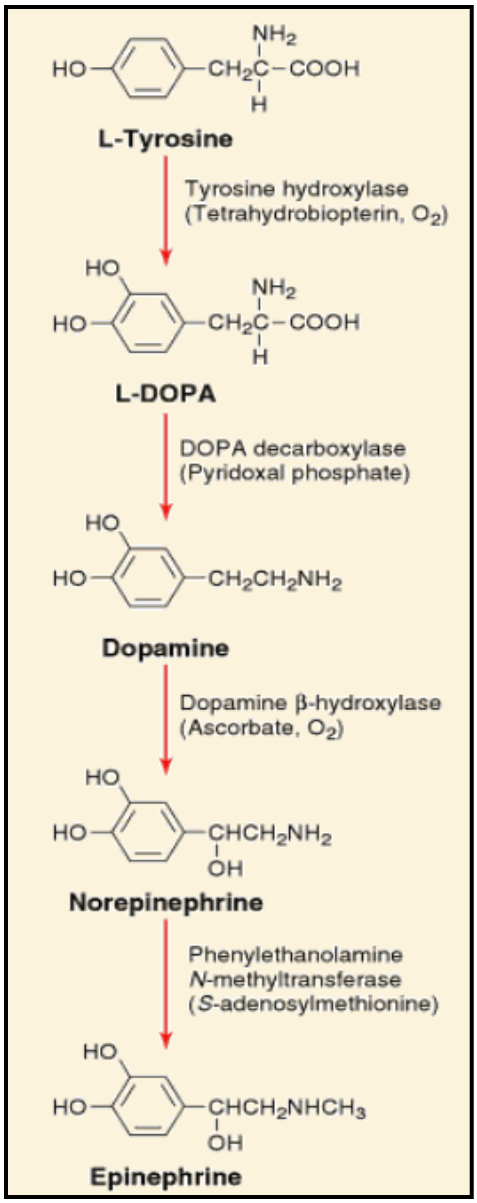

Figure 2. 7 Biosynthetic pathway derived from l-tyrosine for catecholamines [75].

Catecholamines are metabolized by multiple enzymes including monoamine oxidase (MAO) and catechol-O-methyltransferase (COMT) [62,75,77]. In case of DA, the intermediate formed after deamination by MAO is metabolized by aldehyde dehydrogenase to form 3,4- dihydroxyphenylacetic acid (DOPAC) [62,75,77]. COMT can also metabolize DA to produce methoxytyramine which can be further metabolized

by MAO and aldehyde dehydrogenase to produce homovanillic acid (HVA) [62,75,77]. DOPAC can be metabolized to for HVA as well, which is the principal end-product of DA [62,75,77]. Figure 2.8 shows the primary metabolic pathways of Dopamine metabolism along with the responsible enzymes and the corresponding metabolites [77].

NE and EPI are metabolized by the combination of MAO and aldehyde reductase to produce 3,4-dihydroxyphenylglycol (DHPG) [62,75,77]. Another pathway involves COMT which results in production of normetanephrine from NE and metanephrine from EPI [62,75,77]. Normetanephrine and metanephrine are metabolized to produce 3-methoxy-4-hydroxyphenylglycol (MHPG) by the action of MAO and aldehyde reductase. COMT metabolizes DHPG to produce MHPG as well [62,75,77]. The principal end product of NE and EPI metabolism is vanillylmandelic acid (VMA) which is produced by the oxidation of MHPG catalyzed by alcohol dehydrogenase [62,75,77].

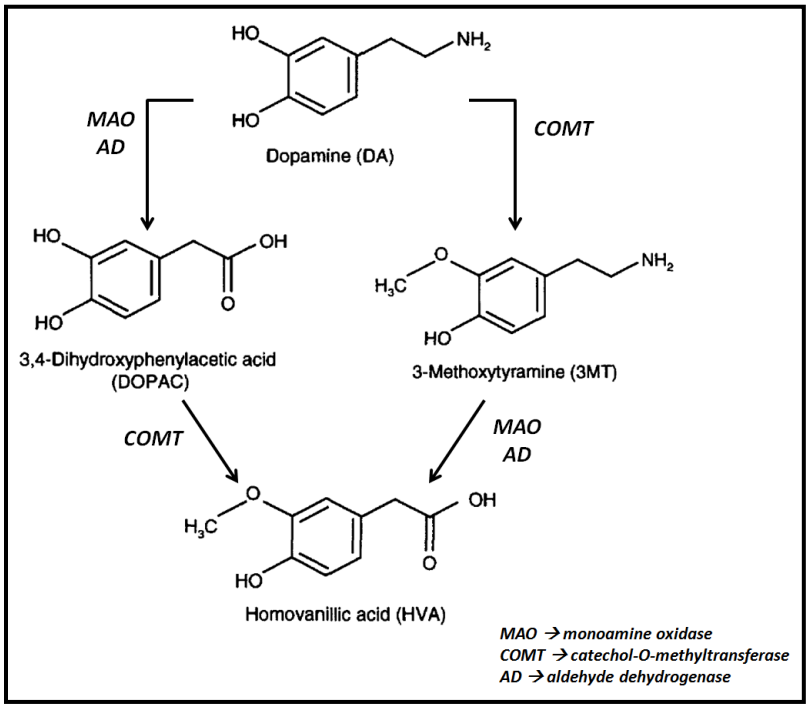

Figure 2. 8 Pathways of Dopamine metabolism leading to the production of HVA [77].

Measurement of catecholamine metabolites can provide insight into the rate of release or turnover of catecholamines in the brain [75]. Abnormally high levels of plasma and urinary HVA and VMA can be indicative of the presence of a neuroblastoma, a malignant tumor of immature nerve cells, and a low VMA:HVA ratio (< 1) suggests a poor prognosis [82]. Concentrations of HVA are decreased in the cerebrospinal fluid (CSF) of patients with Parkinson's disease [75]. Measurement of free metanephrines, metabolites of NE and EPI, in the plasma has shown to be a very sensitive test for the detection of pheochromocytoma, a rare neuroendocrine tumor [83]. MHPG levels measured in the cerebrospinal fluid and urine provide an index of NE turnover in the brain and lower concentrations of MHPG have been observed in certain forms of depression, while in case of generalized anxiety disorder, MHPG levels increased [75].

Ascorbic acid (AA) or vitamin C exists in its deprotonated form, ascorbate, at physiologic pH. AA levels in the extracellular fluid of the brain are much higher than other bio-analytes of interest such as DA [84]. In addition, AA is electrochemically active and acts as an interferant in DA detection [84-86]. AA has been linked to extracellular modulation of neurotransmitters such as glutamate and dopamine [84]. As an electron donor, AA acts as a power anti-oxidant in the body to protect against the effects of free radicals generated by normal biological activity [84]. AA can also stop the oxidation of cellular membranes by recycling or preventing oxidation of vitamin E [84]. Deficiency of AA causes scurvy, a disease associated with weak and swollen limbs, bleeding gums, hemorrhages under the skin and a failure of the wounds to heal. Citrus fruits and red and green vegetables are rich sources of AA [84].

Uric acid (UA) is the primary product of purine metabolism [85-88]. Continuous monitoring of UA in the body fluid is essential since its abnormal concentration levels lead to several diseases, such as hyperuricaemia, Lesch-Nyan syndrome and chronic renal disease [85-88]. UA can also serve as a marker of cardiovascular as well as a number of diabetic complications [88]. Like AA, UA is also present in high concentrations in the serum, urine and the extra cellular fluid and interferes with the electrochemical detection of DA [85-88].

2.4.2 Electrochemistry of dopamine, ascorbic acid and uric acid

DA is a monoamine which can be easily oxidized and reduced making it a suitable target for electrochemical detection. All catecholamines form the corresponding o-quinone after oxidation, along with a transfer of 2 electrons and 2 protons. The redox reaction for DA is shown in figure 2.9. Dopamine-o-quinone (DAQ) contains both an electron deficient ring and an electron-donating amine [89]. When the amine is deprotonated, the molecule undergoes a 1,4 (Michael) addition resulting in a cyclization reaction which produces leucodopaminechrome (LDC), as seen in reaction 1 in figure 2.10 [89]. LDC can also undergo a 2 electron oxidation reaction to produce dopaminechrome (DAC), as seen in reaction 2 in figure 2.10 [89]. This set of reactions can be categorized as an electrochemical-chemical-electrochemical (ECE) reaction and is observed at relatively large time scales [89]. Fast scan rates can suppress the slower, cyclization reaction.

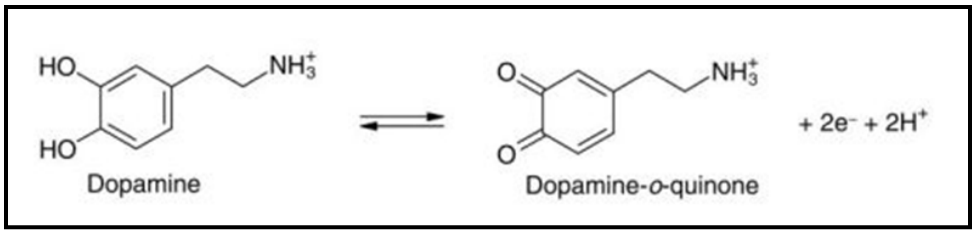

Figure 2. 9 Dopamine undergoes a reversible oxidation reaction accompanied by a transfer of 2 electrons and 2 protons.

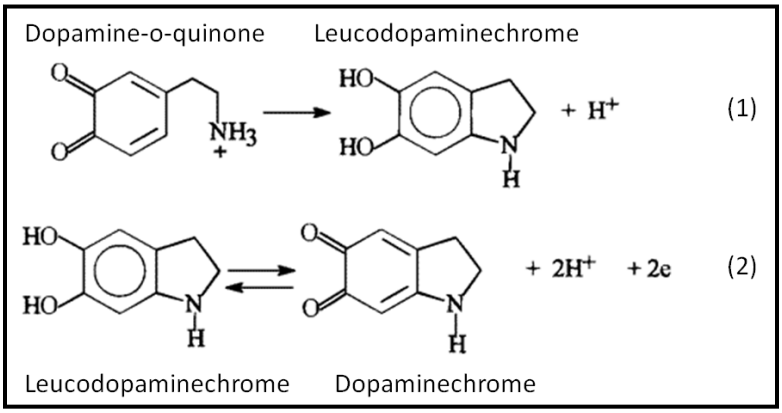

Figure 2. 10 (1) DA is oxidized to form DAQ which undergoes a cyclization reaction after deprotonation. (2) The cyclization reaction produces an electrochemically active molecule LDC which can be readily oxidized to DAQ along with a transfer of 2 electrons and 2 protons.

Ascorbic acid exists in high concentrations, 200μM- 500μM, in the extra cellular fluid which is about 100-1000 times the dopamine concentration [84,90-92]. Ascorbic acid has two dissociable protons with pK_a (dissociation constants) values of 4.2 and 11.8 [84]. Thereby, it exists as a monovalent anion, ascorbate, at the physiologic pH of 7.4. Ascorbate can be oxidized to form ascorbyl radical along with the loss of one electron [84]. A second electron and proton loss produces dehydroascorbate [84]. The net reaction consists of oxidation of AA to dehydroascorbate and transfer of two electrons and protons, as seen in figure 2.11.

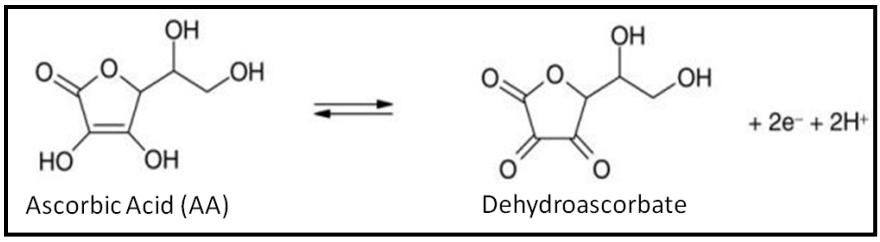

Figure 2. 11 Ascorbic acid can be oxidized to produce dehydroascorbate which is accompanied by a two electron and two proton transfer.

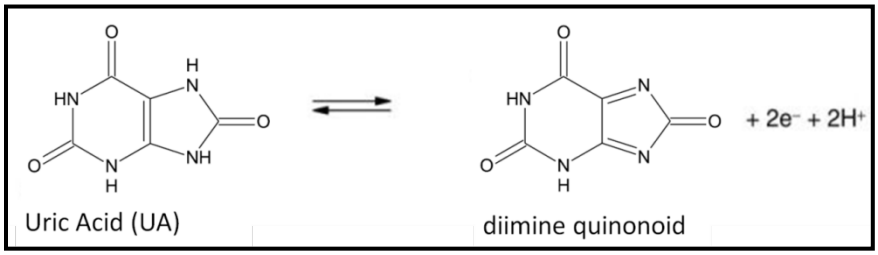

Figure 2. 12 Uric acid can be oxidized to produce a diimine quinonoid which is accompanied by a two electron and two proton transfer.

Electrochemical activity of uric acid is also easily detectable due to its high concentrations, 240µM-520µM in serum and 1.2mM-4.4mM in urine [93]. It is a weak acid with two dissociation constants, pK_a, of 5.5 and 10.3 [94-95]. Consequently, under physiologic conditions uric acid exists in its anionic form called urate which is more soluble. Excess of uric acid leads to formation of kidney stones and one of the approaches to treat this is to alkalinize the urine which converts the uric acid to the more soluble urate [95]. Uric acid can be oxidized to form a diimine quinonoid along with a transfer of 2 electrons and 2 protons, as shown in figure 2.12.

2.5 Alternative bio-analyte detection techniques and their drawbacks

Microdialysis is a sampling technique wherein a perfusion fluid is passed through a microdialysis probe with a membrane implanted in the brain [62,74]. Small molecules are able to diffuse through the membrane and the fluid or the dialysate is collected for further analysis [62,74]. The bio-analytes in the dialysate can be identified by using high performance liquid chromatography or capillary electrophoresis coupled with electrochemical methods or fluorescence spectroscopy or mass spectroscopy [62,74].

The most significant advantage of microdialysis is that it offers excellent chemical selectivity, the results in form of chromatogram or electropherogram peaks are very accurate [62,74]. However, it suffers from several disadvantages where electrochemical techniques win.

1. The microdialysis probe size is > 200μm in diameter as compared to microelectrode probes with diameter of a few microns. Due to the small dimensions, microelectrodes cause minimal tissue damage during implantation and they can be placed very close to the neuronal terminals which are on the same dimensional scale [62,97]. This provides excellent spatial resolution which can reduce diffusional distortion while recording dynamic events as well as allow monitoring events at a cellular level [74,98].
2. The microelectrodes provide excellent temporal resolution allowing users to study high speed and highly localized events near the neurons, either due to external stimulation or spontaneous electrical activity of dopaminergic cells [74].
3. Also, results from microdialysis have a lengthy turnaround time and require specialized laboratories as well [99].

There are other spectroscopic techniques which are non-invasive and provide information on brain activity with good spatial resolution. Among those include functional magnetic imaging (fMRI) and positron emission tomography (PET) [62]. These techniques only provide qualitative and spatial information about the neuronal activity and can be used to study in real time pharmacological effects and response to external stimuli [62]. Also, they require very expensive equipment and specialized staff, limiting their use for widespread research [99].

CHAPTER III

NANODIAMOND MACROELECTRODES

This chapter describes the work done to develop nitrogen incorporated nanodiamond macroelectrode. Microwave plasma enhanced chemical vapor deposition (MPECVD) process was used to grow these nanodiamond films on highly doped n-type silicon substrates. Nitrogen gas was added to the input gas mixtures to achieve nitrogen incorporation. The films were characterized by using SEM (scanning electron microscope), Raman spectroscopy and XPS (X-ray photoelectron spectroscopy) to study the microstructure and composition. Electrochemical experiments were performed to determine the electroanalytical capabilities of the macroelectrode. The ferri/ferrocyanide redox couple and bio-analytes such as dopamine (DA), ascorbic acid (AA) and uric acid (UA) were studied in-vitro. Also, the selectivity of the macroelectrode to detect DA in the presence of UA and AA was explored since that reflects true physiological conditions.

In addition to this, nanodiamond films were also grown by varying the input gas mixtures in the MPECVD process. Below a threshold value of hydrogen flow rate, continuous nanodiamond films were not obtained and these samples could not be used as electrodes. Increments in nitrogen flow rates in the gas mixture had a distinct effect on the microstructure; electroanalytical properties of the corresponding nanodiamond films were also characterized.

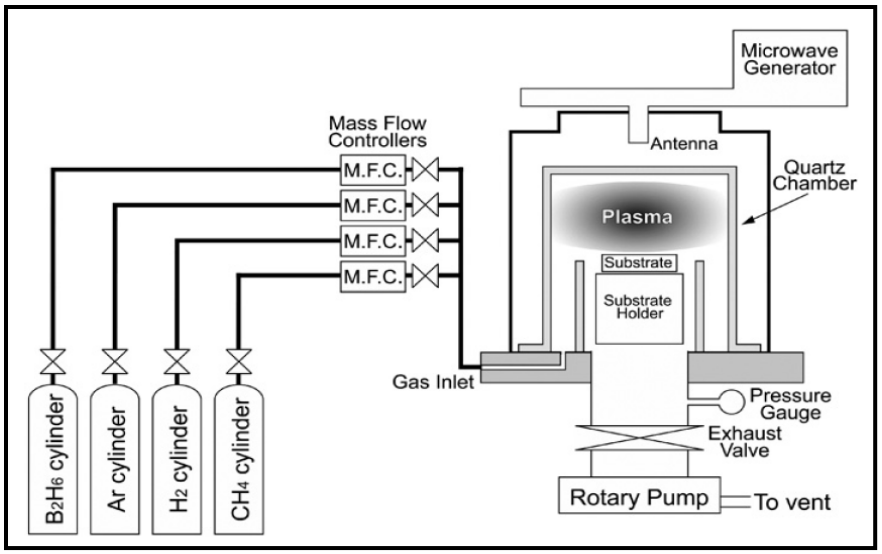

Figure 3. 1Block diagram of a MPECVD system [1].

3.1 Nitrogen incorporated nanodiamond macroelectrodes

3.1.1 Fabrication of nitrogen incorporated nanodiamond macroelectrode

The nanodiamond films in this work were grown using MPECVD process. Some of the advantages of using MPECVD are reasonable linear growth rates, excellent quality of the diamond, good control over the deposition parameters, stable system operation and film adherence to a wide variety of substrates [100-101,103]. However, there are certain limitations on the size of the substrates and diamond growth rates [100-101,103].

Figure 3.1 shows a block diagram of a typical MPECVD setup. It consists of gas sources, mass flow controllers, vacuum pump, pressure regulators (valves), substrate heater, temperature sensors, microwave generator and a water cooled reaction chamber. The microwave energy from the generator is directed to and focused in the reaction chamber producing spherically shaped glow discharge plasma directly above the substrate [1,103]. The critical parameters that control the diamond deposition process

include the microwave power, substrate temperature, input gas mixture and their flow rates and the chamber pressure [1,103].

Thin film diamond deposition follows a nucleation and growth process. The nucleation density has to be high to get a uniform and smooth film with small grain size and conversely, a low nucleation density results in a non-uniform rough film with large grain size. There is a competition for growth of crystals, governed by Van Der Drift's evolutionary selection, only the nuclei that reach a certain critical size survive and continue to grow and develop facets [102].

Diamond does not naturally nucleate on non-diamond substrates, such as Si, due to lattice mismatch, thereby making surface pre-treatment essential to promote a high nucleation density [103]. Commonly used pre-treatments consist of: (a) polishing the substrate with diamond paste; and (b) ultrasonication of the substrate in a diamond powder suspension [1, 103-104]. These two methods produce high nucleation density (10^8-10^{10} nuclei/cm^2) on Si substrates [104]. The pre-treatment disrupts the Si surface creating various configurations of dangling bonds required to match and stabilize the carbon sp^3 tetrahedra thereby enhancing diamond nucleation [104].

Hydrogen gas is commonly used in addition to a hydrocarbon in MPECVD processes to deposit diamond films. It plays a very important role in diamond growth process which can be listed as follows [1,105,106]:

a) It is responsible for the passivation of dangling bonds on the growth surface, which minimizes reconstruction from sp^3 to sp^2 bonding.
b) Atomic hydrogen is known to etch graphitic sp^2 carbon almost 20 times faster than diamond like sp^3 carbon. The hydrogen atoms thus serve to gasify any sp^2-

bonded non-diamond carbon impurity that forms on the growth surface, while leaving diamond clusters behind.

c) Hydrogen atoms are efficient scavengers of long-chained hydrocarbons, breaking them into smaller pieces. This prevents the build-up of polymers or large ring structures in the gas phase which can deposit on the growing surface and inhibit diamond growth.

d) Hydrogen atoms react with neutral species such as CH_4 to creative reactive radicals such as $CH_3\cdot$. Diamond grown in hydrogen rich plasma are hydrogen terminated giving it a hydrophobic surface [107].

A schematic of a generalized diamond CVD process is shown in figure 3.2 [108].

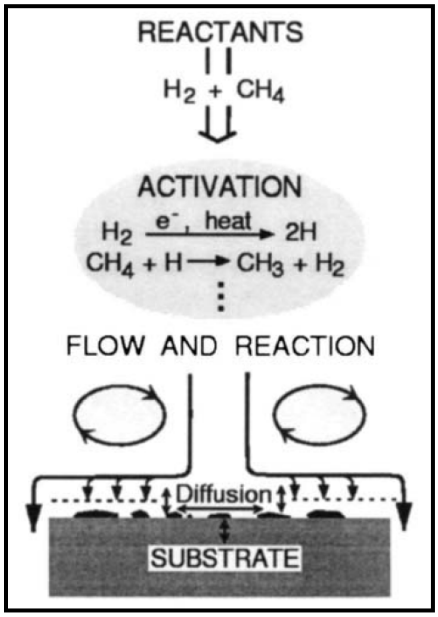

Figure 3. 2 Schematic diagram showing the principal elements in the complex diamond CVD process.

In this work, nitrogen incorporated nanodiamond films were grown on highly doped n-type silicon substrate (resistivity= 0.005 Ω-cm) with thickness of ~500μm. The surface pre-treatment consisted of mechanical polishing using diamond paste and acetone. After rinsing the substrate with acetone, methanol and de-ionized water, it was subjected to ultrasonication in nanodiamond powder slurry. The final cleaning was performed by sequential ultrasonication in acetone, methanol and de-ionized water. This combination of pre-treatment provides sufficient nucleation sites for uniform growth of the nanodiamond film. MPECVD process was used to grow the nanodiamond film using hydrogen, methane as carbon source gas while nitrogen incorporation was obtained by adding nitrogen to the input gas mixture. Table 3.1 lists the parameters used in the MPECVD process.

Table 3. 1 MPECVD process parameters for nitrogen incorporated nanodiamond growth.

Nitrogen Incorporated Nanodiamond	
Microwave Power (W)	1000
Pressure (Torr)	25
Substrate Temperature (^{o}C)	800-850
Growth Time (Hours)	5-6
Gas Flow Rates (sccm)	
Hydrogen H_2 (sccm)	135
Methane CH_4 (sccm)	15
Nitrogen N_2 (sccm)	15

3.1.2 Material Characterization- SEM, Raman Spectroscopy and XPS

The nitrogen incorporated nanodiamond film grown from the MPECVD process has a dark appearance when viewed by the naked eye. Electrical measurements showed a resistance of <10Ω on the surface at a distance of 20mm between the probes. Further material characterization was performed by using SEM, XPS and Raman spectroscopy.

The nanodiamond film microstructure was studied using a Hitachi S-4200 **scanning electron microscope (SEM)**. At low magnification, one can observe a uniform and continuous film resembling randomly oriented needles, as seen in figure 3.3(a). However, the high resolution SEM micrograph, figure 3.3(b), reveals the 'ridge' or platelet like surface morphology with a high degree of surface roughness. These interlaced 'ridges' have a thickness of only a few nanometers with nanocrystalline grains on the side walls and in between the 'ridges'. This unique surface morphology can be attributed to a combination of two competing process, nucleation and growth of the nanodiamond and etching of the graphitic content by the hydrogen plasma.

It must be emphasized here that for electrochemical applications, such as those described in this work, a smooth surface morphology is not critical. Other material properties provide us with a very effective electrode material which will be demonstrated later in this work. A profile of the nanodiamond film can be seen in the cross-sectional SEM micrograph, figure 3.3(c). The 5 hour MPECVD process yielded nitrogen incorporated nanodiamond film with a thickness of about 1.1μm at an estimated 200-250nm/hour growth rate.

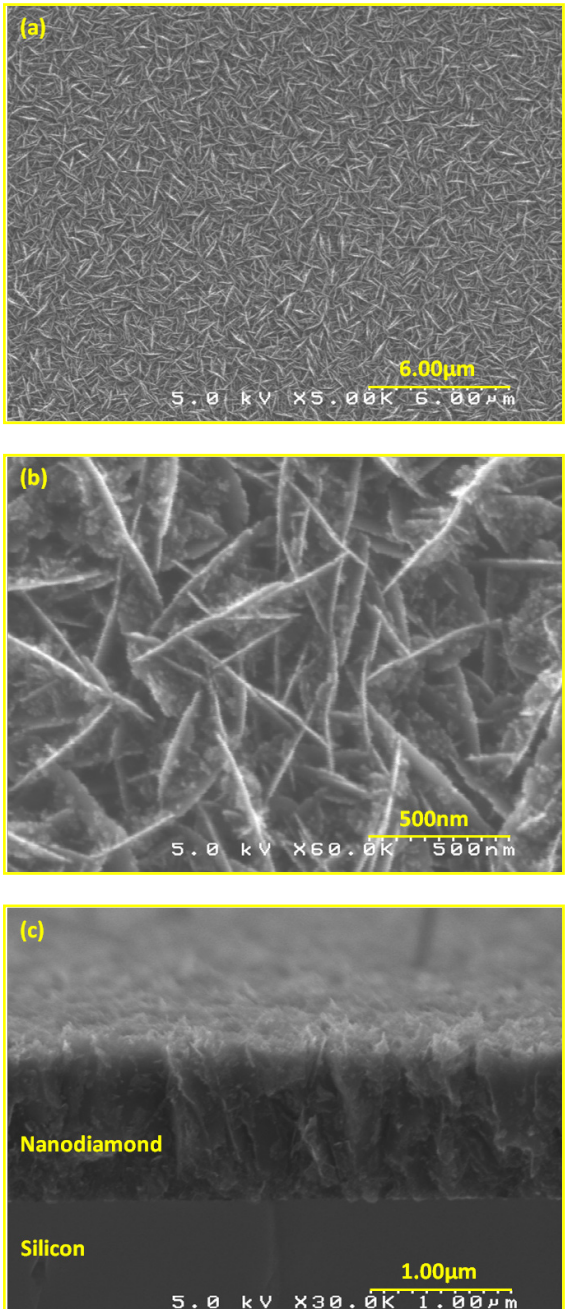

Figure 3. 3 (a) Low magnification micrograph showing a uniform nanodiamond film; (b) High resolution micrograph showing few nanometers thin 'ridge' like features with nanocrystalline grains on the side walls and in between the 'ridges'; (c) Cross sectional view of the 1.1µm thick nanodiamond film on silicon substrate.

Raman spectroscopy is a widely used diagnostic tool for evaluation of diamond and CVD diamond thin films. This method is popular because each carbon allotrope displays an easily identifiable Raman signature, it is non-destructive, requires little or no sample preparation and can made confocal so that volumes as small as 1x1x2 μm^3 can be sampled [109-111].

The Raman spectrum of bulk diamond (sp^3 hybridized carbon) is characterized by a single sharp phonon line at 1332 cm^{-1} with a FWHM (full width half maximum) of 1.2 cm^{-1} at room temperature, as seen in figure 3.4(a) [109-111].

The Raman signal of non-diamond carbon may consist of a variety of different line-shapes. In single crystal graphite (sp^2 hybridized carbon) a sharp peak is observed at 1560-1580 cm^{-1} for visible excitation, known as the G band [110-112]. In microcrystalline graphite, this is accompanied by a band at 1350-1360 cm^{-1}, known as the D band [110-112]. The G peak is due to the bond stretching of all pairs of sp^2 C atoms in both rings and chains, while the D peak is due to the breathing modes of sp^2 C atoms in rings [111-112]. Therefore, if there are no rings, D peak will not be observed [113-114]. Figure 3.4(b) shows the Raman spectrum of highly oriented pyrolitic graphite (HOPG) with the signature G and D peaks [111].

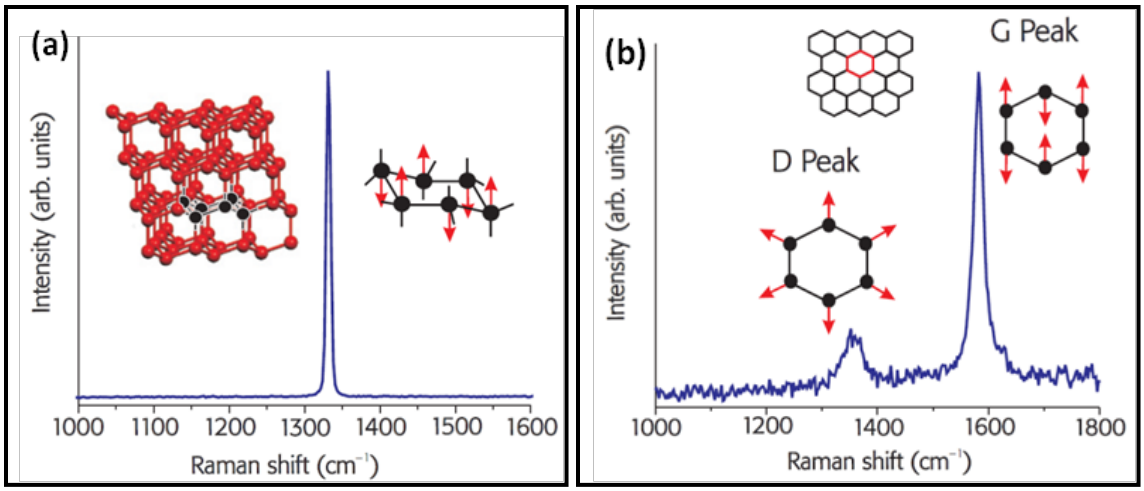

Figure 3. 4 (a) Raman spectrum of a diamond single crystal; inset- cartoon of nuclear displacement associated with this vibration. (b) Raman spectrum of highly oriented pyrolitic graphite; inset- cartoon of nuclear displacement associated with this vibration [111].

A Jobin Yvon Raman spectrometer was used to generate a Raman spectrum from the nanodiamond film as seen in figure 3.5. The excitation wavelength and the power of the laser beam employed were 632.81nm and 11mW respectively. The spectrum contains the sp^3 carbon peak at 1332 cm^{-1}, the sp^2 carbon peak at 1586cm^{-1} and also has a broad feature at 1140cm^{-1} indicative of the presence of nanocrystalline phase(s) in the nanodiamond film [115]. The relative intensities of the sp^3 and sp^2 hybridized C-C peaks are used to determine the film 'quality' which can be misleading sometimes [110,116]. Even though a large sp^2 carbon peak can be observed, the nanodiamond film still consists of a high degree of sp^3 hybridized carbon because at the given excitation wavelength, sp^2 C-C π bonds offer almost 50 times larger scattering cross section as compared to sp^3 C-C σ bonds [110,115-116].Also, the π states are resonantly enhanced at those wavelengths [111].

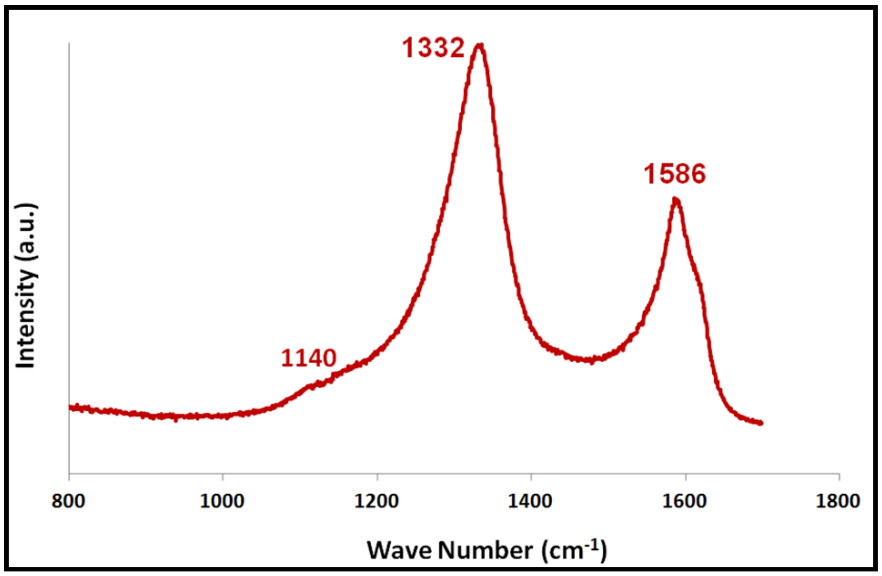

Figure 3. 5 Raman spectrum of the nitrogen incorporated nanodiamond film with the sp^3 carbon peak at 1332cm^{-1}, sp^2 carbon peak at 1586 cm^{-1} and a broad feature near 1140 cm^{-1}, commonly associated with the presence of nanocrystalline phase(s) in the film.

X-Ray photoelectron spectroscopy (XPS) is used to determine the composition of the top few nanometers of a surface. It involves bombarding the surface with x-rays, generally Al or Mg K_α emissions at 1486.6 or 1253.6eV respectively, which leads to generation of photoelectrons from the core-level of the atoms, leaving behind holes [116-117]. Based on conservation of energy, we can use equation 3.1:

$$\frac{1}{2}m_e v^2 = h\vartheta - E_B - \varphi \qquad 3.1$$

where: m_e = mass of the electron, v = electron velocity after ejection, h = Plank's constant, ϑ = frequency of incident x-ray, E_B = electron binding energy, φ = work function of the material being studied.

Equation 3.1 can be rearranged to plot E_B vs. intensity, which is the energy distribution of the photoelectrons and are characteristic of the atomic species. The binding energy of

core electrons in diamond vs. graphite or amorphous carbon shifts less than 1eV which means it is difficult to resolve contributions from sp^3 and sp^2 hybridized C [116,118]. However, deconvolution and peak fitting of C1s peak using modern software can provide information to distinguish pure carbon phases from carbon compounds or oxygenated carbon phases [116,118].

In this work, the XPS data was obtained from a Kratos X-SAM 800 system which uses Mg $K_\alpha(h\vartheta$= 1253.6 eV) radiation. The beam diameter was 5mm at a base pressure of $2x10^{-10}$ torr with an emission current of 10mA and a 90^o take off angle (normal to the analyzer). The C1s peak recorded for the nitrogen incorporated nanodiamond film is shown in figure 3.6. Deconvolution reveals 4 peaks which can be assigned based on their binding energies. The peaks at 284.6eV and 285.4eV can be assigned to sp^2 and sp^3 hybridized carbon respectively [119]. These XPS results are consistent with the Raman spectrum, i.e., the nanodiamond film has a very high sp^3/sp^2 carbon ratio. The peak at 286.5eV can be attributed to the nitrile (-C≡N) bonds, while that at 287.5eV has been reported to be from graphitic C_3N_4 [120]. This suggests that we were able to achieve nitrogen incorporation in the nanodiamond film; more supporting evidence will be presented in this chapter.

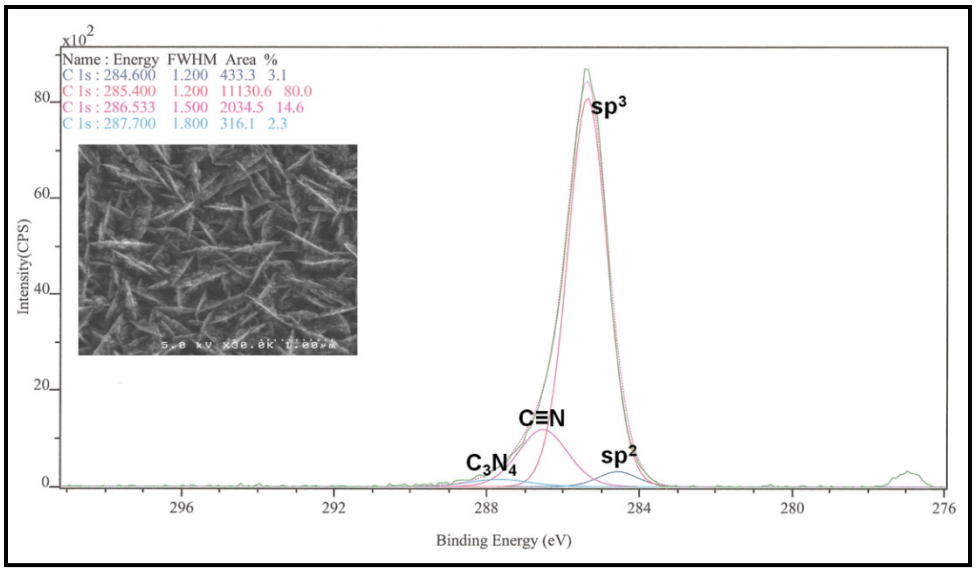

Figure 3. 6 XPS C1s peak after deconvolution, showing a high percentage of sp^3 hybridized carbon as well presence of carbon-nitrogen bonding; inset- high resolution SEM image of the nanodiamond film microstructure.

3.1.3 Electrochemistry

The electroanalytical behavior of the nanodiamond macroelectrode was studied by using cyclic voltammetry technique. A three electrode, single-cell system placed in a Faraday cage is connected to a potentiostat. The currents generated due to oxidation-reduction reactions occurring at the electrode-electrolyte interface are recorded as the applied potential is varied linearly in a triangular waveform. The current-potential plot is known as a cyclic voltammogram. The three electrodes consist of the working, reference and counter electrodes. The Faraday cage is used to provide shielding from electromagnetic interference, especially when recording very low currents, on the order of nA or pA [4].

In this work, Ag/AgCl (3M KCl) electrode was used as the reference, which is very popular due to its simple and inexpensive construction, non-toxic components and excellent stability [121]. All the potential values in this work have been reported with

respect to the Ag/AgCl reference electrode. A platinum wire was used as the counter electrode, which helps in the flow of current in the cell. Working electrodes are the cathodes where the redox processes under study occur as the potential is varied, in this case the nanodiamond film on silicon substrate.

All 3 electrodes were immersed in a supporting electrolyte which provides electrical conductivity. Only the top surface of the nanodiamond film was exposed to the electrolyte and a Viton o-ring was used to provide a leak proof seal. Electrical contact to the working electrode was made on the back side of the silicon by copper tape. The back-side was first cleaned by a cotton swab dipped in dilute HF, to remove any native oxide followed by scratching by silicon-carbide sand paper to roughen the surface which provides a better electrical contact with the copper tape. A schematic of the flat cell in a 3 electrode configuration can be seen in figure 3.7(a). A CH Instruments CHI660C analyzer was used to perform the cyclic voltammetric experiments using the built-in signal generator and data analyzer. Figure 3.7(b) shows the CHI660C work station used in this work.

Initial characterization of the nanodiamond macroelectrode was performed by using the ferri-ferrocyanide redox couple $\mathbf{Fe(CN)_6^{-3/-4}}$ in 0.1M KCl as the supporting electrolyte. This redox reaction is accompanied with the transfer of one e^-; ferrocyanide is oxidized to form ferricyanide, as depicted by the following reaction.

$$Fe(CN)_6^{4-} \quad \leftrightarrows \quad Fe(CN)_6^{3-} + e^-$$

$$ferrocyanide \qquad ferricyanide$$

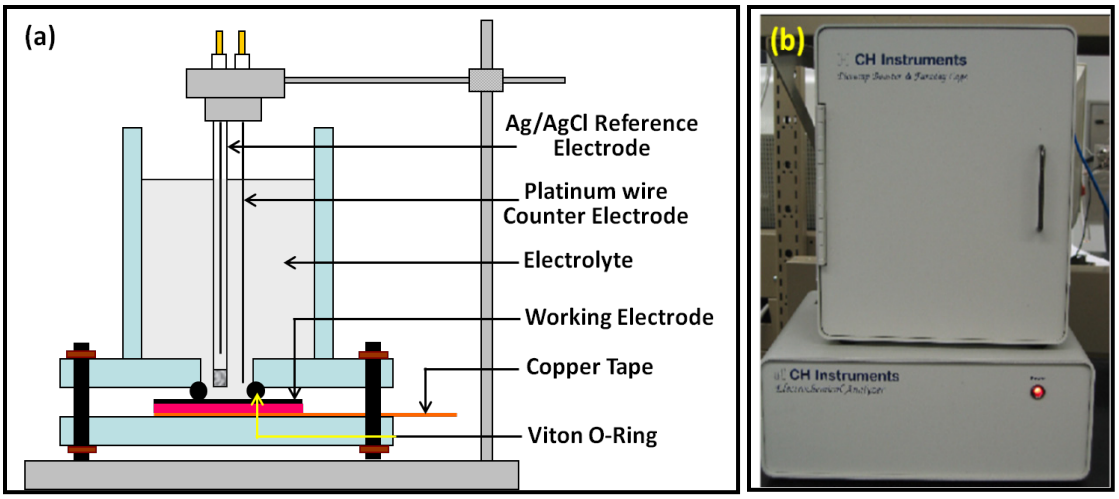

Figure 3. 7 (a) Schematic diagram of a flat cell in a 3-electrode configuration with the nanodiamond film as the working electrode, a platinum wire as the counter electrode and a Ag/AgCl reference electrode. (b) A photograph of the CHI660C electrochemical analyzer work station.

A cyclic voltammogram (CV) recorded in 0.1M KCl at 100mV/s scan rate reveals a wide working potential window of about 3V which is suitable for detecting a wide variety of analytes. This current is also called as the background current and arises due to non-faradaic processes unrelated to the redox reaction of interest. When a solid surface is in contact with an aqueous solution, a double layer capacitor is formed near the interface due to a distribution of charges and/or oriented dipoles to counter the excess charge on the solid electrode [122]. This phenomenon cannot be avoided and generates the background currents due to capacitive charging. The background CV can be seen in figure 3.8, which also shows large over-potential for oxygen and hydrogen evolution. Two reduction peaks are also seen at about 0.75V and -1.50V which can be attributed to oxygen reduction reaction and secondary redox reactions due to functional groups present at the surface.

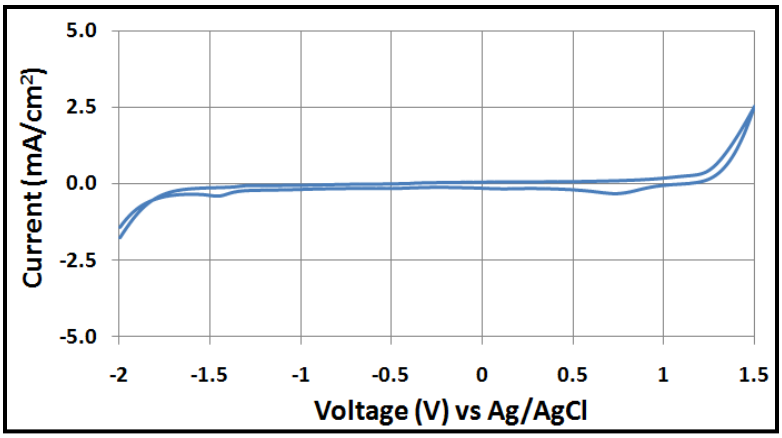

Figure 3. 8 Background CV recorded at a scan rate of 100mV/s in 0.1M KCl as the supporting electrolyte showing a wide working potential window of about 3V.

To study the ferri/ferrocyanide redox reactions, a stock solution of 20mM **potassium ferrocyanide [$K_4Fe(CN)_6$]** was made with deionized water and added to the electrolyte to obtain the desired concentration. CVs for different concentrations of ferrocyanide were recorded at 100mV/s; 1mM, 2mM, 3.9mM, 5.9mM, 8mM and 10mM, as seen in figure 3.9. As per the convention used, the positive currents represent oxidation current while negative values correspond to the reduction current. Distinct oxidation and reduction peaks are observed which are consistent with semi-infinite linear diffusion limited mass transport of the analyte [34]. The peak current for a reversible couple is given by the Randles-Sevčik equation number 3.2 [5].

$$i_p = (2.69 \times 10^5) n^{\frac{3}{2}} A C D^{\frac{1}{2}} \vartheta^{\frac{1}{2}} \qquad 3.2$$

where; i_p= peak current (amperes), n= number of electrons, A= electrode area (cm^2), C= concentration ($mol.cm^{-3}$), D= diffusion coefficient ($cm^2.s^{-1}$) and ϑ= scan rate ($V.s^{-1}$).

From equation 3.2, one can see that the peak current is directly proportional to the analyte concentration and increases with the square root of the scan rate. This response

can be observed in figure 3.9, the anodic and cathodic peak heights increase as we increase ferrocyanide concentration from 1mM to 10mM. The plot of the peak oxidation currents vs. the ferrocyanide concentration is also known as the calibration curve, seen in figure 3.10. This electrode has a linear dynamic range of 1mM-10mM $Fe(CN)_6^{4-}$. The slope of the curve gives the sensitivity of the electrode for detection of ferrocyanide, which in this case is **85µA/cm^2 per mM** of $Fe(CN)_6^{4-}$.The formal potential (E^o) of the redox process, which is centered between the anodic and cathodic peak potentials, is 0.22V vs. Ag/AgCl reference electrode. The peak-peak separation, ΔE_p, is as low as 73mV which is close to but greater than the theoretical value of 59mV for a perfectly reversible, one electron transfer redox reaction and the ratio of peak oxidation to peak reduction currents approach unity [5]. The low ΔE_p value indicates relatively rapid electrode reaction kinetics.

Based on Randles-Sevčik equation, one can see that the peak current is directly proportional to the square root of the scan rate. However, the double layer capacitance generates non-faradaic currents associated with its charging/discharging. This capacitive current varies linearly with the scan rate as per equation 3.3.

$$\boldsymbol{i_c = AC_d\vartheta} \qquad \mathbf{3.3}$$

where; i_c= capacitive current (A), A= electrode area (cm^2), C_d= differential capacitance (F/cm^2) and ν= scan rate (V/s).

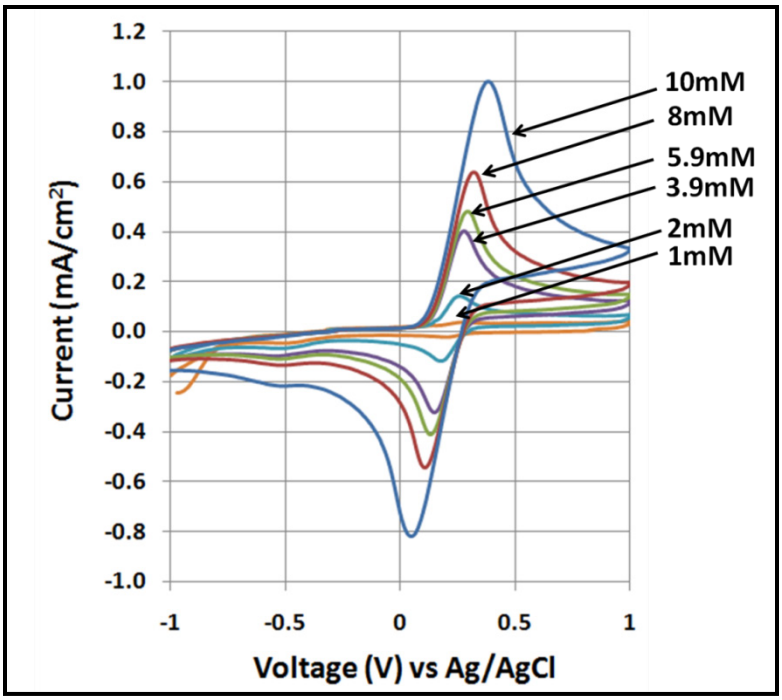

Figure 3. 9 CVs recorded for different concentrations of potassium ferrocyanide (1mM, 2mM, 3.9mM, 5.9mM, 8mM and 10mM) recorded at 100mV/s in 0.1M KCl as the supporting electrolyte.

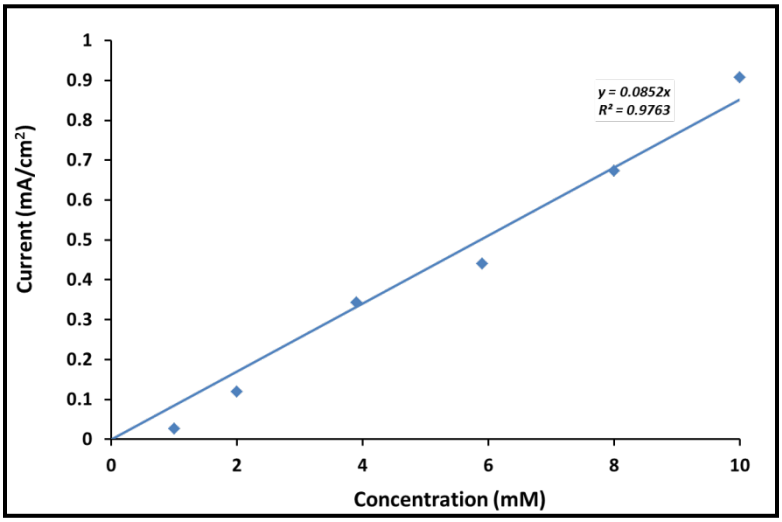

Figure 3. 10 Linear calibration plot derived from the peak oxidation currents (mA/cm^2) obtained from different ferrocyanide concentrations (mM) at 100mV/s scan rate.

CVs recorded for 10mM ferrocyanide in 0.1M KCl at multiple scan rates, 10mV/s, 50mV/s, 100mV/s, 250mV/s and 500mV/s, can be seen in figure 3.11. The CVs retain the peak shaped response, but the oxidation and reduction peak heights increase as the scan rates increase, because of increase in the capacitive currents. The oxidation (reduction) peak position becomes more positive (negative) and the peak-peak separation increases as the scan rate increases due to effect of reaction kinetics on the electrode response. A linear plot between the peak oxidation currents and the square root of the scan rates can be seen in figure 3.12, which is consistent with semi-infinite linear diffusion or planar diffusion of the analyte to the electrode surface. By using Nicholson method, we can calculate the apparent rate constant (k_{app}^{o}), as a function of ν by correlating the variation of ΔE_p with ν and then from the variation with the dimensionless parameter Ψ given by equation 3.4 [4].

$$\boldsymbol{\Psi = \frac{(\frac{D_O}{D_R})^{\alpha/2}\, k_{app}^{o}}{(\pi D_O f \vartheta)^{1/2}}} \qquad \mathbf{3.4}$$

where; D_O and D_R= diffusion coefficients of the oxidized and reduced forms (cm^2/s), f = (nF/RT), F= Faraday's constant (96500C/mol), n= number of electrons, R= gas constant (8.314 $J.mol^{-1}.K^{-1}$), T= temperature (293K), ϑ= scan rate, α= charge transfer coefficient and k_{app}^{o}= apparent heterogeneous rate constant(cm/s). In these calculations, we assume α=0.5 and D_O=D_R, which gives us k_{app}^{o} value of $7x10^{-3}$ cm/s. This is less than that reported for H-terminated boron doped microcrystalline diamond (BDD) and nanodiamond films (10^{-1}-10^{-2} cm/s) but greater than oxidized/ oxygen terminated BDD ($3x10^{-4}$ cm/s) [3, 123].

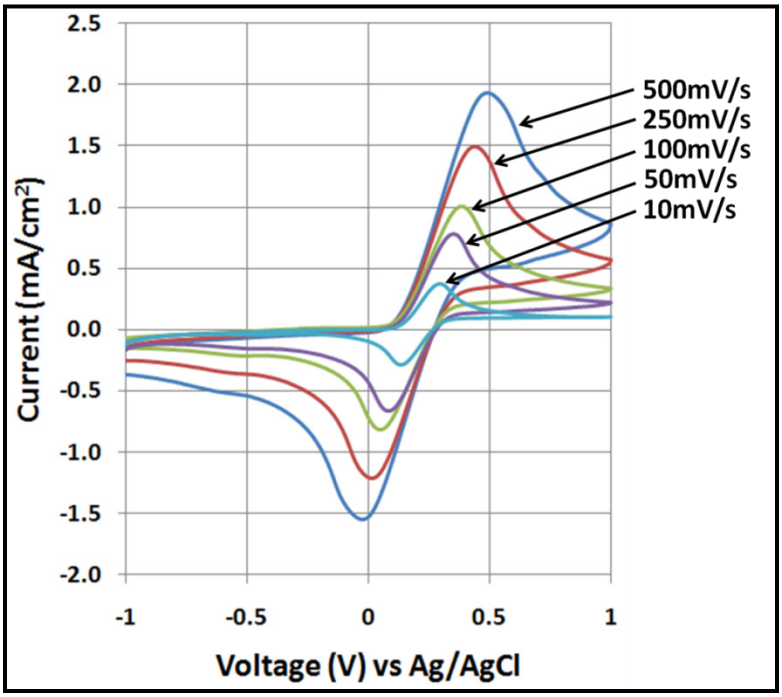

Figure 3. 11 CVs recorded for 10mM potassium ferrocyanide recorded at different scan rates (10mV/s, 50mV/s, 100mV/s, 250mV/s and 500mV/s) in 0.1M KCl as the supporting electrolyte.

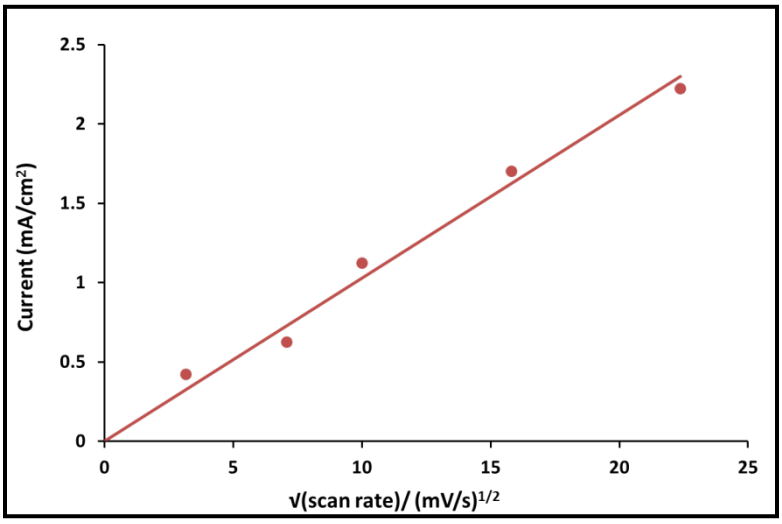

Figure 3. 12 Linear plot derived from the peak oxidation currents (mA/cm^2) vs square root of the scan rate $(mV/s)^{1/2}$, for 10mM ferrocyanide in 0.1M KCl.

Chronocoulometry technique was applied to calculate the electrochemically active area of the macro electrode. This technique involves application of a potential step under conditions of large over-potential so that the redox process is controlled entirely by diffusion of the analyte to the electrode [6]. Figure 3.13 shows one step chronocoulometry curves, q vs. t, recorded for different ferrocyanide concentrations. The time dependence of the current is given by the Cottrell equation, 2.1.The integral of equation 2.1 will give us the time dependence of the charge consumed, as given by equation 3.5

$$q(t) = 2nFAC_o^* D_o^{1/2} \pi^{-1/2} t^{1/2} \qquad 3.5$$

The slope of equation 3.5 can be used to calculate the active area, by substituting the values of F= 96500C/mol, D_o=7.35 × 10^{-6}cm^2.s^{-1}, n=1 and C_o^* (1mM to 10mM). Based on this data, the area calculated was 0.6cm^2, which is close to an estimated geometric area of 0.7 cm^2.

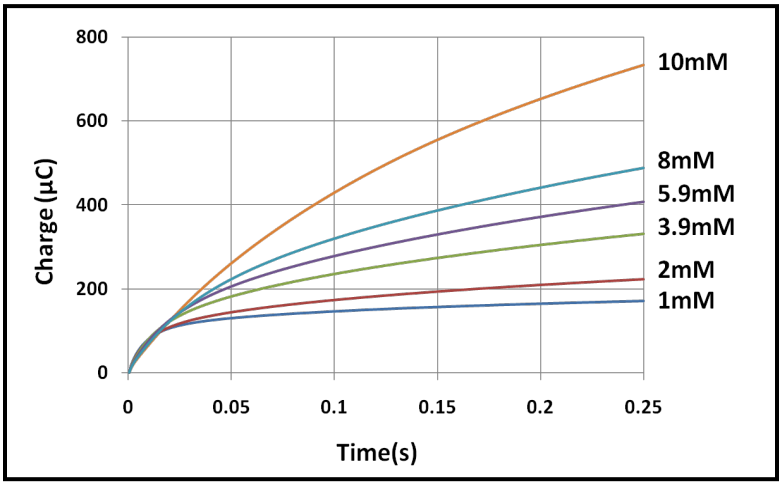

Figure 3. 13 One step Chronocoulometry plots recorded for different ferrocyanide concentrations in 0.1M KCl as the supporting electrolyte.

The nitrogen incorporated nanodiamond macroelectrode was used to detect **dopamine (DA)**, which is an important catecholamine neurotransmitter and plays a significant role in the functioning of the central nervous, cardiovascular, renal, and hormonal systems as well as in drug addiction and Parkinson's disease [21]. Cyclic voltammetry was performed by using different concentrations of DA solutions in 0.1M phosphate buffered saline (PBS) at the physiologic pH of 7.4. A stock solution of 10mM DA was made from which fixed amounts were titrated into the PBS solution to achieve the desired concentrations. The PBS solution was made from a pre-mixed powder mixture of sodium chloride (NaCl), potassium chloride (KCl), sodium phosphate (Na_2HPO_4) and potassium phosphate (K_2HPO_4) of fixed concentrations. This buffer solution helps to maintain constant pH and mimics the physiologic ionic concentrations.

A background CV at 100mV/s scan rate in 0.1M PBS solution at pH 7.4, as shown in figure 3.14, reveals a wide working potential window of about 3V, which is comparable to about 3.5V observed for boron doped diamond electrodes [107].

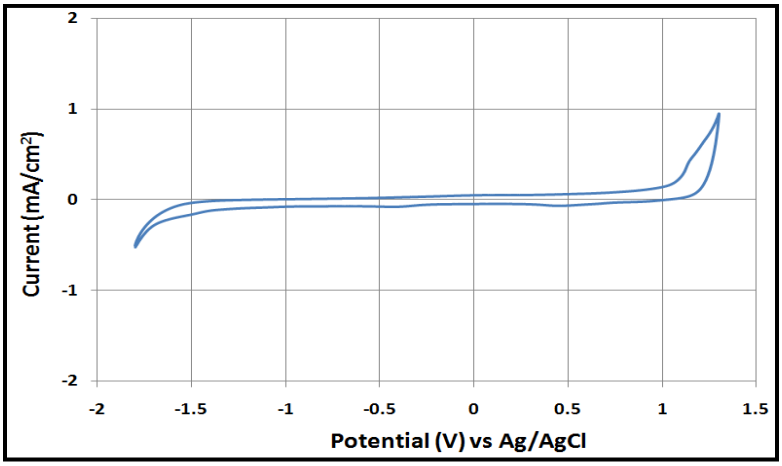

Figure 3. 14 CV recorded in 0.1M PBS supporting electrolyte at 100mV/s scan rate and pH 7.4, showing a wide working potential window of about 3V, as compared to about 3.5V seen for boron doped diamond.

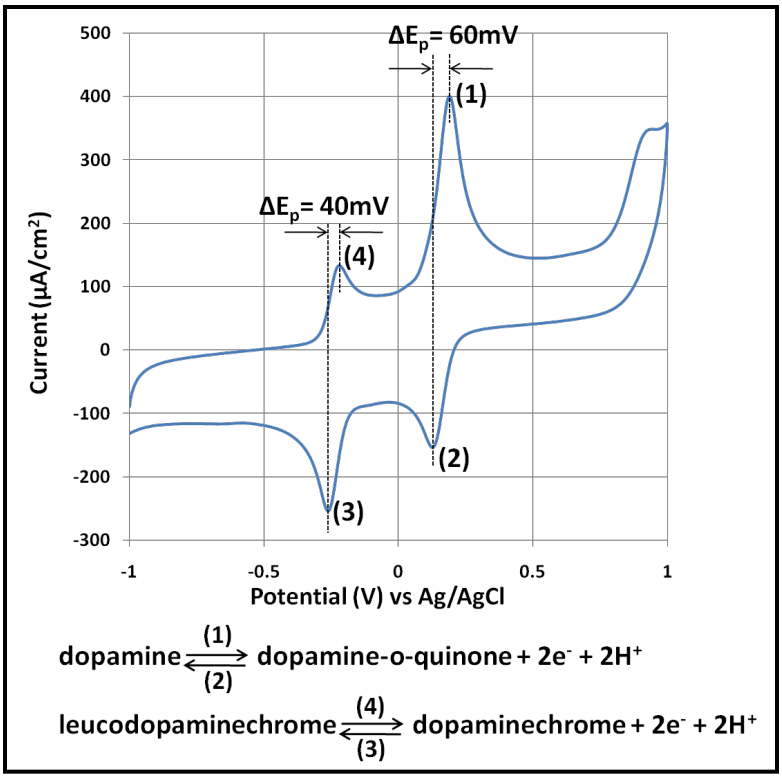

Figure 3. 15 CV recorded for 1000µM DA in 0.1M PBS as the supporting electrolyte at 100mV/s scan rate and pH 7.4 distinctly showing 2 sets of redox peaks, consistent with diffusion limited mass transport. The peak-peak separation values suggest quasi-reversible reaction kinetics for the 2 redox couples. Peaks 1 and 2 correspond to the DA/DAQ redox couple while peaks 3 and 4 can be assigned to the LDAC/DAC redox couple.

For a perfectly reversible couple involving a transfer of n e^-, the peak-peak separation (ΔE_p) is given by equation 3.6.

$$\Delta E_p = \left(E_{p,a} - E_{p,c}\right) = \frac{0.059}{n} V \qquad 3.6$$

where; $E_{p,a}$= anodic peak potential (V) and $E_{p,c}$= cathodic peak potential (V). In the present context, the ΔE_p value should be about 29mV. The separation between peaks 1 and 2 is about 60mV while that between peaks 3 and 4 is only 40mV. These calculations do not include variations in peak potentials arising from iR_u losses due to uncompensated resistance in the cell. The ΔE_p values are consistent with quasi-reversible reaction

kinetics. The ratio of peak currents (peak 1/peak 2) is less than 1 (*equals to 1 for perfectly reversible process*) due to the fact that an irreversible chemical reaction occurs after DA is oxidized to DAQ and consequently lesser amount is available to be reduced back to DA. These reactions are categorized as an ECE process, discussed previously in section 2.4.2. A comparative study using highly **boron doped diamond film** for DA (1000µM, 0.1V/s) detection reveals a response with very sluggish and irreversible reaction kinetics and a large ΔE_p of nearly 250-300mV [72]. This highlights the superior sensitivity of the nitrogen-incorporated nanodiamond film electrode for detection of DA.

Cyclic voltammograms for different DA concentrations (100µM, 200µM, 400µM, 600µM, 800µM and 1000µM) were recorded in 0.1M PBS at pH 7.4 at 100mV/s scan rate, seen in figure 3.16. Planar diffusion limited mass transport produces peak shaped response showing two pairs of redox peaks corresponding to the DA/DAQ and LDAC/DAC redox couples. The oxidation and reduction peak heights increase with increase in DA concentration and a linear calibration curve can be obtained by plotting the peak oxidation current for DA (µA/cm^2) versus DA concentration (µM). The slope of the plot, as seen in figure 3.16, represents the sensitivity of the electrode for DA detection in the linear dynamic range of 100µM-1000µM, which is about **0.3µA/cm^2 per µM.**

The limit of detection of DA using cyclic voltammetry can be calculated by using by using equation 3.7 [124]:

$$\boldsymbol{L.O.D.} = \frac{\boldsymbol{3\sigma}}{\boldsymbol{slope}} \qquad \mathbf{3.7}$$

where: L.O.D. = limit of detection, σ= standard deviation of the background current around the peak and slope= sensitivity. This gives us a value of 3.63µM of DA.

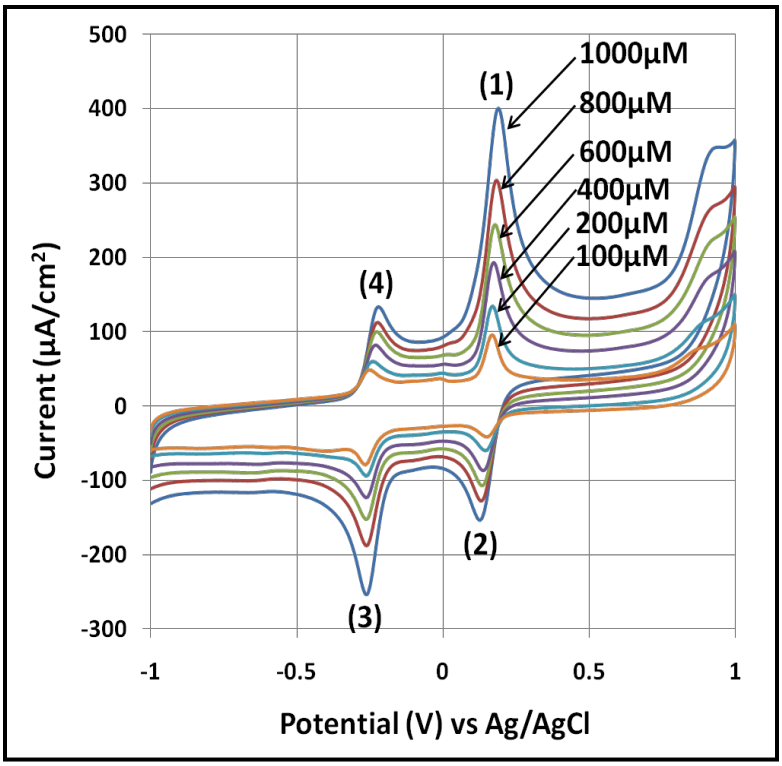

Figure 3. 16 CVs recorded for different DA concentrations in 0.1M PBS as the supporting electrolyte at 100mV/s scan rate and pH 7.4 distinctly show 2 sets of redox peaks, consistent with diffusion limited mass transport. The peak heights increase with increase in DA concentration. Peaks 1 and 2 correspond to the DA/DAQ redox couple while peaks 3 and 4 can be assigned to the LDAC/DAC redox couple.

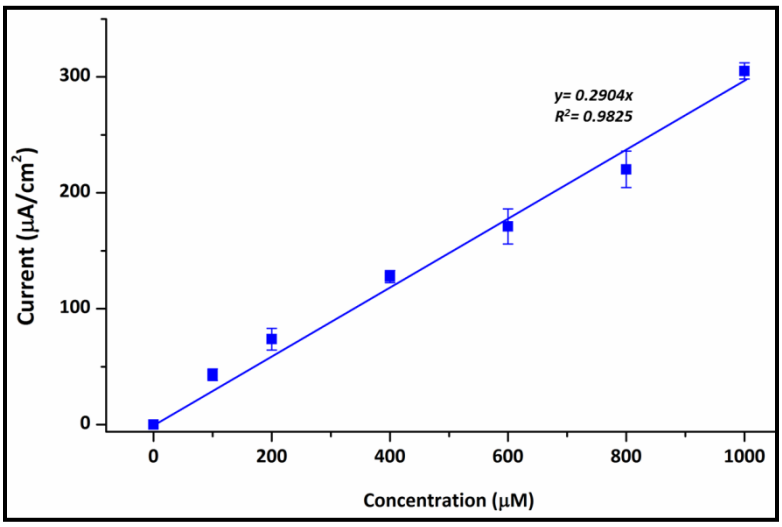

Figure 3. 17 Linear calibration curve plotted by using the peak oxidation currents ($\mu A/cm^2$) for DA/DAQ redox couple versus corresponding DA concentrations (µM). Error bars represent standard deviation.

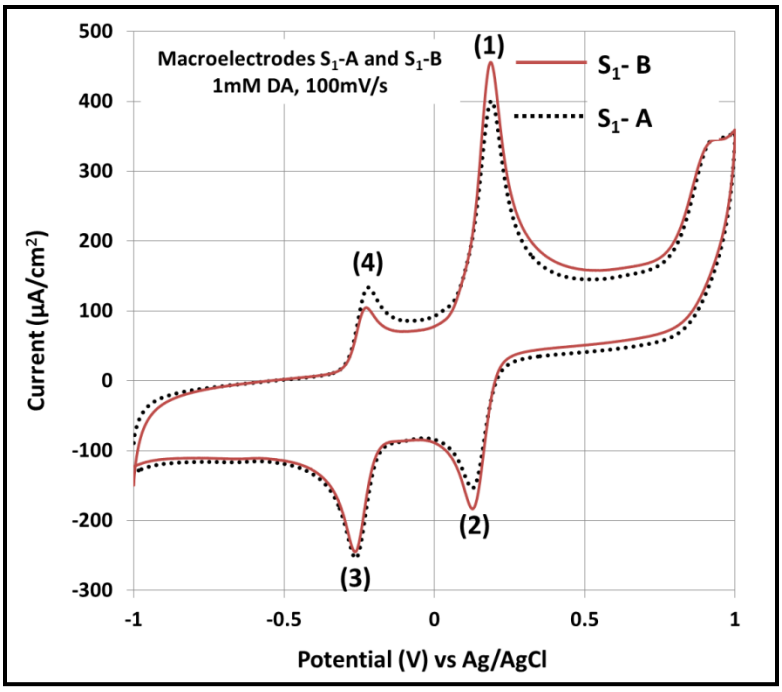

Figure 3. 18 CVs recorded from two nanodiamond macroelectrodes fabricated using the same parameters for 1mM DA in 0.1M PBS solution at a scan rate of 100mV/s. The CV in the dotted line corresponds to the baseline electrode, S_1-A, while the CV in solid line was recorded using the second electrode S_1-B.

In order to evaluate the consistency of the electroanalytical performance of the nanodiamond macroelectrodes, a second macroelectrode was fabricated using the same MPECVD parameters on highly doped n type silicon substrate. These electrodes were labeled as S_1- A, which was the baseline against which the response of the second electrode, S_1- B, was examined. CVs recorded for **1mM DA** in 0.1M PBS at pH 7.4 and a scan rate of 100mV/s can be seen in figure 3.18, S_1- A CV in dotted line and S_1- B CV in the solid line.

The two cyclic voltammograms show very close overlap. The peak locations of (1) and (2) differ by 2mV and 1mV respectively, between S_1-A and S_1-B. The peak oxidation and reduction currents for the DA/DAQ redox couple ((1) and (2)) are higher in

case of S_1-B, however, the current values for peak (3) and especially peak (4), are relatively greater for S_1-A. The DAC/LDAC redox couple (peaks (3) and (4)) arise due to reactions occurring downstream of DA oxidation which leads to its gradual depletion. This could explain the lower peak currents for (1) and (2) and higher peak currents for (3) and (4) observed for S_1-A as compared to S_1-B. The difference in the peak (1) oxidation current was calculated to be **68nA/cm^2** per μM of DA. It must be stressed that prior to use in electroanalysis, each electrode undergoes individual calibration which compensates any differences in response between any two or more electrodes, such as seen in this case.

Ascorbic acid (AA) is a commonly occurring bio-analyte in the extra cellular fluid of the central nervous system and acts as an interferant in the detection of catecholamines such as DA because of very close oxidation potentials. Ascorbic acid undergoes oxidation to form dehydroascorbate (DHA) along with the transfer of 2 electrons and 2 protons.

The CVs recorded for different AA concentrations (100μM, 200μM, 400μM, 600μM, 800μM and 1000μM) can be seen in figure 3.19. A distinct oxidation peak can be observed at around 0V with a small reduction peak (at higher concentrations) at around -0.1V, which suggest irreversible reaction kinetics for AA/DHA redox couple. The reduction peak near -0.45V is due to reduction of surface oxygen functional groups and dissolved oxygen generated during the forward sweep and is not related to the AA/DHA redox couple [125]. The calibration curve plotted using the peak oxidation currents (μA/cm^2) with the corresponding AA concentrations (μM) is seen in figure 3.20. The nanodiamond film macroelectrode shows a linear response with a dynamic range of

100µM-1000µM, a sensitivity value of **0.14µA/cm^2 per µM of AA** and a L.O.D. of 7.77µM.

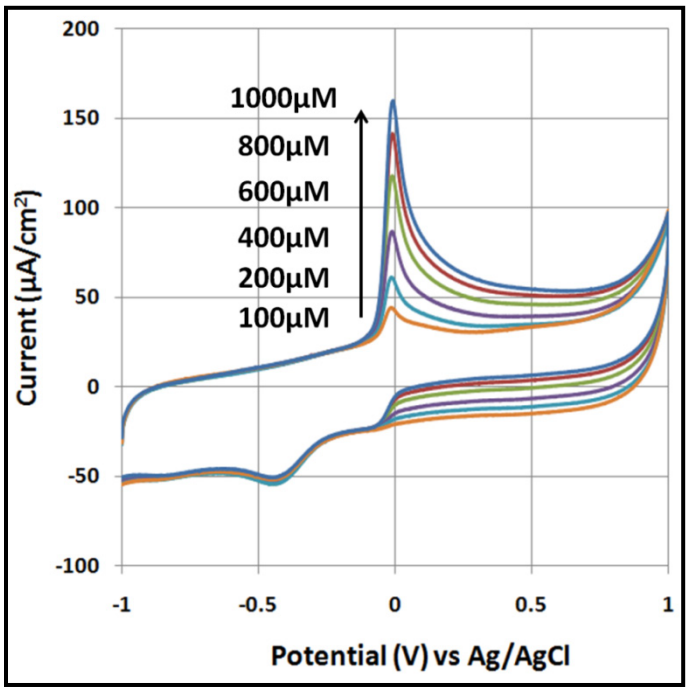

Figure 3. 19 CVs recorded for different AA concentrations in 0.1M PBS as the supporting electrolyte at 100mV/s scan rate and pH 7.4 showing a sharp peak near 0V corresponding to the oxidation of AA to dehydroascorbate.

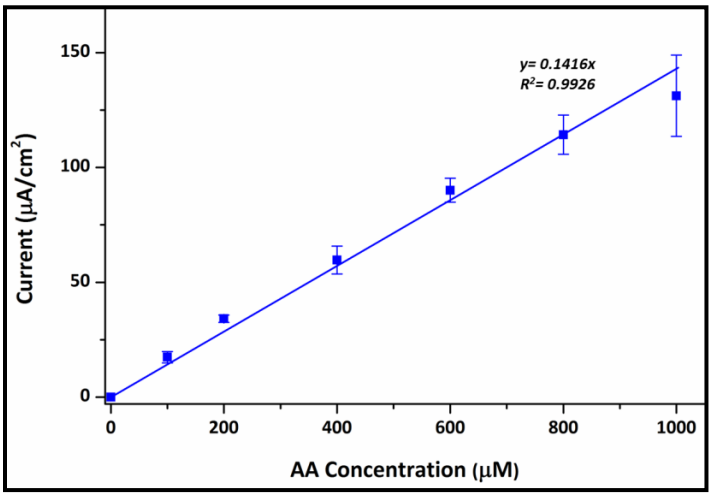

Figure 3. 20 Linear calibration curve plotted by using the peak oxidation currents (µA/cm^2) for AA versus corresponding AA concentrations (µM). Error bars represent standard deviation.

Uric acid (UA) is also an important bio-analyte which can be detected by using electrochemical techniques. The end product of UA oxidation is allantoin, but the electrochemical oxidation is a complex process that proceeds in multiple steps [126-128]. A proposed oxidation pathway for UA has been discussed in detail in appendix A. The oxidation potential of UA lies close to that of DA and AA which makes selective detection of either one of these bio-molecules difficult.

The CV recorded for 200µM UA at 100mV/s in 0.1M PBS (pH 7.4) with the individual redox peaks labeled can be seen in figure 3.21(a). The CVs recorded for increasing concentrations of UA (100µM, 200µM, 400µM, 600µM, 800µM and 1000µM) can be seen in figure 3.21(b) showing sharp and very distinct peaks at 0.331V for UA oxidation. Inset of figure 3.21(b) is a close up of a section of the CVs (from 0.2V to 0.8V).

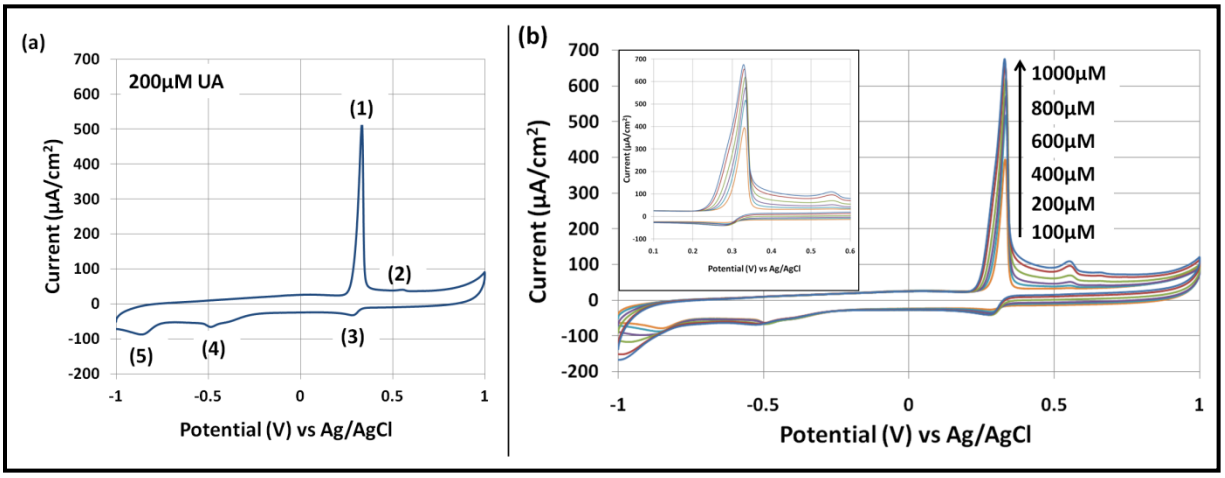

Figure 3. 21 (a) CV recorded for 200µM UA at 100mV/s in 0.1M PBS with the oxidation and reduction peaks labeled. (b) CVs recorded for increasing UA concentrations in 0.1M at 100mV/s in 0.1M PBS (pH7.4); inset- close-up of the UA oxidation peak.

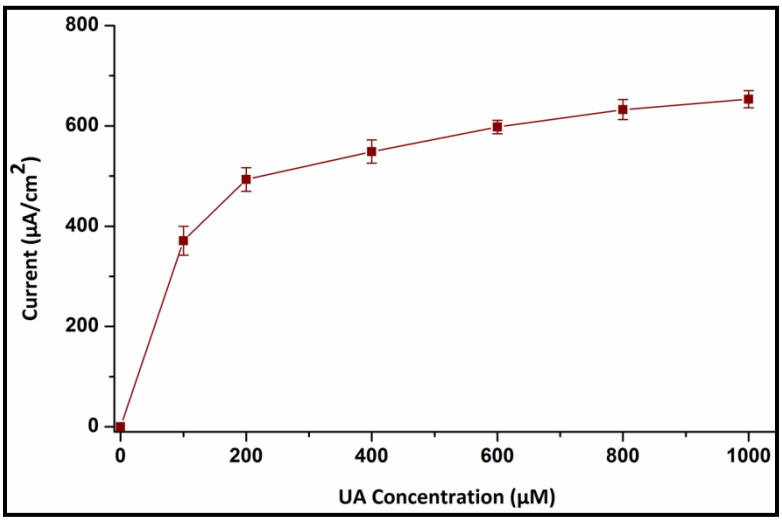

Figure 3. 22 Calibration curve plotted by using the peak oxidation currents (peak 1) ($\mu A/cm^2$) for UA versus corresponding UA concentrations (μM). Error bars represent standard deviation.

The calibration curve plotted using the peak 1 oxidation current is shown in figure 3.22. The oxidation current increases with increase in UA concentration but has a non-linear response. One of the reasons could be adsorption of the products of the reactions downstream of UA oxidation on the electrode surface. By stirring the solution, the signal from UA oxidation increased back to the original values, which suggests that the surface adsorption process is reversible. There is no "fouling" of the electrode.

Based on the experimental results, the excellent sensitivity of nitrogen incorporated nanodiamond electrode for DA, AA and UA detection has been demonstrated. In addition to that, the large separation between the respective oxidation potentials provides a high resolution and easy identification of the individual species when mixed together in a solution. **The $\Delta E_{p,\ ox}$ (oxidation peak potential separation between AA and DA) is about 190mVand $\Delta E_{p,\ ox}$ (between DA and UA) is about**

150mV. These large values have been achieved without any surface modification or functionalization, unmatched by boron doped diamond electrodes.

The CV for a **mixture of 1mM DA, 1mM AA and 1mM UA** recorded at 100mV/s in 0.1M PBS at the physiologic pH can been seen in figure 3.23. The oxidation-reduction peaks have been labeled and the corresponding reactions have been listed underneath. The CV contains distinct peaks corresponding to AA, DA and UA oxidation, peaks 1, 2 and 3 respectively. In addition, the redox peaks due to the LDAC/DAC redox couple (peaks 6 and 7) are also observed.

To further test the electrode selectivity, increasing concentrations of DA (100μM, 200μM, 400μM, 600μM, 800μM, 1000μM) were added to a solution of 0.1M PBS while the concentrations of AA and UA were held constant at 1mM. The resulting CVs recorded at 100mV/s can be seen in figure 3.24. The peak oxidation current for DA increases with increasing DA concentration, as predicted by Randles-Sevčik equation.

The calibration curve plotted between the peak oxidation current ($\mu A/cm^2$) versus the DA concentration (μM) shows a linear relationship, as seen in figure 3.25, with a dynamic range of 100μM-1000μM and sensitivity value of **0.25μA/cm^2 per μM of DA** as compared to 0.3$\mu A/cm^2$ per μM in absence of AA and UA**.** The curve does not pass through the origin because the current measurements are not made with respect to the true background signal. Instead, in such multi-component systems, the section of the curve (the valley or the minima) between peaks 1 and 2 is used as the baseline. Therefore, the signal reported is off-set by the contribution from peak 1. The L.O.D. for DA in solution with 1mM AA and 1mM UA is 4.41μM, which is close to that calculated for DA solution, 3.63μM.

Performance of nitrogen-incorporated nanodiamond electrodes have been compared with results from other electrode materials for detection of ferrocyanide and DA in appendix B; tables B.1 and B.2

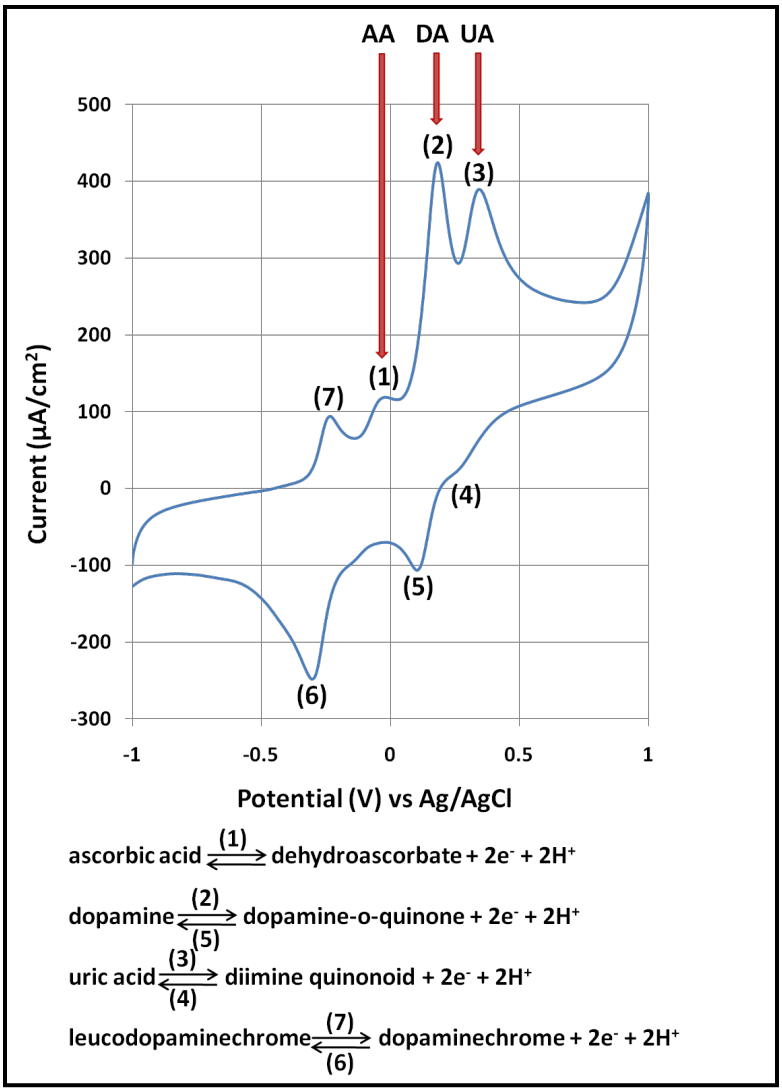

Figure 3. 23 CV recorded for a solution of 1mM AA, 1mM DA and 1mM UA at 100mV/s scan rate in 0.1M PBS (pH7.4) as the supporting electrolyte. The oxidation peaks for AA, DA and UA are well resolved and easily identifiable.

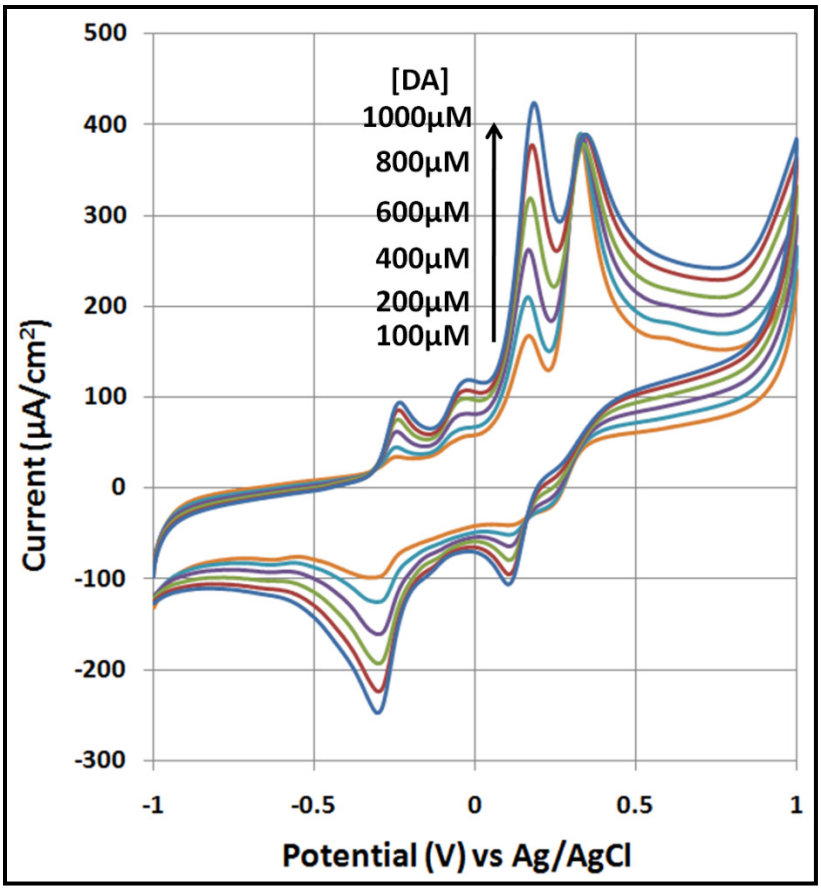

Figure 3. 24 CVs recorded for increasing concentrations of DA in a solution of 1mM AA, and 1mM UA at 100mV/s scan rate in 0.1M PBS (pH7.4) as the supporting electrolyte. The oxidation peak current for DA increases with increase in DA concentration. The electrode is able to maintain excellent resolution and selectivity for all 3 bio-analytes.

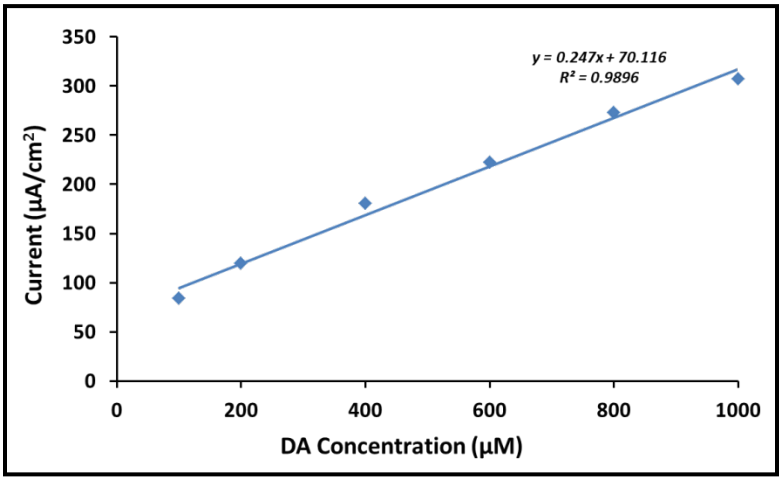

Figure 3. 25 Calibration curve plotted by using the peak oxidation currents for DA (peak 1) ($\mu A/cm^2$) versus corresponding DA concentrations (µM).

3.2 Effect of CH_4:H_2 gas flow rates- Fabrication and material characterization

Experiments to study the effect of varying CH_4:H_2 ratio in the input gas mixture on nanodiamond film growth and the resulting material properties were performed. All the samples underwent the same surface pre-treatment and cleaning steps as undertaken previously. MPECVD process was used to grow nanodiamond films on these substrates using similar power, pressure and temperature conditions. The total gas flow rate was fixed at 165 sccm while varying CH_4 and H_2 gas flow rates. The nitrogen flow rate was adjusted to maintain the total input gas flow. The various parameters used have been summarized in table 3.2.

At the end of the MPECVD process, all the samples, A through D, were analyzed under the SEM to study their microstructure. Low magnification SEM micrographs can be seen in figure 3.26 (A), (B), (C) and (D) with the corresponding high resolution images in the inset. In each case, there was very sparse growth of nanodiamond and the microstructures appeared to be similar with small grain size. Plasma etching due to hydrogen or nitrogen ions as the only reason can be ruled out because subsequent studies with higher hydrogen and nitrogen gas flow rates yielded uniform and continuous films. Clearly, these conditions are not conducive for uniform nucleation on the substrates, probably due to extremely short lifetimes of the reaction intermediates produced in the plasma. Lack of uniform and continuous films rendered these samples ineffective for use in electrochemical studies.

Table 3. 2 MPECVD process parameters for nitrogen incorporated nanodiamond growth.

Microwave Power (W) 1000 **Pressure (Torr)** 25 **Substrate Temperature (^{o}C)** 800-850 **Growth Time (Hours)** 3				
Gas Flow Rates (sccm)				
Samples	**A**	**B**	**C**	**D**
H_2	60	75	90	105
CH_4	15	15	15	15
N_2	90	75	60	45
CH_4:H_2	***1:4***	***1:5***	***1:6***	***1:7***

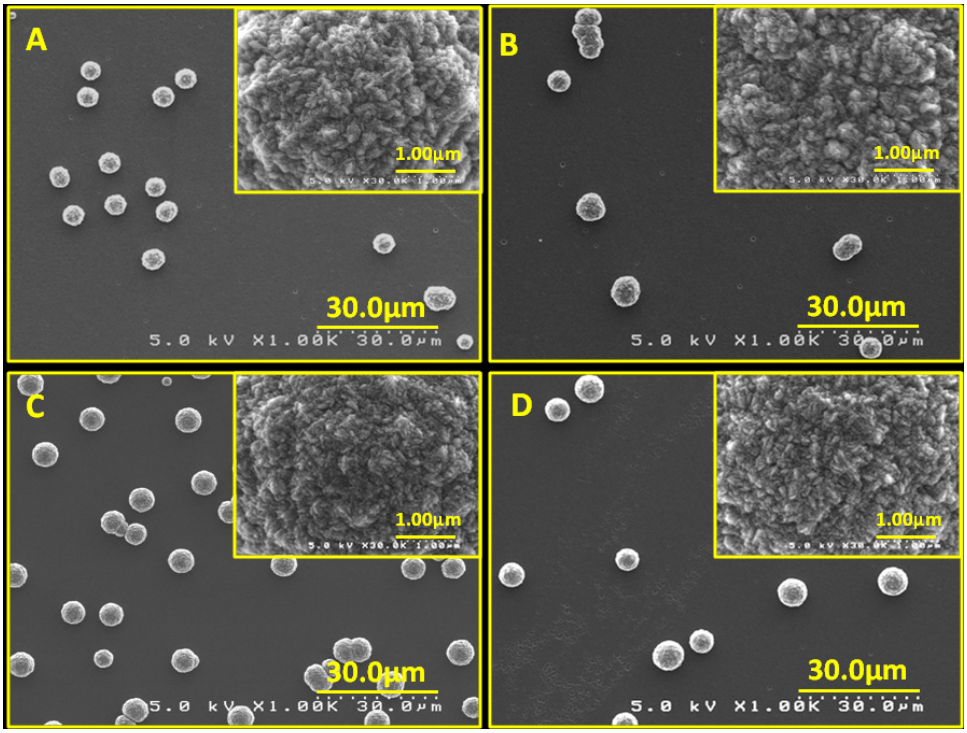

Figure 3. 26 SEM micrographs at low and high resolution (in inset) for samples A (1:4), B (1:5), C (1:6) and D (1:7) showing sparse and discontinuous nanodiamond growth.

3.3 Optimizing material properties for electroanalytical applications

3.3.1 Fabrication of nanodiamond macroelectrodes with varying nitrogen composition

Research has shown that addition of nitrogen gas to the input gas mixture in the MPECVD process has a significant impact on the material properties of nanodiamond film, especially the electrical conductivity [129-133]. The next series of experiments were performed to examine the effect of a wide range of nitrogen composition (%) in the hydrogen rich input gas mixture. The hydrogen and methane flow rates were kept constant while that of nitrogen was increased proportionally to 30 sccm, 60 sccm and 90 sccm. The nanodiamond film previously grown was used as our baseline for comparison and is labeled as sample S_1. The MPECVD process parameters have been listed in table 3.3.

Table 3. 3 MPECVD process parameters for nitrogen incorporated nanodiamond growth.

Microwave Power (W) 1000, **Pressure (Torr)** 25, **Substrate Temperature (^oC)** 800-850, **Growth Time (Hours) 5**				
Gas Flow Rates (sccm)				
Sample	**S_1**	**S_2**	**S_3**	**S_4**
H_2	***135***	135	135	135
CH_4	***15***	15	15	15
N_2	***15***	30	60	90
N_2:H_2	***1:9***	2:9	4:9	6:9

3.3.2 Material Characterization- SEM, Raman spectroscopy and XPS

Sample S_2 looked dark in appearance, similar to S_1 when viewed by the naked eye, while S_3 and S_4 had a more grayish appearance. Electrical measurements showed an increase in the resistance with increase in nitrogen content, ~30-40Ω (S_2), ~10MΩ (S_3) and ~30MΩ (S_4), on the surface at a distance of 20mm between the multimeter probes as compared to <10Ω for S_1. This represents an increase of almost 6 orders of magnitude in the resistance of S_2 and S_3 with respect to S_1 and S_2.

SEM analysis revealed that all three samples had a continuous and uniform growth of nanodiamond films as seen in the first column of figure 3.27. However, at higher magnifications, one can observe difference in the microstructures. There is a transition from 'ridge' or platelet like morphology in S_2 to a more cauliflower like morphology in S_4 with small grain size, evident from the second column of figure 3.27. The microstructure of S_2 is similar to that observed in S_1 with the main difference being in the lengths of the platelets, about 500nm in S_2 versus about 1μm in S_1, and only few nm wide in both cases. Cross sectional SEM images, as seen in the third column of figure 3.27, show the nanodiamond films and the silicon substrates labeled distinctly. The nanodiamond film thickness is about 1.2μm for S_2, same as that observed for S_1. As the nitrogen composition increases, the thickness increased to about 1.3μm for S_3, but further increase in nitrogen reduced the thickness to about 1μm in case of S_4.

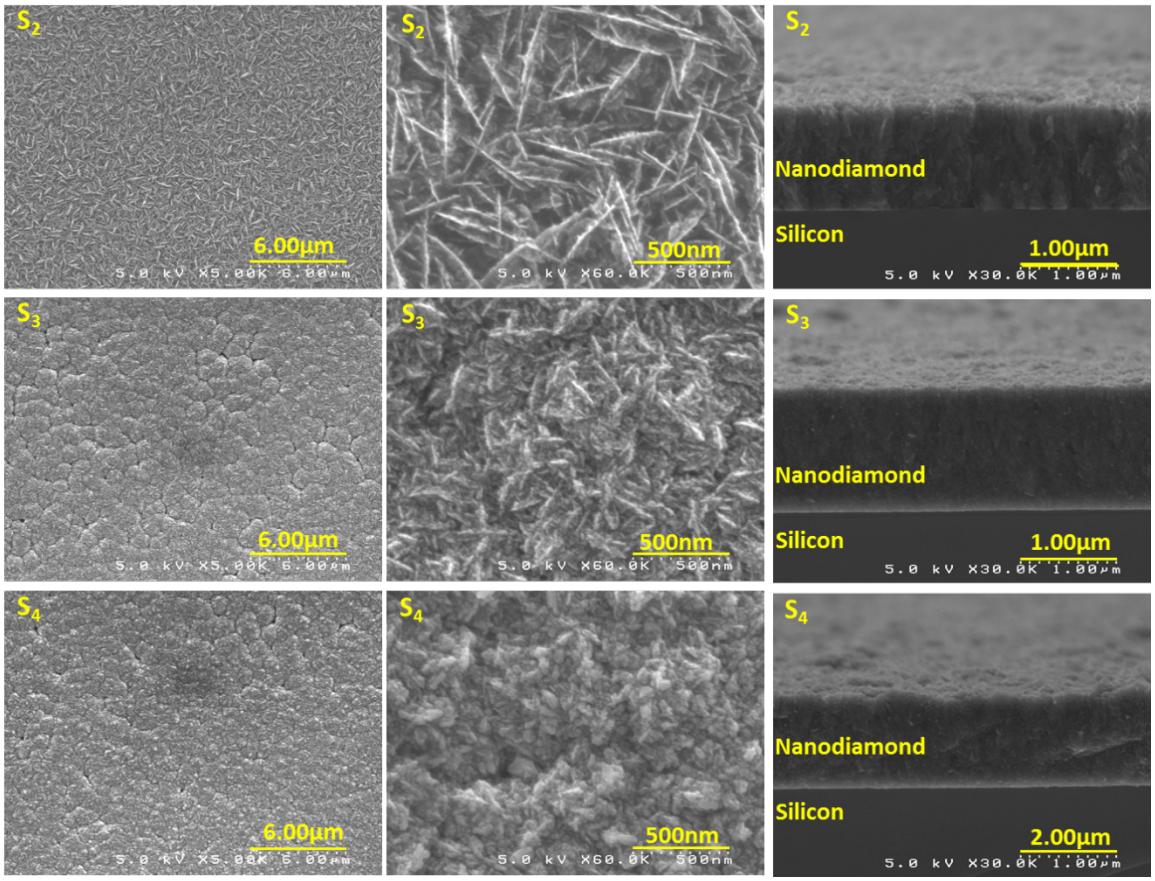

Figure 3. 27 SEM micrographs at low and high resolution for samples S_2 (30sccm), S_3(60sccm) and S_4(90sccm) of uniform and continuous films with the microstructure changing from 'ridge' like (S_2) to 'cauliflower' like (S_4). The third column shows the cross-sectional SEM micrographs of nanodiamond on silicon substrates. The nanodiamond film thickness is about 1.2µm for S_2 which increases to about 1.3µm for S_3 but then decreases to about 1µm for S_4.

Raman spectroscopic analysis was also carried out for the 3 samples with a red laser (632.81nm) as the excitation source. The Raman spectra recorded can be seen in figure 3.28; results for sample S_1 have also been included for comparison.

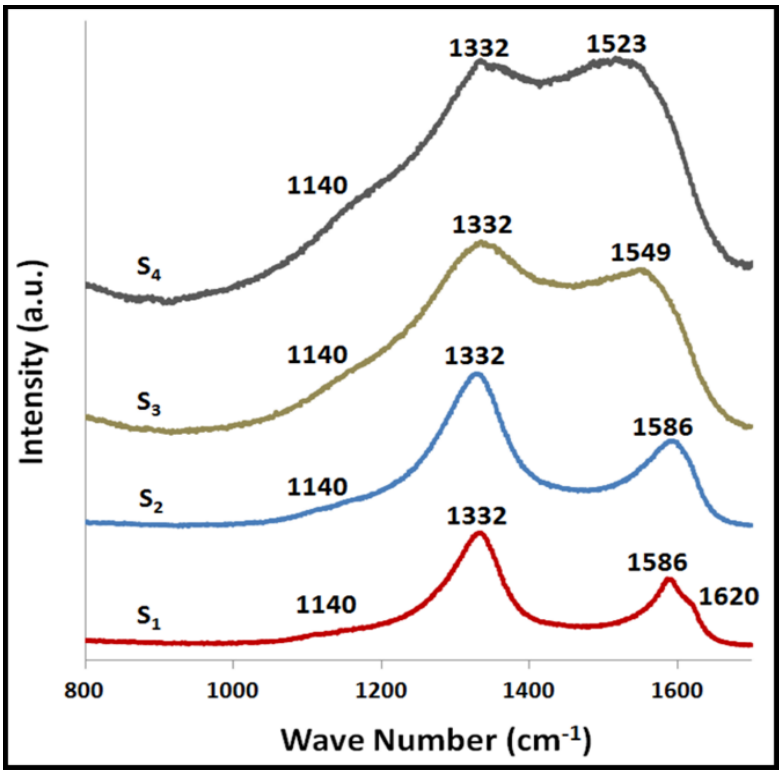

Figure 3. 28 Raman spectra collected for the 4 samples with the diamond peak at 1332 cm^{-1} and graphitic peak at 1523-1586 cm^{-1}. With increase in nitrogen flow, the graphitic peak intensity increases and shifts towards the lower wave numbers. The feature at 1140 cm^{-1} associated with nanodiamond films is present in all samples while the shoulder at 1620 cm^{-1} disappears in S_3 and S_4.

The diamond signature at 1332cm^{-1}, due to sp^3 hybridized C-C bonds, is present for all the nanodiamond films. The G-band, due to the presence of sp^2 hybridized C-C bonds, increases in intensity as the nitrogen composition increases and shifts towards lower wave-numbers; 1586cm^{-1}(S_1 and S_2)→1549cm^{-1}(S_3)→1523cm^{-1}(S_4). An increase in the amorphous carbon content in the nanodiamond films with increase in nitrogen flow can explain the shifting of the G-band [112]. The peaks (diamond and graphitic) become broader and start overlapping. The increase in the peak widths (FWHM) can be attributed to reduction in the grain size and increase in the number of defects (e.g. grain boundaries) and impurities (nitrogen) which is supported by SEM analysis [134]. The relative

intensity of sp^3 C peak to sp^2 C peak decreases from 1.6 for S_1 and S_2 to 1.1 for S_3 to 1.0 for S_4. Increasing nitrogen flow rate lowers the grain size thus increasing the relative amount of grain boundaries where the sp^2 carbon atoms exist [119,134]. The broad feature at around 1140cm^{-1} due to nanocrystalline phase(s) in these films is also present [115]. Another feature observed in case of S_1 and to lesser extent in S_2 at around 1620 cm^{-1} is not present in S_3 and S_4. This feature has been observed in nanocrystalline graphite which suggests the presence of this phase in S_1 and S_2 [112].

XPS data was collected for S_2, S_3 and S_4 to study the composition of these films and then compared the results with that from S_1. The C1s spectra after deconvolution and peak fitting can be seen in figure 3.29 along with the corresponding high resolution micrograph of the nanodiamond films. The peaks at 284.6eV and 285.4eV can be assigned to sp^2 and sp^3 hybridized carbon respectively [119]. The peak at 286.5eV can be attributed to C=O or C≡N bonds but since the peak height increases with increase in nitrogen flow, it is reasonable to assign this contribution to C≡N [120,135-136]. The peak at 287.5eV has been reported to be from graphitic C_3N_4 [120,136]. These results suggest that there was successful incorporation of nitrogen in the nanodiamond films. However, sample survey spectra and N1s deconvolution did not reveal nitrogen presence. This may be due to the fact that the used methane-nitrogen reactant gas mixtures did not yield nitrogen content at or above the detection limits of XPS (8.5×10^{20} cm^{-3}) [137].

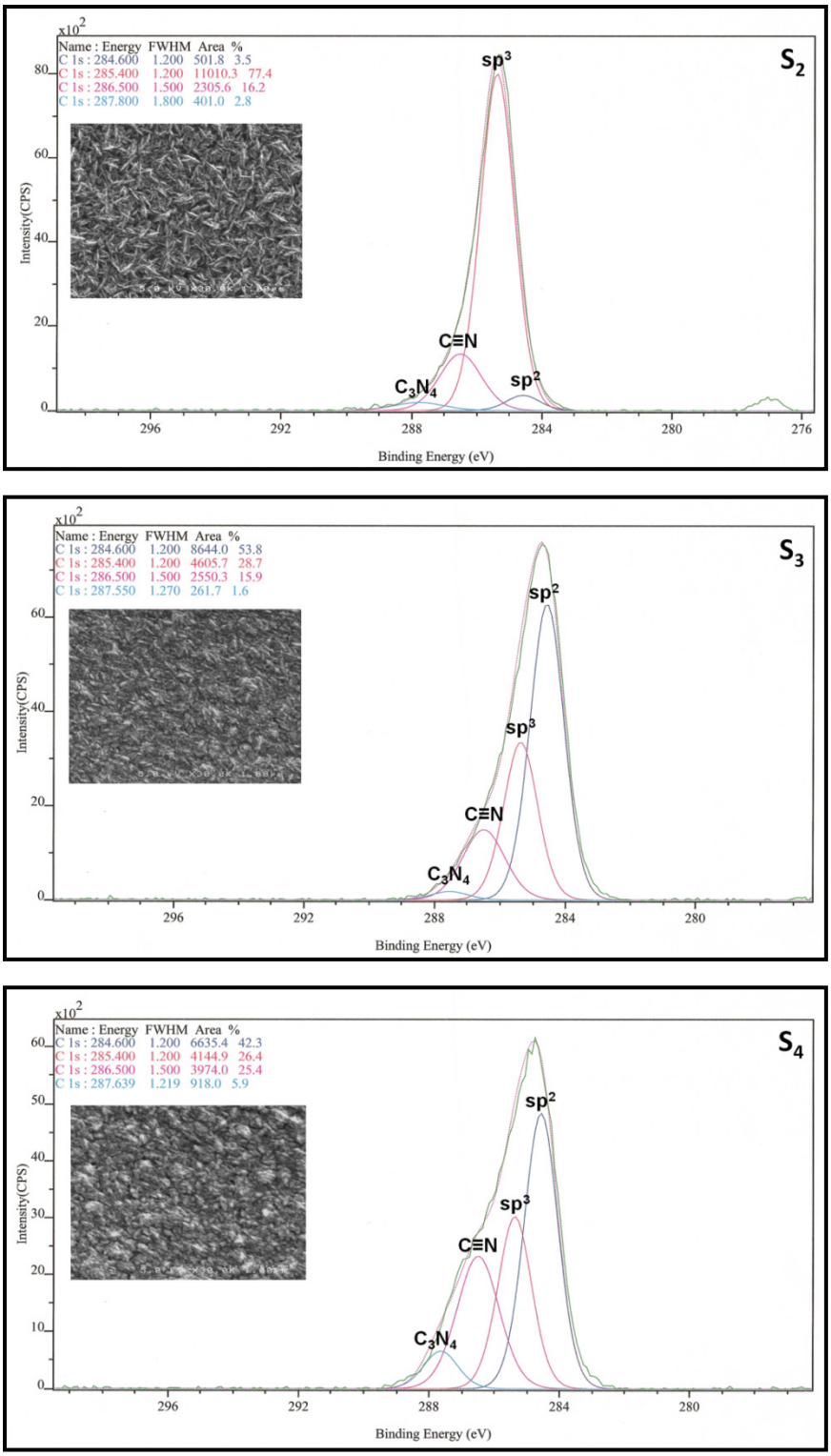

Figure 3. 29 XPS C1s peak after deconvolution, showing a decrease in sp^3 C content and an increase in the sp^2 C and CN bonds with increase in nitrogen flow rates; inset- high resolution SEM micrographs of the nanodiamond films.

In addition to an increase in carbon nitrogen bonding, there is a sharp increase in the sp^2 hybridized C content while the contribution from sp^3 hybridized C decreases as the nitrogen flow rates are increased. Quantitative analysis of contribution from different carbon bonding states is also possible and is depicted in figure 3.30. The sp^3 C/sp^2 C ratio decreases as the nitrogen flow rate is increased, which is consistent with our observations from Raman spectroscopy data. There is a decrease in the electrical conductivity of the S_3 and S_4 because of the larger amount of C≡N and C_3N_4 bonding which increases the band gap of the electrode material [138].

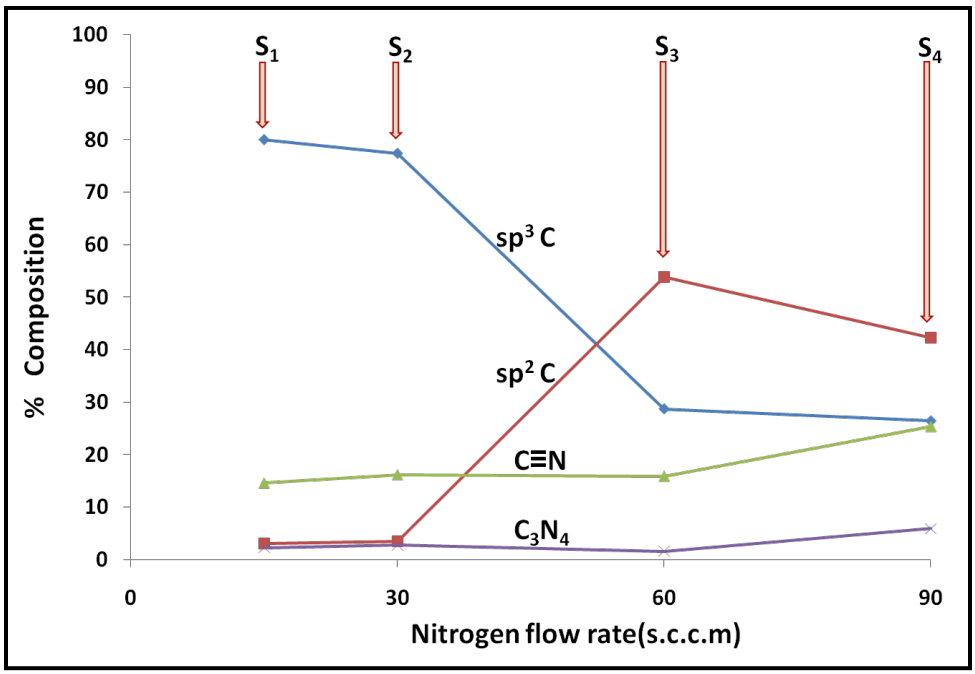

Figure 3. 30 Variation in composition of the different types of carbon bonding states extracted from the C1s XPS data of the nanodiamond films as a function of N_2 flow rates.

3.3.3 Electrochemistry

The electrochemical response of S_2, S_3 and S_4 was examined by using the ferri-ferrocyanide redox couple $\mathbf{Fe(CN)_6^{-3/-4}}$ in 0.1M KCl as the supporting electrolyte, which involves transfer of one electron. The $Fe(CN)_6^{-3/-4}$ redox reaction proceeds through an inner-sphere electron transfer mechanism which involves interaction with the electrode surface and the electrode kinetics are sensitive to the surface chemistry as well as density of electronic states near the formal potential [1].

Background scans in 0.1M KCl at 100mV/s reveal a wide working potential window of about 3V for all the three electrodes, same as that observed for S_1. CVs were also recorded for increasing concentrations of ferrocyanide of 1mM, 2mM, 3.9mM, 5.9mM, 8mM and 10mM at 100mV/s. To compare the electrochemical response of the electrodes, CVs recorded for 10mM ferrocyanide at 100mV/s have been overlapped and presented in figure 3.31. S_2 shows a quasi-reversible response with fast electron transfer kinetics similar to S1. The lowest ΔE_p recorded for S_2 was 80mV which is close to the theoretical value of 59mV for a one electron redox process [5]. In contrast, CVs for S_3 and S_4 show a gradual broadening of the redox peaks, increase in peak-peak separation and a decrease in the signal consistent with sluggish electron transfer kinetics due to poor electrical conductivities and reduced charge carriers at the surface. The peak-peak separations increase with increase in the nitrogen flow rates; $\Delta E_p\,(S_1) = 73mV < \Delta E_p\,(S_2) = 80mV < \Delta E_p\,(S_3) = 180mV < \Delta E_p\,(S_4) = 280mV$.

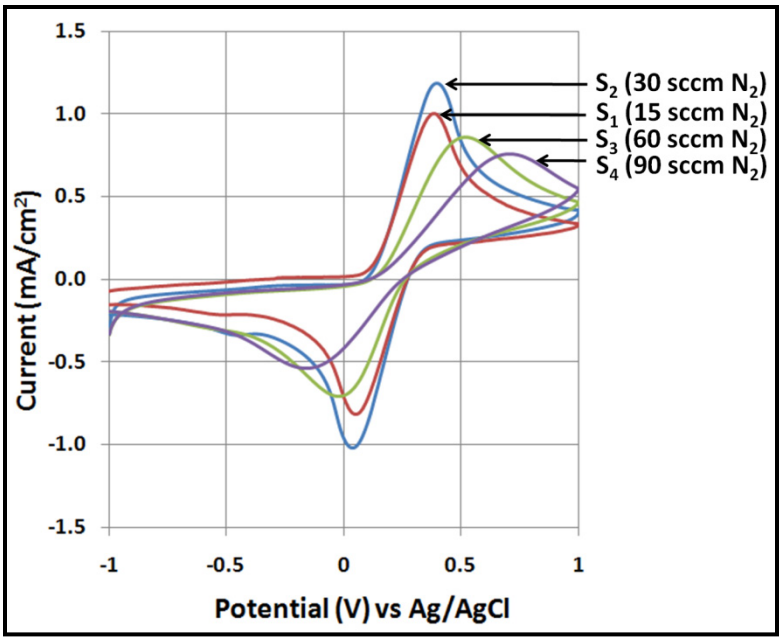

Figure 3. 31 CVs recorded for 10mM ferrocyanide at 100mV/s in 0.1M KCl. $S_1$and S_2 show quasi-reversible response with small ΔE_p values. The redox peaks broaden, the signal is reduced and the value of ΔE_p increases as we go to S_3 and S_4.

One-step chronocoulometry experiments were used to calculate the electroactive areas of each electrode. Compared to an estimated geometric area, as defined by the o-ring, of 0.7 cm^2, the areas calculated decreased; S_1=0.6 cm^2, S_2=0.69 cm^2, S_3= 0.52 cm^2 and S_4=0.45 cm^2. This trend could be due to the variation in the respective surface morphologies/ microstructures and the electroactive sites. The calibration curves, plots of peak oxidation current versus ferrocyanide concentrations, are shown in figure 3.32 to compare the electrode sensitivities. Electrode S_2 shows the highest sensitivity for the $Fe(CN)_6^{-3/-4}$ redox couple.

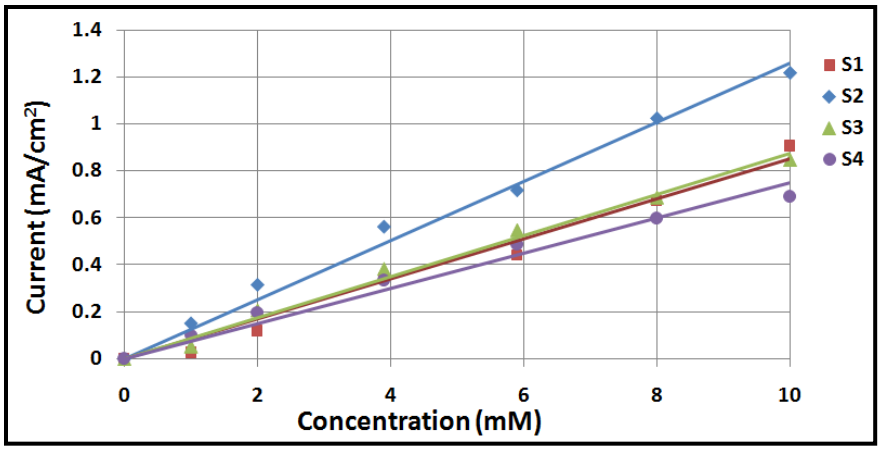

Figure 3. 32 Linear calibration plots derived from the peak oxidation currents (mA/cm^2) and ferrocyanide concentration (mM) for the 4 electrodes showing S_2 with the highest sensitivity for ferrocyanide detection.

CVs for 10mM ferrocyanide in 0.1M KCl were recorded at different scan rates (v) (50mV/s, 100mV/s, 150mV/s, 200mV/s and 250mV/s). The peak oxidation currents varied linearly with the $\sqrt{v}$ which is consistent with semi-infinite linear diffusion or planar diffusion limited mass transport mechanism.

Electrochemical detection of bio-analytes was examined by using **DA** in a PBS solution. The pre-mixed PBS powder makes a solution of pH7.4 which is same as the physiologic pH and was not changed. Background scans at 100mV/s in 0.1M PBS showed wide working potential windows of about 2.8-3.0V. CVs were recorded using S_2, S_3 and S_4 at 100mV/s for increasing concentrations of DA (100µM, 200µM, 400µM, 600µM, 800µM and 1000µM). S_2 showed a quasi-reversible response similar to S_1 with well-defined redox peaks, small peak-peak separation and facile electron transfer kinetics.

Electrode S_2 was able to detect not only the DA/DAQ redox couple, but the LDAC/DAC couple too which are a product of reactions occurring downstream of DA oxidation. In contrast, S_3 and S_4 have a poor response with widely spaced and broad redox peaks with reduced signal. The peak-peak separation (ΔE_p) values of 320mV for S_3 and 430mV for S_4 are much higher than 35mV observed for S_1 and S_2. Slow electrode reaction kinetics in case of S_3 and S_4 are consistent with our previous observations. CVs recorded for 800µM DA in 0.1M PBS at 100mV/s using S_2, S_3 and S_4 can be seen in figure 3.33. The calibration curves were plotted by using the peak oxidation currents for DA (peak 1) versus DA concentration which is shown in figure 3.34. A linear response is obtained for all the electrodes and the sensitivity for DA detection can be calculated from the slope of this curve. The superior sensitivity of S_1 **(0.3µA/cm^2.µM)** and S_2 **(0.4µA/cm^2.µM)** is evident from the plots as compared to S_3 and S_4 **(0.1µA/cm^2.µM)**.

These results suggest that nitrogen incorporation can be achieved by adding nitrogen to the input gas mixture in the MPECVD process. Adding nitrogen leads to an increase in the formation of sp^2 C-C bonds and carbon-nitrogen bonds. However, the electrical conductivity decreases sharply, by almost 6 orders of magnitude, when the N_2 content is$\geq$ 44.4% of H_2 gas. Below this level, the nanodiamond films exhibit quasi-reversible response for bio-analyte detection with rapid electron transfer kinetics.

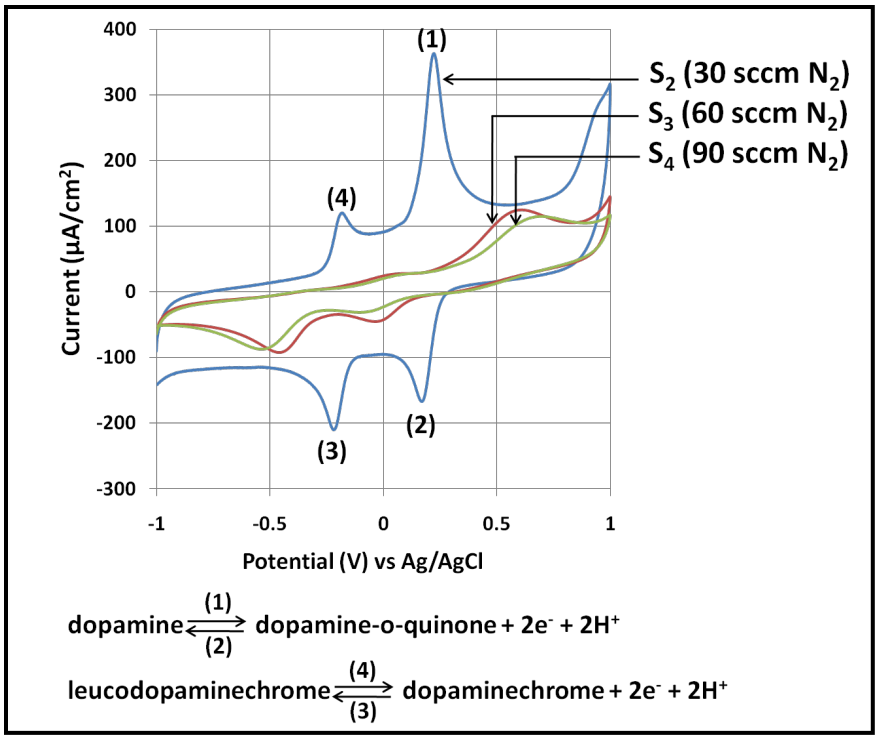

Figure 3. 33 CVs recorded for 800µM DA at 100mV/s in 0.1M PBS. S_2 shows quasi-reversible response with small ΔE_p value. The redox peaks broaden, the signal is reduced and the value of ΔE_p increases as we go to S_3 and S_4. S_2 is able to detect both the DA/DAQ and LDAC/DAC redox couples

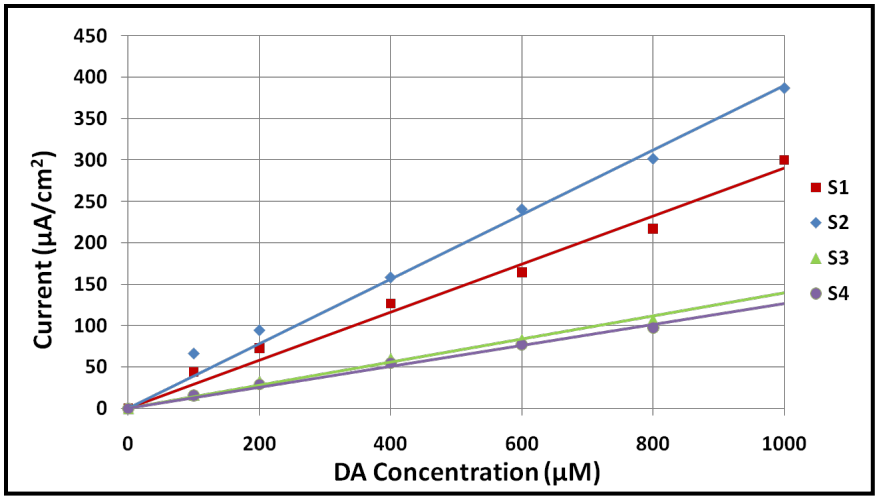

Figure 3. 34 Linear calibration plots plotted between the peak oxidation currents for DA oxidation (peak 1) (µA/cm^2) and DA concentration (µM) for the 4 electrodes. S_1 and S_2 show almost 3x and 4x higher sensitivity as compared to S_3 and S_4.

3.4 Summary

- Nitrogen incorporated nanodiamond macroelectrodes were successfully fabricated on highly doped n-type silicon substrates by MPECVD process.
- The use of high CH_4:H_2 gas ratio (1:4, 1:5, 1:6 and 1:7) along with N_2 yielded substrates with sparse nanodiamond growth which made them unsuitable for use as electrodes.
- Uniform and complete films of nanodiamond were synthesized by reducing CH_4:H_2 ratio to 1:9. An increase in the nitrogen flow rates had a direct impact on the material properties of the nanodiamond, including the microstructure, composition and electrical conductivity.
- The baseline macroelectrode, S_1 (15sccm N_2) and S_2 (30sccm N_2) had almost similar microstructures resembling platelets of nanodiamond, about 1μm long in S_1 and 500nm long in S_2 by few nanometers wide. This changed to a more cauliflower like clusters with small grain size in case of S_3 and S_4, as the nitrogen flow rate was increased.
- Raman spectroscopy revealed peaks which are signatures of sp^3 and sp^2 hybridized C-C bonds. There was an increase in the relative intensity of the G-peak (sp^2 C-C) and a shift towards lower wave numbers due to an increase in the sp^2 C content and possibly the amorphous graphitic content.
- These observations were confirmed by XPS data which showed much higher sp^2/sp^3 C values for S_3 and S_4 as compared to S_1 and S_2. Also, an increase in the carbon-nitrogen bonds was observed with increase in the nitrogen flow rate, which also explained the poor electrical conductivity of S_3 and S_4.

- Electrodes S_1 and S_2 exhibited quasi-reversible response for detection of ferrocyanide in KCl with rapid electrode kinetics. In contrast the S_3 and S_4 response consisted of redox peaks with poor definition and a large peak-peak to separation consistent with sluggish electrode kinetics.
- Similar quasi-reversible response was exhibited for DA detection in 0.1M PBS at pH7.4 by S_1 and S_2 and a linear dynamic range of 100μM-1000μM and sensitivity values of 0.3μA/cm^2.μM and 0.4μA/cm^2.μM respectively.
- Electrode S_1 was also used to successfully detect other interfering bio-analytes such as AA and UA individually. S_1 was able to selectively detect DA in a mixture of 1mM AA and 1mM UA with a sensitivity value of 0.25μA/cm^2.μM with a linear dynamic range of 100μM-1000μM and a limit of detection of 4.41μM.

CHAPTER IV

NANODIAMOND ULTRAMICROELECTRODE ARRAYS

This chapter describes the work done to fabricate and characterize nitrogen incorporated nanodiamond ultramicroelectrode arrays. The first design consisted of UMEAs, with pyramidal geometry, fabricated from highly doped n-type silicon substrate after a combination of thermal oxidation (0.5µm), conventional UV photolithography and isotropic silicon etch. In the first approach, the silicon substrate with array of tips was thermally oxidized (0.5µm) followed by a partial SiO_2 etch-back to produce pyramids with silicon exposed near the top. Nanodiamond was selectively grown on the exposed silicon regions of the tips. In the second approach under this design, nanodiamond was grown on the silicon substrate (with tips) followed by e-beam deposition of 0.2µm quartz and a partial quartz etch-back to expose the top section of the pyramids. Nanodiamond UMEAs were successfully fabricated by these techniques, however their electroanalytical performance was poor in addition to other drawbacks.

Planar nanodiamond UMEAs were then fabricated on highly doped n-type silicon substrates where the UMEs projected above the surround SiO_2 insulating layer, thus providing a 3-D electroactive surface. The microstructure consisted of platelets of nanodiamond, 100-200nm long and few nanometers wide. These UMEAs exhibited quasi-reversible response for the ferri-ferrocyanide redox couple. Also, they detected bio-analytes such as DA, AA and UA successfully.

4.1 Pyramidal ultramicroelectrode arrays

Ultramicroelectrode arrays combine the size advantages with current enhancement from an array. By using UMEAs, we can achieve high rates of mass transport of the analyte to the UMEA surface, improve S/N ratio due to low capacitance, reduce iR_u losses due to uncompensated resistance and perform experiments with high temporal resolution [6-8].

The motivation behind choosing the pyramidal shape is to provide a true three-dimensional electroactive surface where hemi-spherical diffusion limited mass transport is dominant and reduce the edge effects observed in two-dimensional, disc shaped geometry. To achieve this configuration, conventional silicon microfabrication technology with MPECVD diamond growth process was used. Two approaches, bottom-up and top-down were identified to produce the final UMEA structures.

There were some common steps in the beginning of these processes. We start with a highly doped n-type silicon substrate which was thermally oxidized for 45 minutes at 1100°C with oxygen flow rate at 20 sccm. This produced a 0.5μm thick SiO_2 layer. By using conventional UV photolithography we patterned and developed a square array consisting of 10^6 square pads each with 10μm edge and 30μm pitch, protected by the photo-resist on top. The exposed SiO_2 was wet-etched by using buffered oxide etch (BOE) for 5 minutes followed by stripping of the photoresist. Then an isotropic etch was performed by using a 1:20 mixture of HF and HNO_3 which etches the silicon around and under the SiO_2 pads which act as the mask, thus creating a pyramidal structure. Figure 4.1 (a) shows the UMEA before completion of the acid etch, where the SiO_2 pad/mask is still

present at the top. The final structure consisting of silicon tips and a single silicon tip can be seen in figures 4.1 (b) and 4.1 (c) respectively.

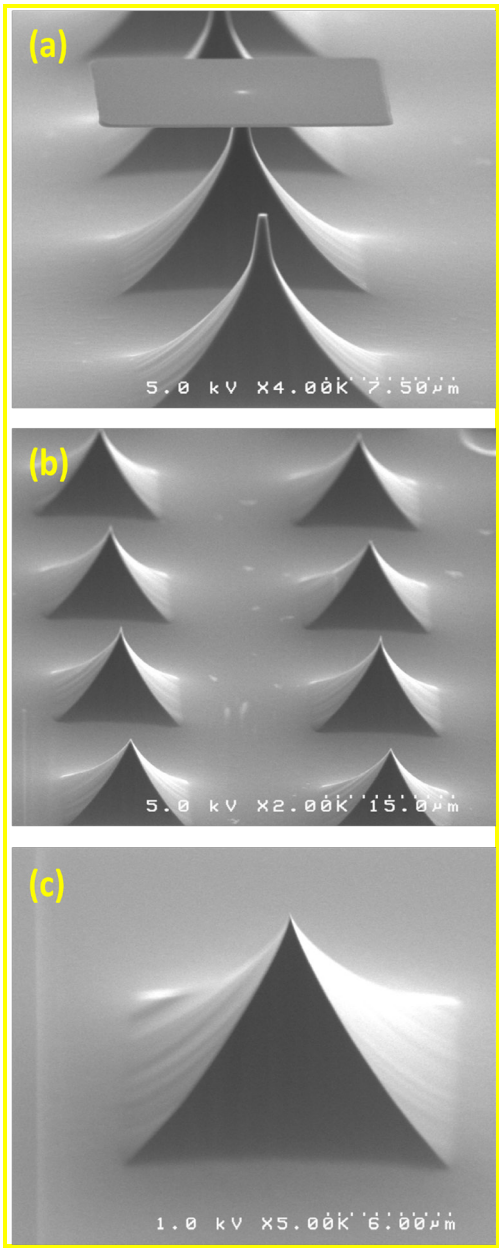

Figure 4. 1 (a) Silicon tip with the SiO_2 pad on top, just before completion of the isotropic acid etch. (b) Final array of silicon tips. (c) Individual silicon tip in the array.

Bottom-up fabrication: After fabricating silicon pyramidal array, the entire substrate, including the tips, was thermally oxidized. We then spin coated and hard baked a layer of photo-resist (AZ5214E) at 5000 rpm and 135°C (2 minutes), respectively. Due to the centrifugal force, the photo-resist flows away from the tips. A wet etch in BOE removed the exposed SiO_2 thus revealing the silicon underneath as seen in figures 4.2 (a) and (b). Before stripping the photo-resist, the UMEA underwent an ultrasonic surface preparation step in a nanodiamond powder and de-ionized water slurry for 5 minutes. MPECVD process was then used to selectively grow nanodiamond on the silicon tips. The schematic diagram of the fabrication process has been included in appendix B, figure B.1.

The parameters used were: Power = 550W, Pressure = 13 torr, Substrate temperature = 850^{o}C, Gas flow rates ($H_2/CH_4/N_2$) = 135/15/15 sccm and Time = 30 minutes. The exposed SiO_2 layer is susceptible to damage from the harsh plasma conditions which limited the power and growth time that could be used. The nanodiamond grew selectively and uniformly on the silicon tips, as seen in figures 4.2 (c) and (d) while the SiO_2 layer acts an insulator between the individual UMEs.

However, this process had a few draw backs. In some trials, nanodiamond grew in form of a ball just at the tip of the pyramid as seen in figure 4.2 (e). The high aspect ratios of the tips create a field enhancement effect because of which the nanodiamond growth is accelerated in a much localized area. In other cases, there was nanodiamond growth on the SiO_2 region of the pyramid instead of the silicon, as seen in figure 4.2 (f). The pyramidal geometry of the UMEA cannot be avoided. Also, the duration of surface pre-

treatment is limited by the amount of time the photo-resist can withstand the ultrasonication process, which is less than 5 minutes.

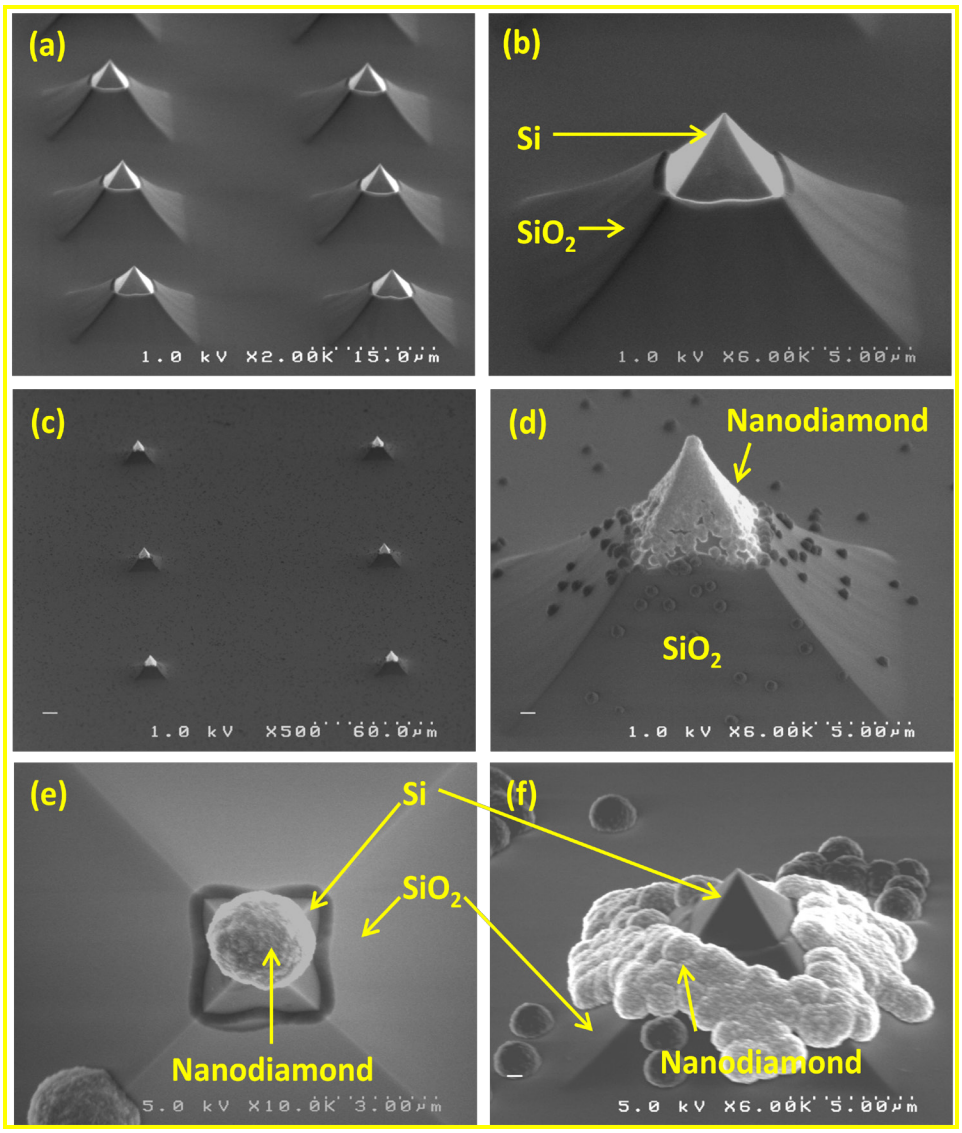

Figure 4. 2 (a) and (b) Exposed silicon at the tip after SiO_2 back-etch; (c) and (d) Controlled and selective growth of nanodiamond on the exposed silicon tips to achieve the final structure; (e) MPECVD trial resulting in very localized nanodiamond growth in a ball-form at the apex; (f) MPECVD trial resulting in nanodiamond growth on the SiO_2 instead of the silicon tips.

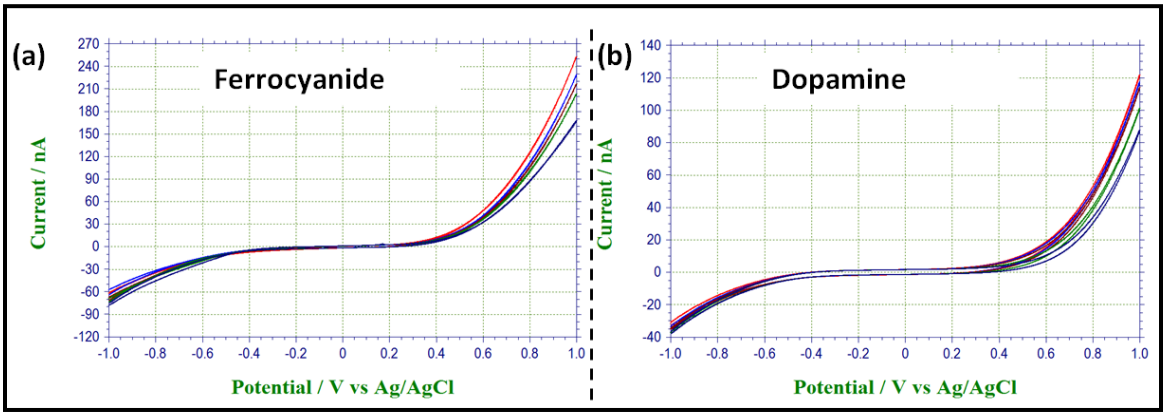

Figure 4. 3 (a) CVs recorded at 100mV/s in 0.1M KCl for different ferrocyanide concentrations; 0.5mM (Dark Blue), 1mM (Green), 2mM (Brown), 3.9mM (Blue) and 5.9mM (Red). (b) CVs recorded at 100mV/s in 0.1M PBS for different DA concentrations; 200µM (Dark Blue), 400µM (Green), 600µM (Brown), 800µM (Blue) and 1000µM (Red).

Electrochemistry: The CVs recorded for the $Fe(CN)_6^{-3/-4}$ redox couple did not yield any identifiable signal, neither a peak-shaped nor a sigmoidal response, as seen in figure 4.3(a). Different concentrations of ferrocyanide, 0.5mM, 1mM, 2mM, 3.9mM and 5.9mM, and a scan rate of 100mV/s were used to generate these curves. This can be attributed to poor electrical conductivity of the nanodiamond grown under the given conditions. Similar behavior was observed for DA detection. CVs recorded for different DA concentrations (200µM, 400µM, 600µM, 800µM, 1000µM) at 100mV/s in 0.1M PBS solution can be seen in figure 4.3(b).

Top-down fabrication: In the second approach, a conformal layer of nanodiamond was grown on the bare silicon pyramidal array by MPECVD process while maintaining the sharp tip geometry, as seen in figure 4.4(a) and (b). Sample surface

preparation before the MPECVD process involved ultrasonication in a nanodiamond powder slurry in de-ionized water for 10 minutes.

The MPECVD parameters used were: Power = 550W, Pressure = 13 torr, Substrate temperature = 850°C, Gas flow rates ($H_2/CH_4/N_2$) = 135/15/15 sccm and Time = 1 hour. To provide insulation, a 0.2µm thick layer of quartz was deposited by e-beam evaporation. This was followed by spin-coating and hard baking a layer of photo-resist, AZ5214E at 5000 rpm which acts as a sacrificial mask during the quartz etch back step in BOE. The final step was stripping of the photo-resist. The UMEA consists of exposed nanodiamond/silicon tips isolated from each other by a layer of quartz, as seen in figure 4.4(c) and (d). The schematic diagram of the fabrication process has been included in appendix B, figure B.2.

Electrochemistry: Electrochemical analysis using the $\mathbf{Fe(CN)_6^{-3/-4}}$ redox couple showed a peak-shaped response with large ΔE_p values and sluggish electrode reaction kinetics. CVs recorded for different ferrocyanide concentrations (1mM, 2mM, 3.9mM, 5.9mM and 8mM) in 0.1M KCl at 100mV/s scan rate can be seen in figure 4.5(a). The peak-shaped response is observed because at the scan rates used, the individual diffusion layers of each UME overlap each other due to the small spacing between the UMEs. The response is similar to that observed for a macro-electrode of an electroactive area equal to the sum of the UMEs and with semi-infinite linear or planar diffusion dominated mass transport mechanism [6]. The nanodiamond film grown may still not be conductive enough to support rapid electron transfer as inferred from the large peak-peak separation. A linear calibration plot can be seen in figure 4.5(b).

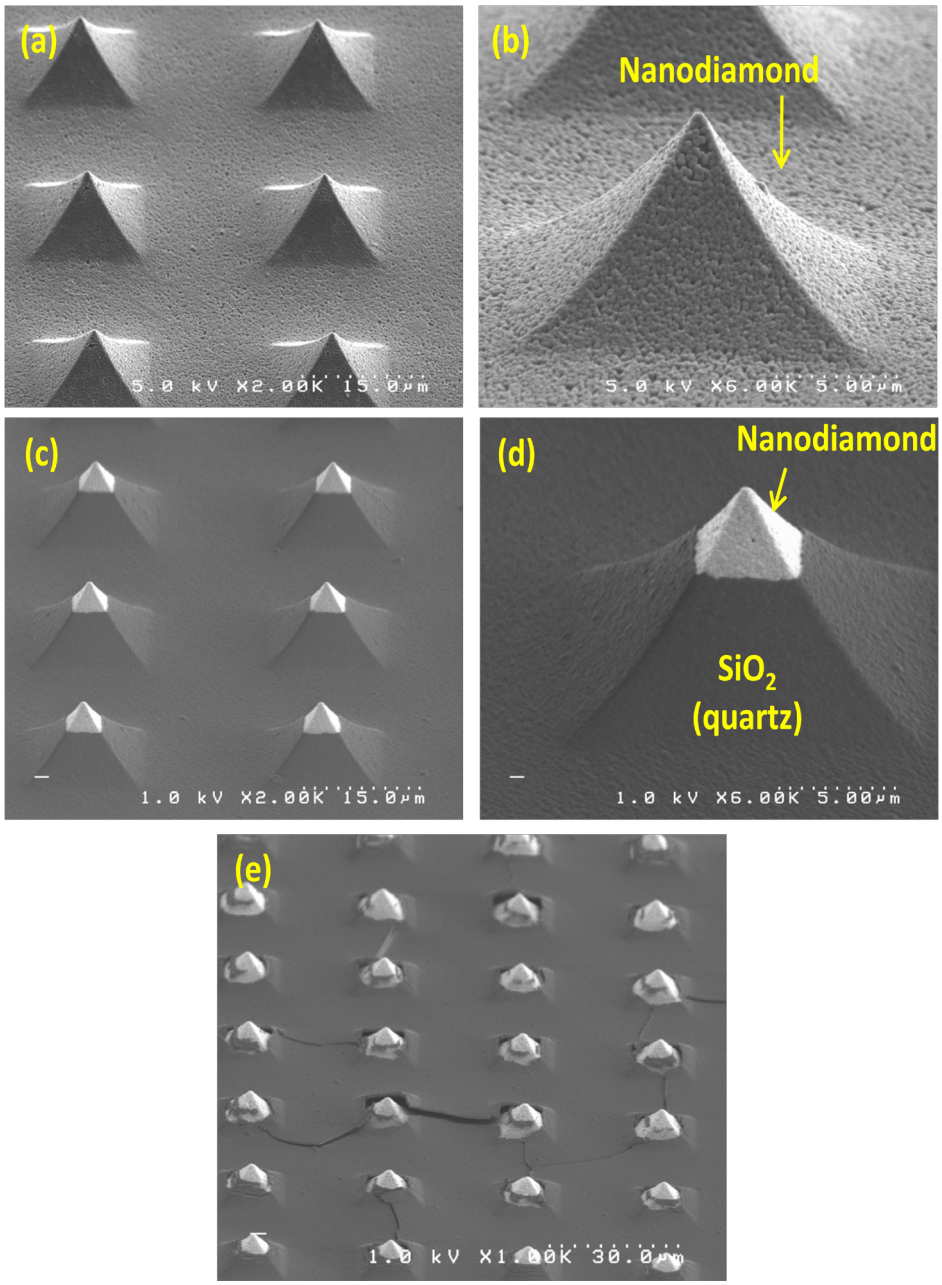

Figure 4. 4 (a) and (b) Conformal growth of nanodiamond film on the bare silicon pyramidal array; (c) and (d) The final structure of the UMEA, nanodiamond/silicon tips isolated from each other by a layer of quartz; (e) The UMEA seen after the de-lamination of the quartz layer due to poor adhesion.

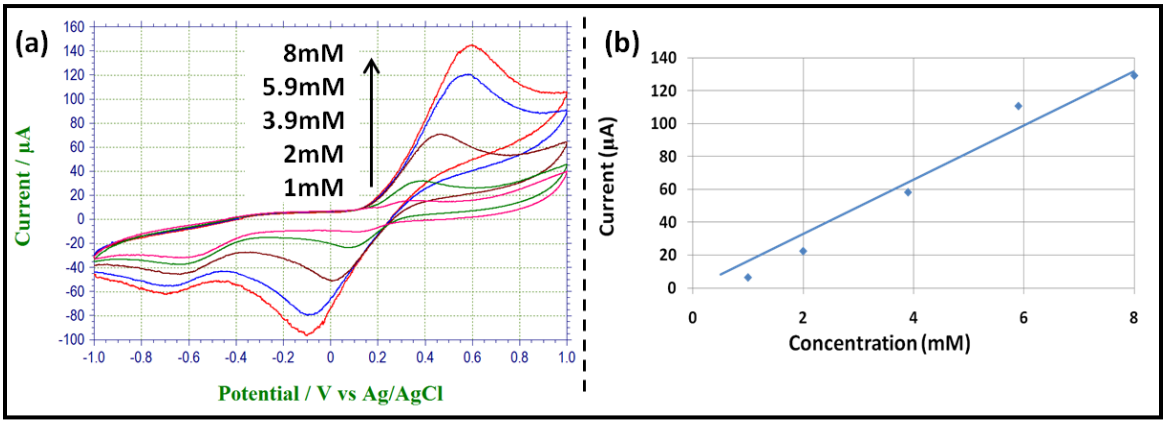

Figure 4. 5 (a) CVs recorded at 100mV/s in 0.1M KCl for different ferrocyanide concentrations. (b) Calibration curve plotted using the peak oxidation currents (µA) vs. ferrocyanide concentrations (mM), showing a linear relationship.

The quality of the nanodiamond film could be improved to get a better electrochemical response; however, there existed another critical problem. During the electrochemical experiments, the response would slowly start increasing with time which was not proportional to the increase in the ferrocyanide concentration. SEM analysis revealed that there was poor adhesion between the insulating quartz and the nanodiamond/Si layers which resulted in the delamination of the quartz layer, as seen in figure 4.4(e). To overcome this problem, the UMEA was annealed at 800°C for 1 hour and 2 hours (in two separate trials) in an inert atmosphere after quartz deposition. This intermediate step improved the adhesion and prolonged the life of the device, however, the experiments always ended in catastrophic failure due to delamination of quartz.

The limitations of the two approaches of UMEA fabrication discussed previously include;

1. Localized nanodiamond growth just at the apex of the pyramids or on oxide layer.
2. Poor electrical conductivity of the nanodiamond layer.
3. Poor adhesion between the quartz and nanodiamond layers.

In addition to these, the final devices were fragile and susceptible to mechanical damage (breaking of tips) and led us to change the design and modify the fabrication process to produce a better and durable UMEA.

4.2 Planar ultramicroelectrode arrays

4.2.1 Fabrication and material characterization

The planar nanodiamond UMEAs were designed with sufficient spacing between the UMEs in order to avoid the overlapping of individual diffusion layers. The UMEAs had to be used under steady state conditions where the mass transport is dominated by radial diffusion process, as seen in figure 2.4 (b).

Bottom-up fabrication: A 0.5μm thick SiO_2 layer was grown by thermal oxidation at 1100^{o}C on a highly doped n-type silicon substrate, 15mm x 15mm in size. This was followed by deposition of a 0.5μm thick layer of molybdenum by DC sputtering technique in a Cressington 308R coating system at 80mA deposition current, the thickness was monitored by the built-in quartz crystal microbalance. Then, AZ5214E photoresist was spin-coated on the top surface. Conventional UV photolithography was used to expose and develop the layout of the UMEAs. The regions not covered by the

photoresist were etched in 2 steps. In the first step, molybdenum film was wet-etched followed by wet-etch of the exposed SiO_2 layer by BOE (buffered oxide etch). This also etched SiO_2 on the back side of the substrate. The wet-etch processes created trenches exposing the silicon surface.

Surface preparation was performed by ultrasonication in slurry of nanodiamond powder and de-ionized water for 5 minutes followed by photo-resist stripping and a thorough rinse with acetone, isopropyl alcohol (IPA) and de-ionized water. Nanodiamond was grown in the Astex MPECVD machine and the following parameters: Power = 1000W, Pressure = 25 torr, Substrate temperature = 850^{o}C, Gas flow rates ($H_2/CH_4/N_2$) = 135/15/15 sccm and Time = 2-2:30 hours. The molybdenum film acted as a sacrificial layer to protect the under lying SiO_2 from plasma damage during the MPECVD process. The final step consisted of molybdenum lift-off by wet-etch process. The fabrication process flow can be seen in figure 4.6(a).

The end-result of this fabrication process was an array of nanodiamond ultramicroelectrodes in a SiO_2 matrix projecting above the surrounding plane, as seen in figure 4.6(b). The UMEAs provide a 3-D surface, although not of a regular shape, during electroanalytical experiments. Based on this fabrication process, three nanodiamond UMEAs were produced and labeled as $UMEA_1$ (50x50), $UMEA_2$ (20x20) and $UMEA_3$ (10x10). These dimensions are based on information obtained from SEM analysis. Figure 4.7 shows the SEM micrographs of the 3 UMEAs.

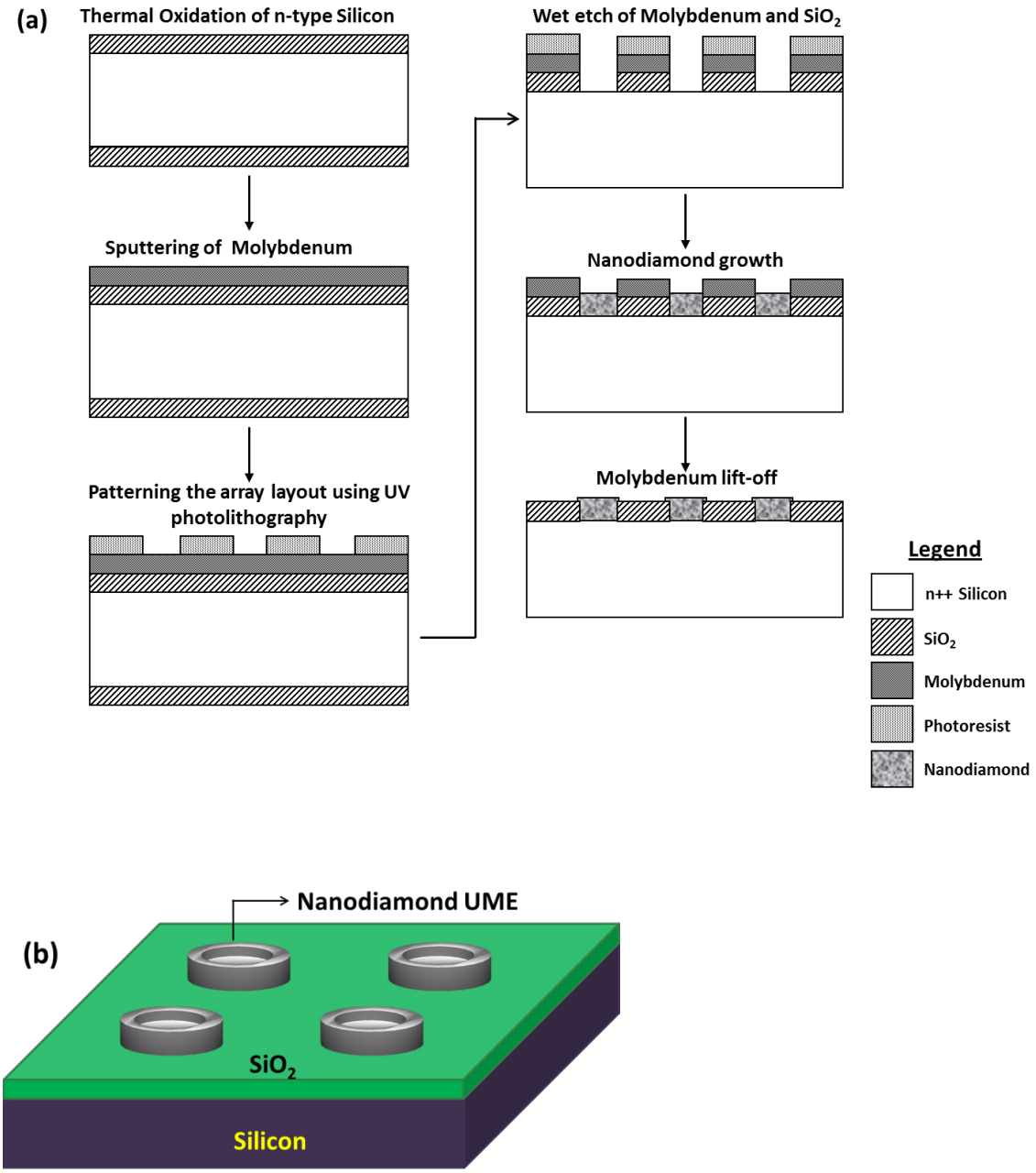

Figure 4. 6 (a) Schematic diagram of the fabrication process for the planar nanodiamond UMEAs. (b) A 3-dimensional representation of the final UMEA structure.

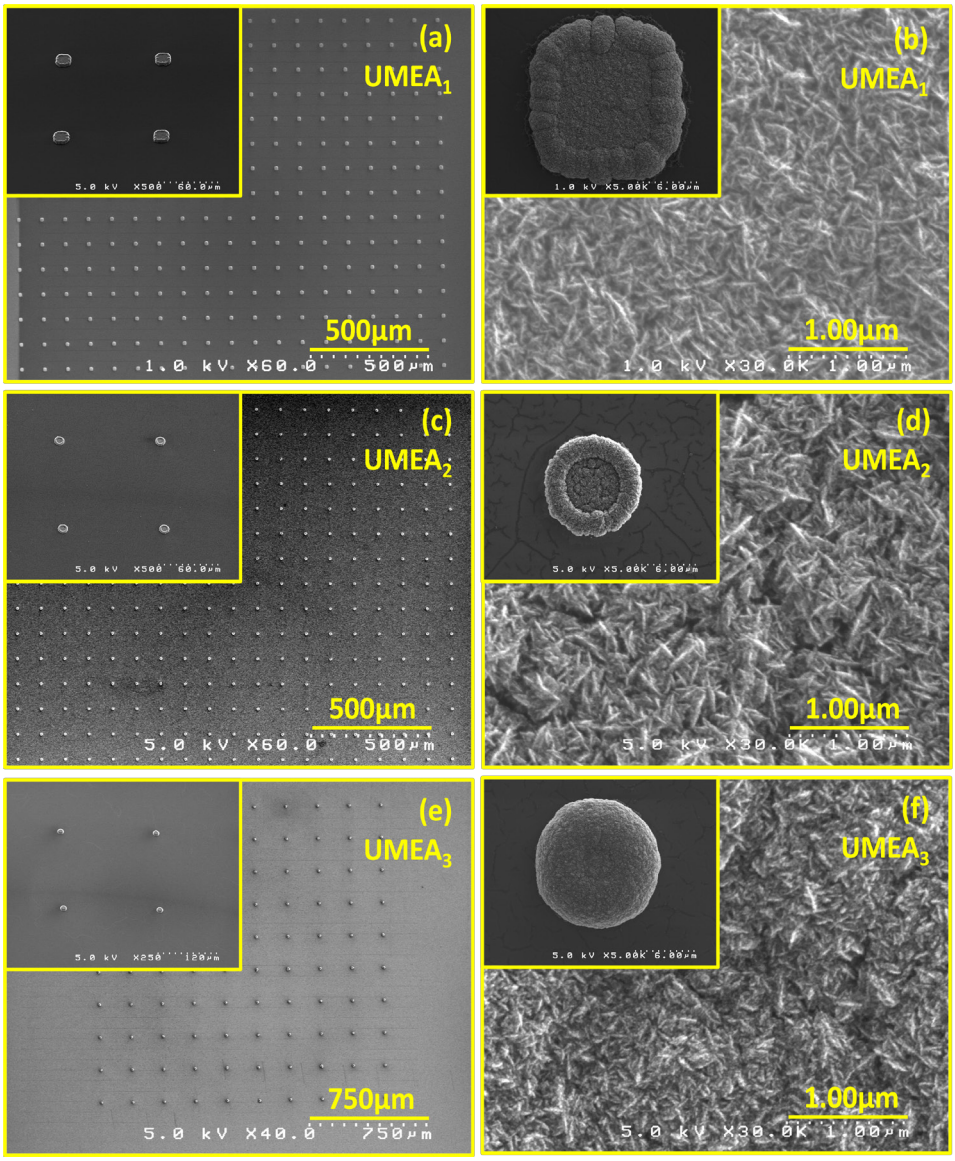

Figure 4. 7 (a) (c) (e) Low magnification SEM image of the array layout for $UMEA_1$, $UMEA_2$ and $UMEA_3$ respectively; inset- 4 UMEs viewed at a 45^o tilt showing that they project above the surround SiO_2 plane. (b) (d) (f) High resolution SEM images of the 'ridge' like microstructure of the nanodiamond $UMEA_1$, $UMEA_2$ and $UMEA_3$ respectively.; inset- SEM images of individual UMEs showing a 'donut' shaped profile, thicker at the periphery than in the center.

The low magnification SEM micrographs in the left column show the layout of the arrays and inset are images recorded of four UMEs at an angle of 45^{o}. High resolution SEM images in the right column the corresponding microstructures of each UMEA and inset are images of individual UMEs. In figure 4.7(a), (c) and (e), the UMEs can be easily identified by the bright spots surrounded by the SiO_2 insulation. All the devices have similar nanodiamond microstructure consisting of 100-200nm long 'ridge' or platelet like features, as seen in figure 4.7(b), (d) and (f). The wet-etch process of molybdenum and SiO_2 created a rough surface at the periphery of the UMEs which led to higher nanodiamond growth rates there than in the middle. This resulted in the 'donut' form of the UMEs seen in the inset of figure 4.7(b), (d) and (f).

$UMEA_1$ has 2500 elements arranged in a square layout with a spacing (pitch) of 100μm between neighboring UMEs. The overall shape of the UMEs is square with an edge length of about 15μm. $UMEA_2$ consists of 400 elements also arranged in a square layout with a spacing of 100μm. Each UME has a circular shape and radius of about 5μm. $UMEA_3$ is a square array of 100 elements but with a larger spacing of 200μm. Each UME has a radius of about 7.5μm.

4.2.2 Electrochemistry

Under steady state conditions we get a sigmoidal shaped response due to hemispherical diffusion limited mass transport of the analyte to the UME surface [6]. Based on the 3-D geometry of the nanodiamond UMEAs, they can be considered to be hemispheres with an equivalent radius r_{eq}. The current-time relationship for spherical or hemispherical UMEs can be given by equation 4.1 [6].

$$\boldsymbol{i = \frac{nFAD_o^{\frac{1}{2}}C_o^*}{\pi^{1/2}t^{1/2}} + \frac{nFAD_oC_o^*}{r_o}} \qquad \mathbf{4.1}$$

where: i= current, n= number of electrons transferred, F= Faraday's constant (96500 C/mol), A= electroactive area (cm^2), D_o= diffusion coefficient of the oxidized species (cm^2/s), C_o^* = bulk concentration of the oxidized species (mol/cm^3) and r_o= radius of the hemisphere or sphere. The first term in equation 4.1 dominates at short times (or fast scan rates) when the diffusion layer thickness is less than r_o. Semi-infinite linear diffusion is dominant in this time regime. The second term is dominant under steady state conditions at longer times (or slower scan rates). The diffusion layer thickness becomes larger than the UME dimensions.

The nanodiamond UMEAs were used under steady state conditions where the steady state or limiting currents for N UMEs each of an equivalent radius r_{eq} is given by equation 4.2.

$$\boldsymbol{i = 2\pi NnFD_0C_o^*r_{eq}} \qquad \mathbf{4.2}$$

Initial characterization of the nanodiamond UMEAs was performed by using the ferri-ferrocyanide redox couple $\mathbf{Fe(CN)_6^{-3/-4}}$ in 0.1M KCl as the supporting electrolyte. This redox reaction is accompanied with the transfer of one e^-; ferrocyanide is oxidized to form ferricyanide, as depicted by the following reaction:

$$Fe(CN)_6^{4-} \quad \leftrightarrows \quad Fe(CN)_6^{3-} + e^-$$

$$ferrocyanide \qquad ferricyanide$$

CVs recorded at 100mV/s by using the nanodiamond UMEAs as the working electrodes can be seen in figures 4.8(a), (b) and (c). Under these conditions sigmoidal response was observed for the three devices, consistent with hemi-spherical diffusion limited mass transport. The individual diffusion layers did not overlap, thus preserving the UMEA response.

The limiting currents increased with increase in the ferrocyanide concentration. In addition to this, the faradaic currents decreased as the electroactive areas decreased, $UMEA_1 > UMEA_2 > UMEA_3$. Closer analysis of the curves using the Tomeš criterion, $(E_{3/4} - E_{1/4})$, which is the difference between the three-quarter wave potential and quarter wave potential, was found to be between 56 and (56/α) mV suggesting quasi-reversible electrode kinetics [6]. For the ferri/ferrocyanide redox couple, the value of $\alpha = 0.5$.

The half wave potential, $E_{1/2}$, for a steady state CV is equal to the formal potential, $E^{o\prime}$, of the cell in a perfectly reversible system [6]. The $E_{1/2}$ values increase as the array size decreases, $E_{1/2}$ ($UMEA_1$) = 0.18V → $E_{1/2}$ ($UMEA_2$) = 0.22V → $E_{1/2}$ ($UMEA_3$) = 0.24V. This trend suggests that there is an increasing deviation from a perfectly reversible response or in other words, more sluggish reaction kinetics [6].

Calibration curves were plotted for each UMEA between the steady state limiting current (mA/cm^2) and the ferrocyanide concentration (mM) which gave a linear relationship, as seen in figure 4.9. The slopes of these calibration plots were used in conjunction with equation 4.2 to calculate the equivalent radii of individual UMEs, assuming their shape to be perfectly hemi-spherical. The details of the UMEAs' dimensions can be seen in table 4.1.

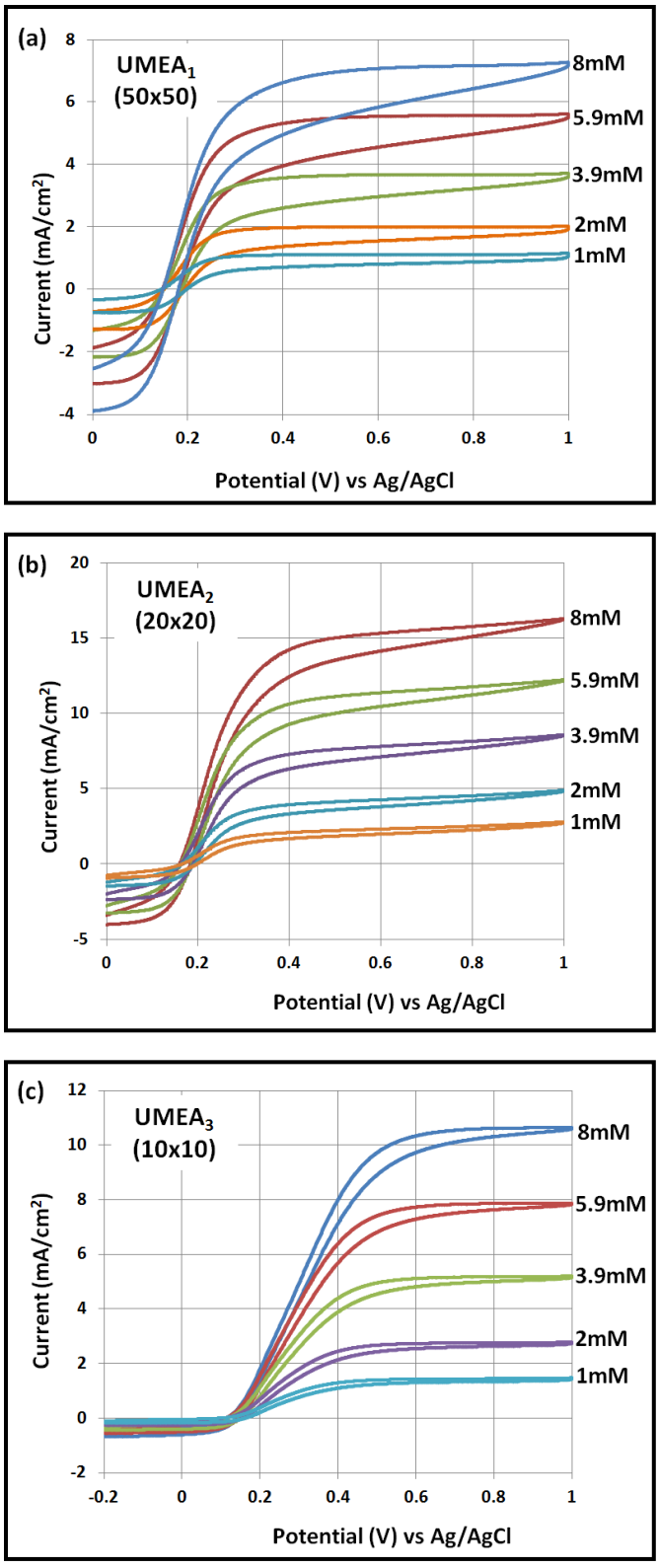

Figure 4. 8 CVs recorded in 0.1M KCl at 100mV/s for increasing concentrations of ferrocyanide by using the nanodiamond UMEAs; (a) $UMEA_1$- 50x50 array, (b) $UMEA_2$- 20x20 array and (c) $UMEA_3$- 10x10 array.

Table 4. 1 Nanodiamond UMEAs' dimensions.

	$UMEA_1$ (50x50)	**$UMEA_2$ (20x20)**	**$UMEA_3$ (10x10)**
Total number of UMEs (N)	2500	400	100
Size of each UME (µM)	15 (edge length)	5 (radius)	7.5 (radius)
Spacing (d) (µm)	100	100	200
Electroactive Area (geometric) (cm^2)	$5.625x10^{-3}$	$3.14x10^{-4}$	$1.766x10^{-4}$
Total Array Area ($N.d^2$) (cm^2)	0.25	0.04	0.04
Equivalent UME radius (r_{eq}) (µm)	***6.4***	***3.7***	***5.6***
Equivalent Area ($N.2\pi r_{eq}^2$) (cm^2)	*$6.441x10^{-3}$*	*$3.423x10^{-4}$*	*$1.966x10^{-4}$*

The equivalent radii provide a better way to compare electrochemical response between the three UMEAs as it compensates for differences in shape and size. The calibration plots normalized to the equivalent areas of each UMEA can be seen in figure 4.9. In order to highlight the advantages of UMEs, the calibration plot for the macro-electrode S_1 has also been included.

All three UMEAs have a much higher sensitivity for ferrocyanide detection as compared to the macroelectrode because of the high analyte flux densities achieved due to the small dimensions. The macroelectrode has a sensitivity of **85.2µA/cm^2 per mM** of ferrocyanide. In comparison, the value for $UMEA_1$ is ***13x***, $UMEA_2$ is ***23x*** and $UMEA_3$ is ***15x*** higher. The improvement in performance of the UMEAs is consistent with the decrease in the size or r_{eq}, which has an inverse relationship with the current density. $UMEA_2$ has the smallest dimension and its sensitivity is ***1.7x*** $UMEA_1$ and ***1.5x*** $UMEA_3$.

The effect of UME size is evident, however, no information could be obtained about the effect of inter electrode spacing. Theoretically, when $d=2r_{eq}$, the UMEA response is similar to a macroelectrode of same area because the individual diffusion layers completely overlap and produce peak-shaped CVs [63,139-140]. Only when $d >> 2r_{eq}$, do we observed a characteristic, steady state UMEA response where the total current from each UME is amplified N times (N= total number of UMEs) [63, 139-140]. It has been reported that the inter-electrode spacing should be at least 10 times the UME diameter to avoid an overlap of individual diffusion layers; of course, the scan rate is also an important consideration [63,141].

The current density from an UMEA is smaller than that obtained from a macroelectrode when one considers the size of the entire array, including the insulated regions in between. Thus, the design of the UMEA has to be optimized in order to maximize its efficiency while maintaining a small footprint for the entire array. This effect can be seen in figure 4.10 where current efficiencies, with respect to a macro electrode, for $UMEA_1$ is highest followed by $UMEA_2$ and $UMEA_3$.

CVs at increasing scan rates (100mV/s, 200mV/s, 300mV/s, 400mV/s and 500mV/s) and 8mM ferrocyanide concentration were recorded for $UMEA_3$ to study the effect on its response, as seen in figure 4.11. Under steady state conditions, the signal should be independent of the scan rate [70]. However, despite having a sigmoidal response, there is a very small increase in the current with increase in the scan rate as seen by the shallow slope of the plot in the inset of figure 4.11. This could be due to the fact that as the scan rate is increased, the diffusion layer thickness decreases and the

contribution of current due to semi-infinite diffusion increases, corresponding to the first term in equation 4.1 [70,142].

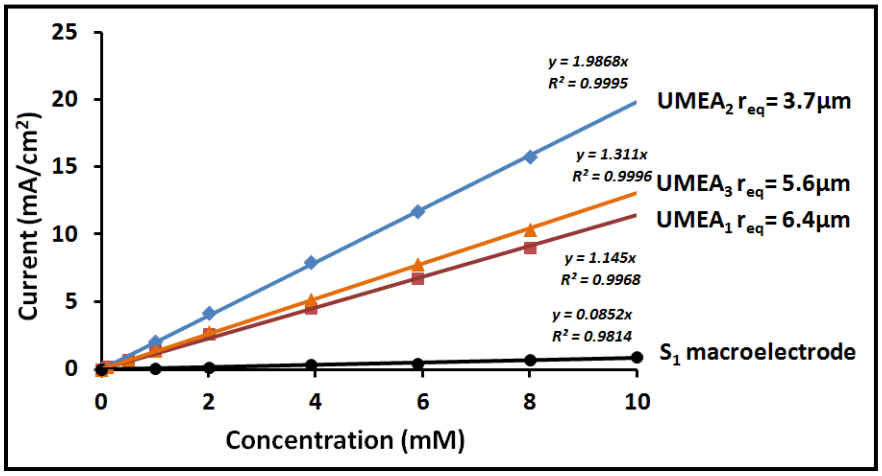

Figure 4. 9 Linear calibration curves plotted between the steady state currents and the ferrocyanide concentration. The curves have been normalized with respect to the electroactive areas of the UMEAs and the macroelectrode.

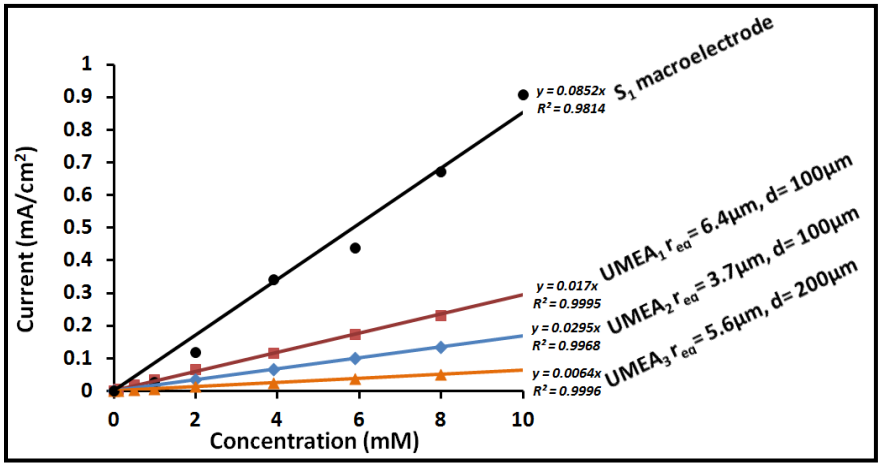

Figure 4. 10 Calibration curves plotted between the steady state currents and the ferrocyanide concentration. The curves have been normalized with respect to the total areas ($\mathbf{Nd^2}$) of the UMEAs and the macroelectrode.

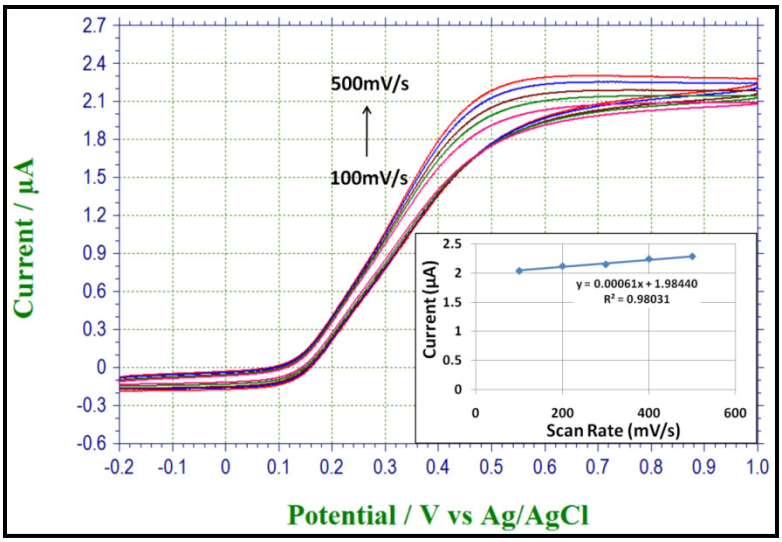

Figure 4. 11 CVs recorded in 0.1M KCl at 100mV/s, 200mV/s, 300mV/s, 400mV/s and 500mV/s for 8mM ferrocyanide by using $UMEA_3$;inset- plot of steady state current (µA) versus the scan rate (mV/s).

Electrochemical detection of bio-analytes with the UMEAs was examined by using **DA** in a 0.1M PBS solution. The pre-mixed PBS powder makes a solution of pH7.4 which is same as the physiologic pH and was not changed. CVs recorded at 10mV/s ($UMEA_1$) and 50mV/s ($UMEA_2$ and $UMEA_3$) by using the nanodiamond UMEAs as the working electrodes can be seen in figures 4.12(a), (b) and (c).

Steady state response was obtained which is consistent with hemi-spherical diffusion limited mass transport. The limiting currents increased with increase in DA concentration for all three UMEAs. Tomeš criterion, ($E_{3/4}-E_{1/4}$), which is the difference between the three-quarter wave potential and quarter wave potential, was found to be between 56 and (56/α) mV suggesting a quasi-reversible electrode kinetics [6].

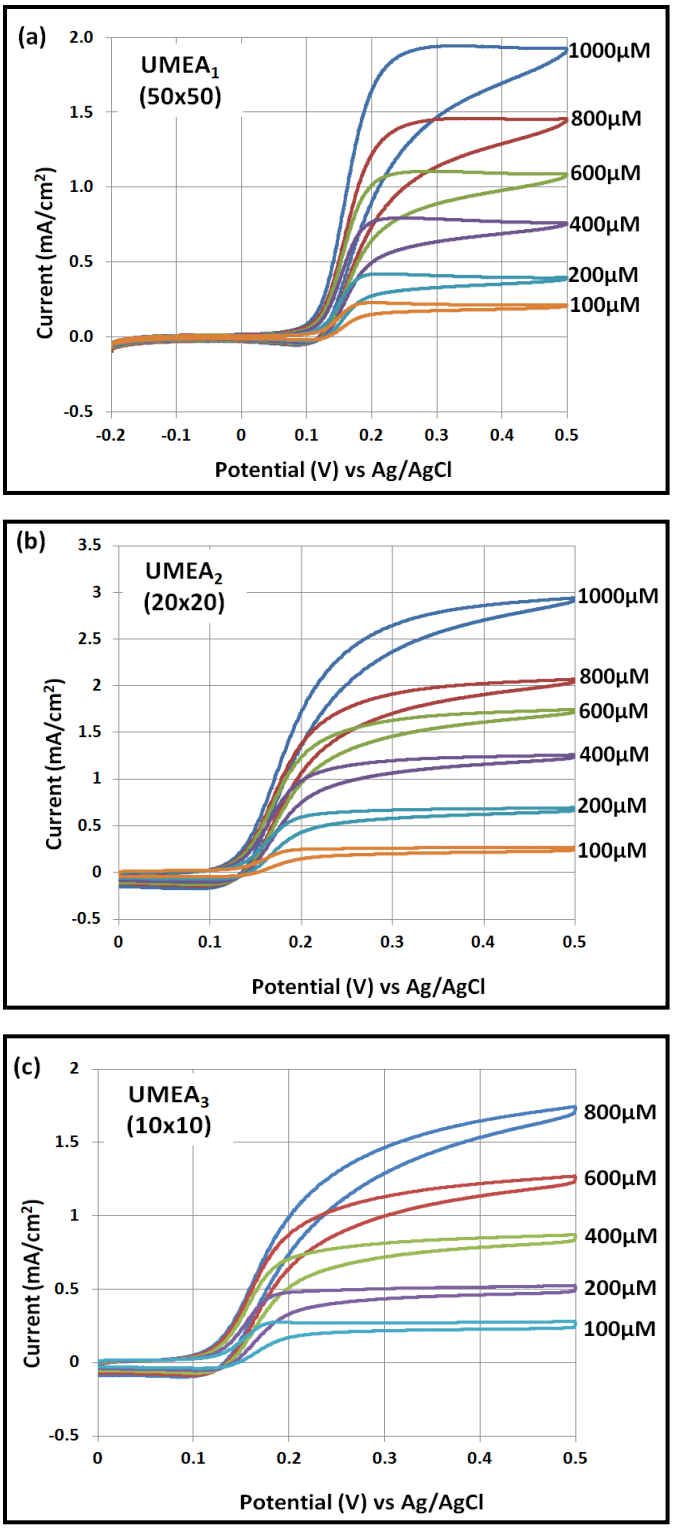

Figure 4. 12 Steady state CVs recorded in 0.1M PBS and pH7.4 at 10mV/s ($UMEA_1$) and 50mV/s ($UMEA_2$ and $UMEA_3$) for increasing concentrations of DA by using the nanodiamond UMEAs; (a) $UMEA_1$- 50x50 array, (b) $UMEA_2$- 20x20 array and (c) $UMEA_3$- 10x10 array.

The $E_{1/2}$ values do not follow the trend observed for ferrocyanide; $E_{1/2}$ ($UMEA_1$) = 0.16V → $E_{1/2}$ ($UMEA_2$) = 0.18V → $E_{1/2}$ ($UMEA_3$) = 0.18V. The secondary reactions downstream of DA oxidation, due to LDAC/DAC redox couple, were not observed. This was probably due to the narrow potential window used for recording this data which did not support those reactions.

The linear calibration curves plotted between the steady state currents (mA/cm^2) and DA concentration (µM) can be seen in figure 4.13. By using UMEAs, we were able to achieve much higher sensitivities for DA detection as compared to that from the macroelectrode **S_1 (0.3µA/cm^2.µM)**. $UMEA_1$ and $UMEA_3$ show similar sensitivities which is ***6x*** the value for S_1 respectively. $UMEA_2$ has the highest sensitivity, ***9x*** that of S_1. This enhancement highlights the advantage of miniaturization of electrode dimensions.

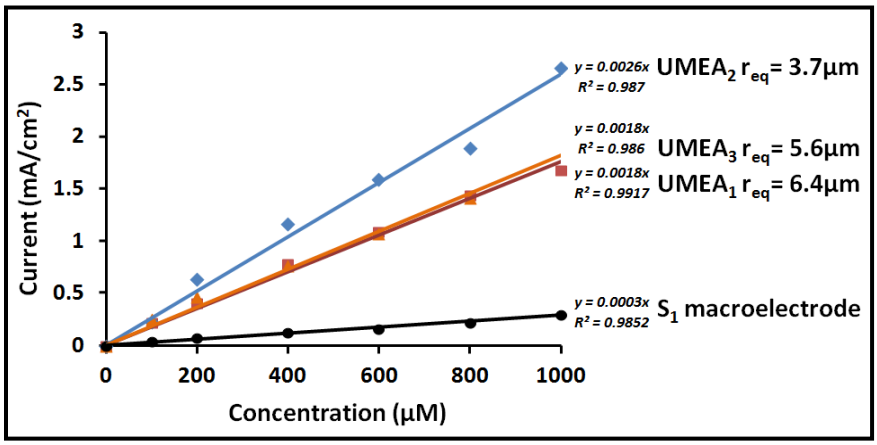

Figure 4. 13 Linear calibration curves plotted between the steady state currents and the DA concentration. The curves have been normalized with respect to the electroactive areas of the UMEAs and the macroelectrode.

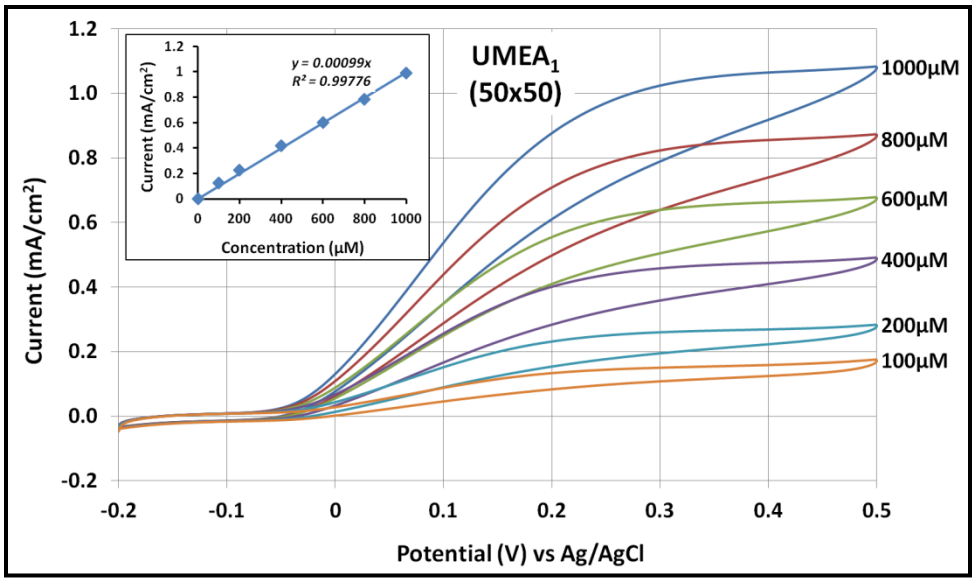

Figure 4. 14 Steady state CVs recorded in 0.1M PBS and pH7.4 at 10mV/s for increasing concentrations of AA by using $UMEA_1$- 50x50 array; inset- linear calibration plot between limiting currents (mA/cm^2) and AA concentration (µM).

Ascorbic acid (AA) exists in high concentrations in the extra-cellular fluid of the brain and can be detected by electrochemical techniques [84]. $UMEA_1$ was used to detect the presence of different concentrations of AA in 0.1M PBS and pH7.4. The steady state CVs recorded for AA at 10mV/s can be seen in figure 4.14 and the linear calibration curve plotted between the limiting currents (mA/cm^2) and AA concentration (µM) can be seen in the inset. The $UMEA_1$'s sensitivity value for AA detection was **0.99µA/cm^2.µM**.

Further, DA was added to a 1000µM AA solution to study the response for DA detection in the presence of AA. In a multi-component system like this, the signal due to AA oxidation is superimposed over the signal due to DA oxidation [144]. CVs recorded at 10mV/s for increasing DA concentrations (100µM, 200µM, 400µM, 600µM, 800µM and 1000µM) in 1000µM AA solution can be seen in figure 4.15. The CV shape changes and the steady state currents increase with DA addition. This

effect is further made clear in the inset of figure 4.15. The oxidation of the *AA+DA* solution in PBS starts at a slightly higher potential than that recorded for only AA.

The steady state current for each CV is the sum of ($i_{1000\mu M\ AA} + i_{x\mu M\ DA}$), where ***x*** is the DA concentration (100, 200, 400, 600, 800 and 1000). The plot corresponding to the limiting currents versus DA concentration can be seen in figure 4.16 in blue and is labeled as '1000µM AA+ DA'. In order to derive the calibration plot due to the contribution of DA oxidation alone, the signal due to 1000µM AA, recorded previously, was subtracted which gave a sensitivity value of **1.2µA/cm^2.µM**. The linear plot hence obtained is shown in red in figure 4.16 and labeled as 'DA'.

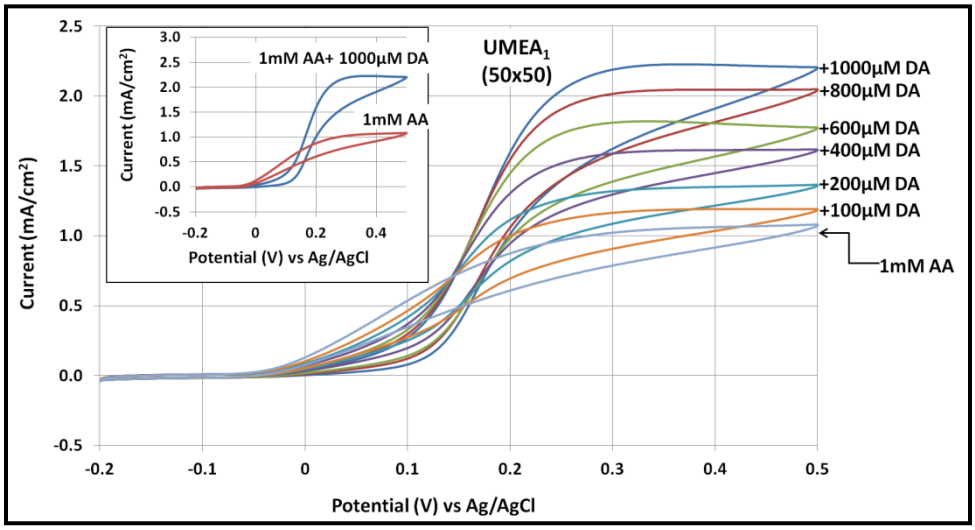

Figure 4. 15 Steady state CVs recorded in 1000µM AA solution in PBS and pH7.4 at 10mV/s for increasing concentrations of DA by using UMEA$_1$- 50x50 array; inset- steady state CVs for only1000µM AA in blue and for 1000µM AA+1000µM DA in red.

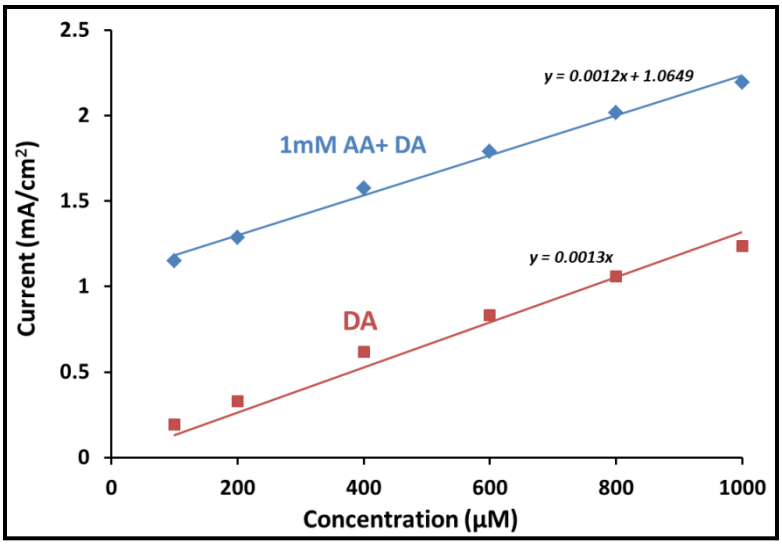

Figure 4. 16 Calibration plot based on the cumulative signal from AA and DA labeled as '1000µM AA + DA' in blue and the extracted calibration plot corresponding to the contribution of DA, labeled as 'DA' in red.

Uric acid (UA) is also an electrochemically active bio-analyte found in the body and interferes with the detection of DA [85-88]. $UMEA_1$ was used to detect the presence of different concentrations of UA in 0.1M PBS and pH7.4. The steady state CVs recorded for UA at 10mV/s can be seen in figure 4.17 and the linear calibration curve plotted between the limiting currents (mA/cm^2) and UA concentration (µM) can be seen in the inset. The $UMEA_1$'s sensitivity value for UA detection was **1.3µA/cm^2.µM**. A subtle feature at 0.55V was observed in the CVs recorded for UA which can be attributed to secondary redox reactions due to products formed downstream of UA oxidation.

Performance of nanodiamond electrodes have been compared with results from other electrode materials for detection of ferrocyanide and DA in appendix C, tables C.1 and C.2.

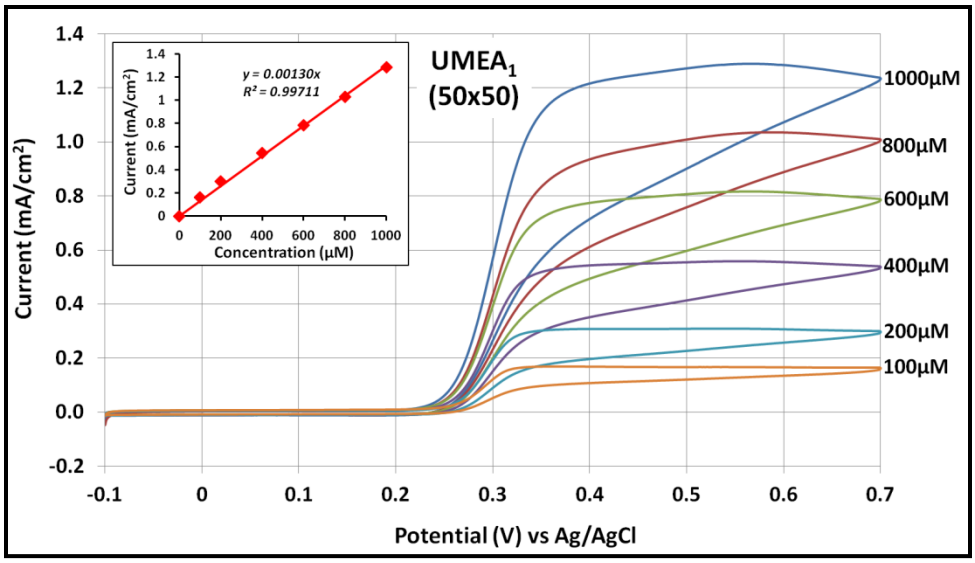

Figure 4. 17 Steady state CVs recorded in 0.1M PBS and pH7.4 at 10mV/s for increasing concentrations of UA by using $UMEA_1$- 50x50 array; inset- linear calibration plot between limiting currents (µA) and UA concentration (µM).

4.3 Fast scan cyclic voltammetry for dopamine detection

UMEAs, as discussed in the previous sections, have many advantages over macroelectrodes, such as higher rates of mass transport of the analyte to the UMEA surface, improved S/N ratio due to low capacitance, lower currents that result in lower iR_u losses due to uncompensated resistance, and perform experiments with high temporal and spatial resolution [6-8].

The value of the electrode time constant, $\tau = R_u C_d$, where R_u is the uncompensated resistance between the working electrode and the reference electrode and C_d is the double layer capacitance, determines its temporal resolution. The value of R_u varies inversely with r, the size of the electrode, while C_d increases with r^2 [6]. However, on the whole, $R_u C_d$ varies linearly with the size of the electrode [6]. By using an UME, this time constant can be reduced substantially, as compared to a macroelectrode, which in turn lowers the limit of the time scale that can be used in the electrochemical experiments [6].

This is critical for in-vivo electrochemical analysis of neurotransmitters whose concentrations may vary on a sub-second time scale [39, 54,144-145].

Fast scan cyclic voltammetry (FSCV) with scan rates greater than 100V/s can be used to identify and quantify rapid changes in the concentrations of redox active bio-analytes [39, 54,144-148]. No other technique provides such qualitative and quantitative information with high temporal resolution and selectivity [144-148].

At very short time scale, as in fast scan cyclic voltammetry (FSCV), the diffusion layer thickness is relatively smaller than the radii of the microelectrodes and semi-infinite linear diffusion (planar diffusion) is dominant, as seen in figure 2.4(a). The peak oxidation and reduction currents scale up linearly with the square root of the scan rate, as expressed in equation 3.2. However, at the same time, the background currents due to double layer capacitance and redox reactions of surface attached functional groups scale up with the scan rates, as seen in equation 3.3 [148]. This makes direct data analysis difficult. To overcome this drawback, the background signal recorded initially is subtracted from that obtained after adding the redox active analytes. Background subtracted FSCV has since become popular for studying sub-second variations in catecholamine levels [144-148].

Researchers have identified that further improvement in sensitivity for DA detection can be achieved by surface adsorption which results in pre-concentration of DA on the electrode surface prior to oxidation [144-147]. One reason for DA adsorption on the surface is due to electrostatic interaction between a negative holding potential at the electrode surface and the positively charged DA molecules at physiologic pH 7.4 [146-147]. A second reason suggested is change in the surface chemistry due to potential

sweep excursions above 1V vs. Ag/AgCl reference, which leads to formation of surface oxides, which may be a reversible process [146-147]. In case of gold microelectrodes, this occurs at potentials less than 1V, but leads to formation of an oxide monolayer [147]. Conventional carbon based microelectrodes tend to form oxygen functional groups on surface sites, which can be in the form of ketones (-C=O), carboxylic acid (-C-COOH) or hydroxyl groups (-C-OH) [146-147]. A third reason is an increase in the active surface area, which is particularly true in case of electrode materials such as carbon fibers and graphite foils [147]. Multiple exposures and longer hold times at potentials exceeding 1V vs. Ag/AgCl reference has been responsible in change in surface morphology (increase in area) or degradation due to etching (decrease in surface area) [147].

Adsorption of a specie, electroactive or electro*in*active, changes the electrode response for detection of an analyte which can be seen in the resulting cyclic voltammograms [147]. Peaks of adsorbed species (electroactive) may occur earlier than those due to diffusion limited mass transport from the bulk of the solution depending on the experimental parameters [146,149].

4.3.1 Experimental set-up

The objective of the following experiments was to examine the application of nanodiamond UMEAs in FSCV for detection of bio-analytes, especially DA. At such fast scan rates, planar diffusion is dominant and UMEAs with larger electroactive area are desirable for in-vitro experiments as they generate bigger signal. Therefore, **$UMEA_1$**, which consists of a 50x50 array of nanodiamond UMEs was employed in this work.

Application of a triangular waveform at a scan rate of 300V/s and repeated at a frequency of 10Hz simulates sub-second transient events of DA release in the brain [144-148]. In order to enhance sensitivity for DA, a negative holding potential of -1.0V for 100ms was used in between the FSCV scans resulting in DA pre-concentration on the surface. This effect relies on electrostatic forces of interaction between the UMEA and the DA cations. The large cathodic potential limit also allowed examination of secondary redox reactions occurring downstream of DA oxidation, which resulted in an extra pair of redox peak at slower scan rates.

The anodic potential limits were varied from 0.8V to 1.4V in steps of 200mV, labeled as A (-1V to +0.8V), B (-1V to +1.0V), C (-1V to +1.2V) and D (-1V to +1.4V). The FSCV waveform can be seen in figure 4.18 for the scan window D. This enabled the study of stability of the UMEA surface chemistry and microstructure, which changes in case of carbon fiber microelectrodes at potentials greater than 1V. Background signals in 0.1M PBS at pH7.4 were recorded for each scan window prior to addition of DA. This data was used to generate background subtracted CVs for different concentrations of DA. The experimental parameters used for FSCV have been summarized in table 4.2.

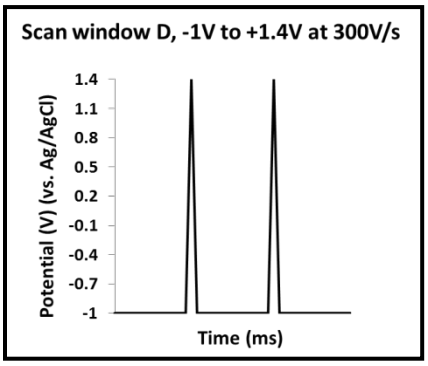

Figure 4. 18 A typical triangular waveform used for FSCV experiments: Potential window of -1V to +1.4V at a scan rate of 300V/s.

Table 4. 2 FSCV parameters for DA detection.

FSCV Scan Rate (ν) = 300V/s (for different DA concentrations)		
Scan Window Label	**Potential Scan Limits**	**Time/Cycle (ms)**
A	-1V to +0.8V	12
B	-1V to +1.0V	13
C	-1V to +1.2V	15
D	-1V to +1.4V	16

4.3.2 Results and Discussions

Background subtracted FSCV voltammograms recorded at 300V/s for different DA concentrations (100µM, 200µM, 400µM, 600µM, 800µM and 1000µM) can be seen in figure 4.19. As predicted, a peak shaped response is observed which is consistent with semi-infinite linear diffusion or planar diffusion limited mass transport. However, this interpretation is not completely correct.

For potential scan windows A and B, figures 4.19 (a) and (b) respectively, there is only one oxidation peak at 0.7V which increases in height with increase in DA concentration. For the larger scan windows, C and D, the presence of 2 peaks can be clearly observed, figures 4.19 (c) and (d) respectively. The first peak located at 0.7V is common for all scan windows, but a broader wave at 1V can only be resolved for windows with anodic potential limits of 1.2V and 1.4V. Such a response is seen for systems where the reactant is electroactive and is also adsorbed on the electrode surface [146,149]. The first peak can be attributed to the adsorbed DA while the second peak results from diffusion of the analyte from the bulk of the solution.

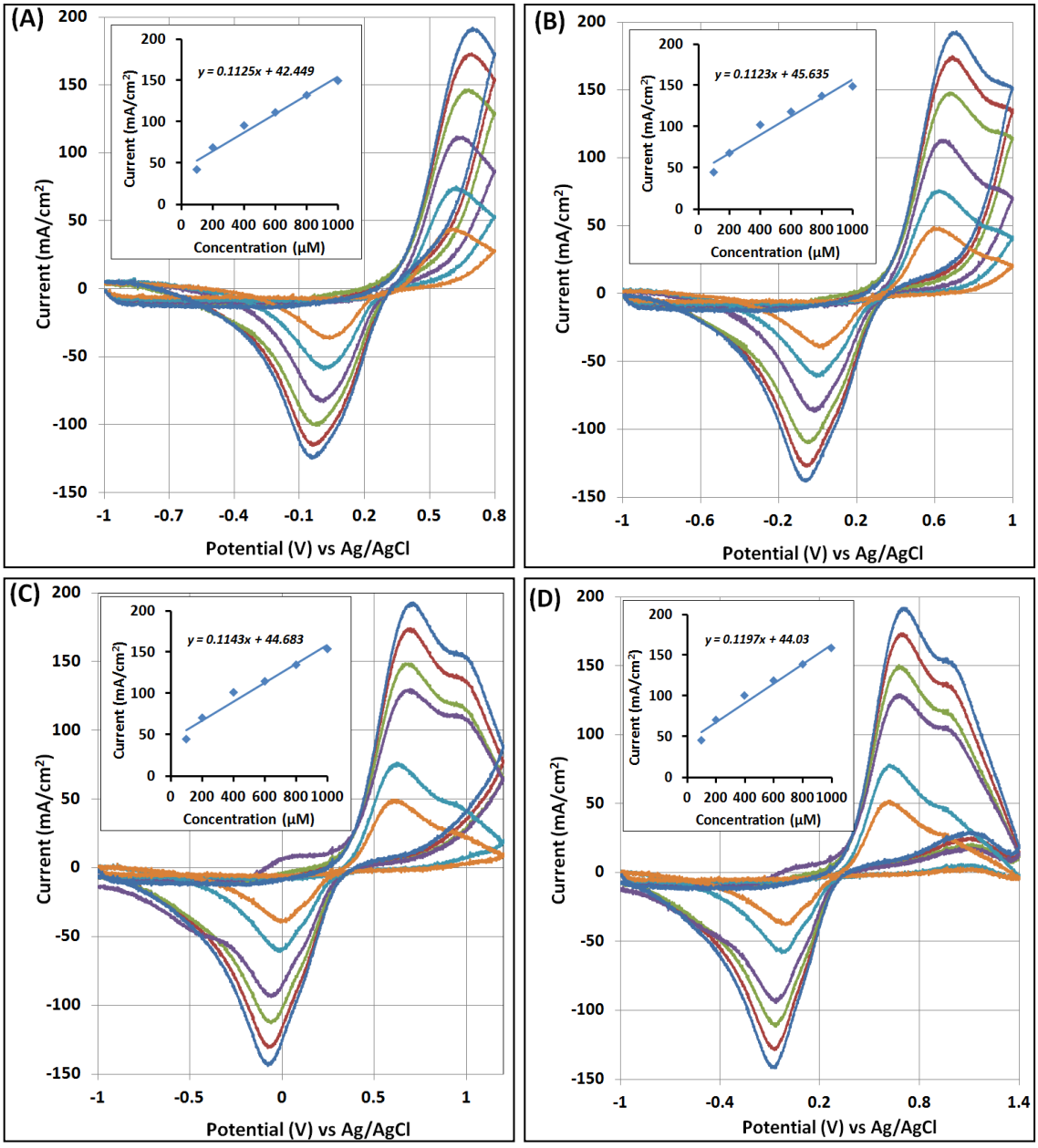

Figure 4. 19 FSCV voltammograms recorded using nanodiamond UMEA1 at 300V/s for different DA concentrations (100µM, 200µM, 400µM, 600µM, 800µM and 1000µM) in 0.1M PBS solution at pH7.4; inset- linear calibration plots.

Calibration curves plotted between peak oxidation current (adsorption peak) (mA/cm^2) vs. DA concentration (µM), show a linear behavior for all the scan windows as seen inset in figures 4.19 (A) to (D). The sensitivity of an electrode can be calculated

from the slope of the calibration curves. In these experiments, all four cases have comparable values of **~115μA/cm^2.μM**. However, this is nearly **400*x*** that reported for the macroelectrode S_1 for DA detection at slower scan rates. Also, it is almost **45*x*** that reported for the same electrode, $UMEA_1$, at 100mV/s. **This clearly demonstrates the superior sensitivity of FSCV technique for DA detection.**

The reason for similar sensitivity observed for all scan windows was further examined by overlaying the corresponding CVs recorded for 1mM DA at 300V/s, as seen in figure 4.20. The adsorption peak (#1) and diffusion peak (#2) have been clearly labeled and are prominent in case of CVs C and D. The CVs show excellent overlap for the anodic sweep segment, and only the reduction peaks showed some observable distinction. There is no evidence of any signal due to the LDAC/DAC redox couple, electroactive products formed downstream of DA oxidation at slower scan rates. The chemical reaction involving transformation of dopamine-o-quinone to leucodopaminechrome has very slow kinetics, which is why, by using FSCV, this chemical reaction was suppressed.

The reduction peaks for the four potential windows increase in the order D=C > B > A. This difference arises due to the larger over potential for DA oxidation (ΔV= 0.2V and 0.4V) which generates greater amount of dopamine-o-quinone and thus a larger reduction peak.

Studies performed on carbon fiber based electrodes have shown an increase in sensitivity by cycling to potentials greater than 1V and also, shift in the peak potential locations [146-147]. This is due to generation of greater number of sites of oxygen

functional groups on the surface and/or an increase in surface area due to change in the microstructure due to such potential excursions, both of which increase DA adsorption sites. However, in case of $UMEA_1$, no enhancement was observed as the anodic potential limit was increased from +0.8V to +1.4V. **This is a clear indication that nanodiamond UMEA provides a very stable platform for sensitive detection of DA as there is no change in the surface chemistry or microstructure in the UMEA**.

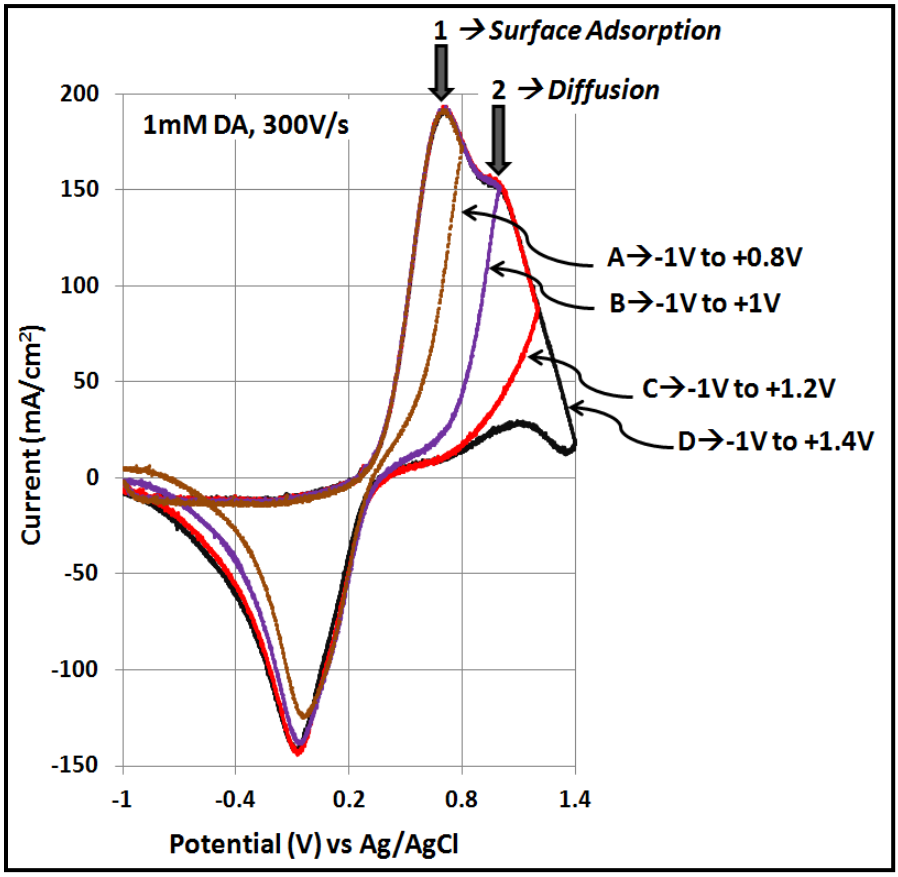

Figure 4. 20 FSCV voltammograms recorded for 1mM DA at 300V/s in PBS for different potential scan windows (A, B, C and D) depicting the effect of adsorption in form of peak 1 which appears before the one due to diffusion limited mass transport of DA. All 4 CVs show a close overlap for the anodic sweep segment.

Similar work done for detecting DA using FSCV considered smaller potential windows of -0.4V to 1V or 1.3V[144-145,147-148,150-151]. The results indicated an improvement in sensitivity when an anodic potential limit of 1.3V was chosen over 1V, due to reasons discussed previously. However, this improvement came at the cost of decrease in the temporal resolution [144-145,147-148,150-151]. Also, the CVs recorded consisted of cumulative signal due to adsorption and diffusion which made their independent analysis difficult. By using nanodiamond $UMEA_1$ and a more negative holding potential of -1V, the effect or contribution of adsorption was greatly enhanced allowing for easier analysis.

The PBS solution was made from a pre-mixed powder mixture of sodium chloride (NaCl), potassium chloride (KCl), sodium phosphate (Na_2HPO4) and potassium phosphate (K_2HPO4) of fixed concentrations. This buffer solution helps to maintain constant pH and mimics the physiologic ionic concentrations. However, the use of this electrolyte limits the use of other electrode materials such as gold. The anodic scan limit should be limited to 0.7V vs. Ag/AgCl reference because of large corrosion currents arising from oxidation of gold in presence of chloride ions to form $Au[Cl]_4^-$ at around 1.1V [147]. This also limits the number of bio-analytes that can be detected by a gold electrode. Nanodiamond UMEA does not have this limitation and is a viable electrode for electrochemical detection of bio-analytes.

4.4 Columnar ultramicroelectrode array- A better design

The planar nanodiamond UMEAs fabricated using the bottom-up approach discussed in section 4.2, were successfully able to detect various bio-analytes under slow and fast scan rate cyclic voltammetry. However, the fabrication process had some drawbacks including:

1. The UME molds created after wet-etch of molybdenum and SiO_2 (see figure 4.6(a)), had very rough edges/perimeter due to which nanodiamond growth rate in those areas was faster than at the base of the mold, on the silicon surface. Consequently, the UMEs ended up with a 'donut' structure; a thick perimeter with a flat surface in the center, as seen in see figures 4.7 (b), (d) and (f). The final size was always greater than that of the original mold leading to inconsistencies.

2. The nanodiamond microstructure showed a small variation in the 3 UMEAs as can be observed in figures 4.7 (b), (d) and (f). This variation can be linked to their electrochemical performance which also exhibited an inconsistency even though all three were able to successfully detect the bio-analytes with high sensitivity.

3. The molybdenum film which acted as a sacrificial mask to protect the underlying SiO_2 layer during the PECVD nanodiamond growth process would form a carbide layer. This layer was difficult to lift-off and did not quite serve its purpose.

In order to overcome these drawbacks, a new fabrication process was designed involving a top-down approach.

4.4.1 Fabrication and material characterization

Top-down fabrication: Among the critical requisites for producing UMEAs reproducibly are control over the nanodiamond microstructure and UME dimensions. This process provides excellent control over both of these parameters. A schematic diagram of the fabrication process can be seen in figure 4.21(a).

A highly doped n-type silicon substrate was used to grow a ~2μm thick nanodiamond film using PECVD process with the following parameters: Power = 1kW, Pressure = 25 torr, Substrate temperature = 850°C, Gas flow rates (H2/CH4/N2) = 135/15/15 sccm and Time = 7 hours. A 0.5μm thick aluminum film was deposited by DC sputtering technique on the nanodiamond layer. Conventional UV photolithography was used to pattern and develop the desired array layout. This was followed by wet etch of the exposed aluminum areas and photoresist lift-off. A dry etch process, reactive ion etch (RIE), was used to completely remove nanodiamond not protected by the aluminum mask. The RIE process was performed in a STS AOE machine with the following parameters: Pressure: 10mTorr, Power (RIE): 100 W, Power (ICP): 600 W, Gas: O_2, Flow rate: 30 sccm. This recipe gave an etch rate of ~0.2 μm/min.

IC1-200 is a polysiloxane-based spin-on dielectric material (SOG) dispersed in a solution of n-butanol. The application and baking procedure are as follows:

1. Spin coat at 3000 rpm for 40 s followed by baking at 200°C on a hot plate for 60s. This is repeated to apply a double coating of the SOG.

2. The last curing step includes baking at 400°C for 30minutes under a nitrogen atmosphere.

This SOG application process results in a 350-400nm thick dielectric layer after curing. Due to the centrifugal force, the liquid SOG tends to flow away from the nanodiamond UME posts. The last step involves aluminum lift-off using PAE aluminum etchant aided by ultrasonication. A two-dimensional cross-sectional representation of the final structure can be seen in figure 4.21(b).

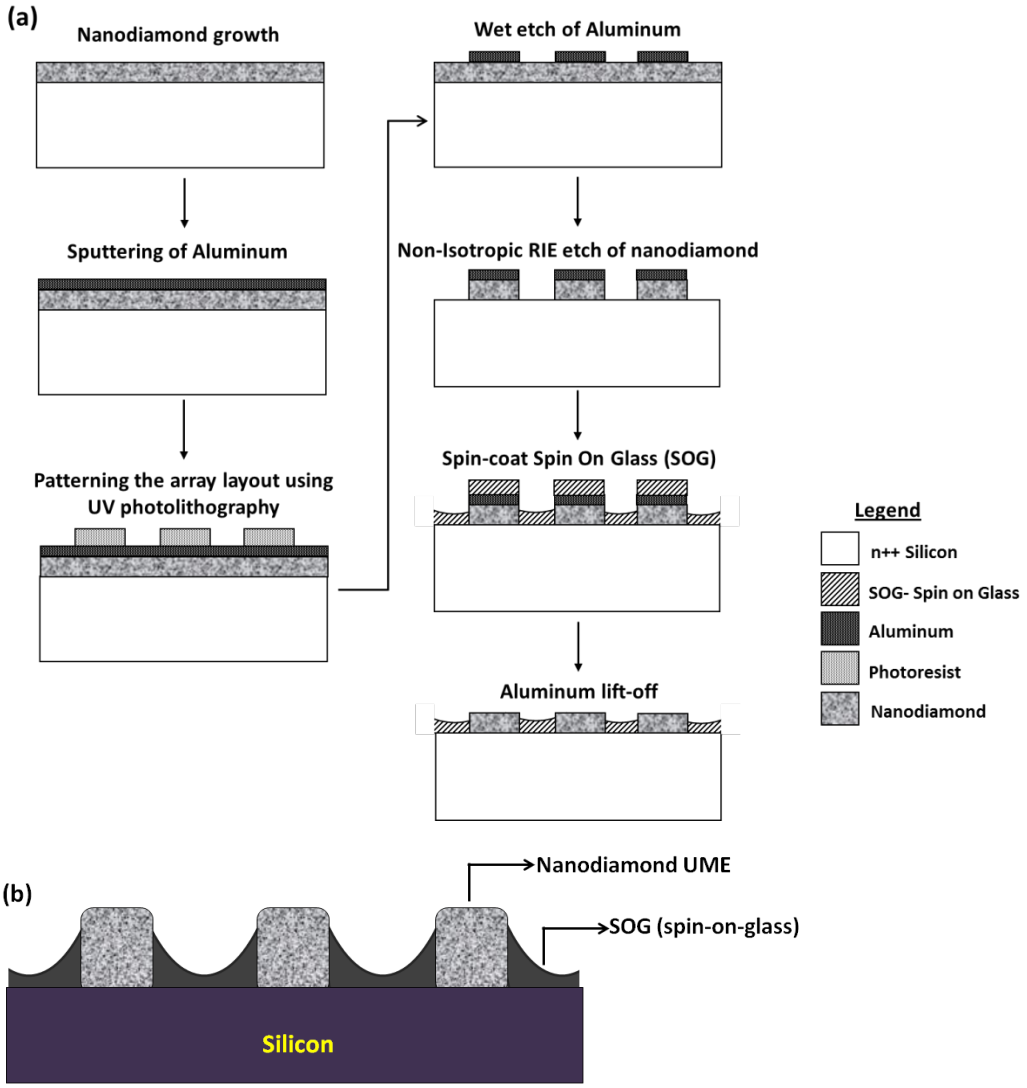

Figure 4. 21 (a) Schematic diagram of $UMEA_{RIE}$ fabrication. (b) 2-dimensional cross-sectional representation of the final structure of $UMEA_{RIE}$.

This process was used to fabricate nanodiamond **UMEA$_{RIE}$**, which consisted of 2500 UMEs arranged in a square layout (50x50). The original pattern consisted of discs with a diameter of 10μm and spacing of 100μm.

A low magnification SEM micrograph of UMEA$_{RIE}$ layout can be seen in figure 4.22 (a). The bright spots representing the UMEs separated by the insulating SOG matrix can be observed. A tilt view of 9 UMEs can be seen in figure 4.22 (b), while a high resolution SEM image of the nanodiamond microstructure can be seen in figure 4.22 (c). This microstructure is consistent with that observed for the macroelectrode S_1 discussed in chapter 3, resembling an assembly of ridges or platelets few nm wide with nanocrystallites on the side-walls and in between those ridges.

A tilt view of an individual UME after the nanodiamond RIE process with the aluminum mask layer on top can be seen on the left in figure 4.22 (d). The same figure displays the final UME structure after the SOG application and curing and aluminum lift-off, on the right. It must be noted that the geometry is different from that of UMEAs 1, 2 and 3. The array consists of UMEs projecting above the surrounding dielectric matrix. The amount of nanodiamond exposed can be controlled by varying the SOG spin-coating speed. The final diameter at the top is ~9μm.

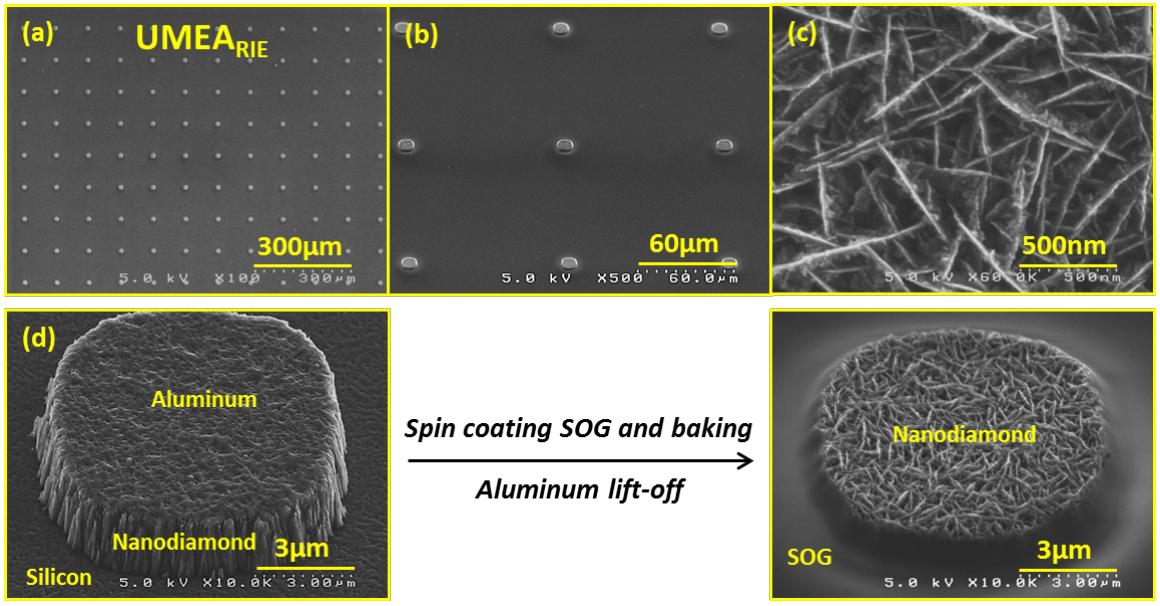

Figure 4. 22 (a) Low magnification SEM micrograph showing the UMEA layout, bright spots representing the UMEs separated by an insulating dielectric matrix; (b) SEM micrograph of a section of the UMEA obtained at 45° angle; (c) High resolution SEM image of the nanodiamond microstructure consisting of platelets few nm wide and with nanocrystallites on the sidewalls and in between them; (d) SEM micrograph of an individual UME after nanodiamond RIE step on the left and on the right, the final structure the same UME.

4.4.2 Electrochemistry

The approach to evaluate the electrochemical behavior of **UMEA$_{RIE}$** was similar to that discussed under section 4.2.2. Initial characterization of the nanodiamond UMEAs was performed by using the ferri-ferrocyanide redox couple $\mathbf{Fe(CN)_6^{-3/-4}}$ in 0.1M KCl as the supporting electrolyte. This redox reaction is accompanied with the transfer of one e^-; ferrocyanide is oxidized to form ferricyanide, as depicted by the following reaction.

$$Fe(CN)_6^{4-} \leftrightarrows Fe(CN)_6^{3-} + e^-$$

$$ferrocyanide \quad ferricyanide$$

CVs recorded at 100mV/s by using **$UMEA_{RIE}$** as the working electrodes can be seen in figure 4.23. Under these conditions sigmoidal response was observed, consistent with hemi-spherical diffusion limited mass transport. The individual diffusion layers did not overlap, thus preserving the UMEA response.

A linear calibration curve was plotted by using the steady state limiting current (μA) and the ferrocyanide concentration (mM). The slope of this graph was used in equation 4.2 to calculate the equivalent radius, r_{eq}, which assumed that the UMEs had a hemispherical geometry. This step was necessary in order to maintain consistency in performance comparison between the UMEAs fabricated in this research. $UMEA_{RIE}$ has r_{eq}= 3.6μm which is nearly same as that for $UMEA_2$ (3.7μm). The important dimensional quantities calculated for **$UMEA_{RIE}$** have been listed in table 4.3.

Table 4. 3 Nanodiamond $UMEA_{RIE}$ dimensions.

	$UMEA_{RIE}$ (50x50)
Total number of UMEs (N)	2500
radius each UME (disc) (μM)	4.5μm
Spacing (d) (μm)	100
Electroactive Area (geometric) (cm^2)	$1.589x10^{-3}$
Total Array Area ($N.d^2$) (cm^2)	0.25
Equivalent UME radius (r_{eq}) (μm)	***3.6***
Equivalent Area ($N.2\pi r_{eq}^2$) (cm^2)	$2.035x10^{-3}$

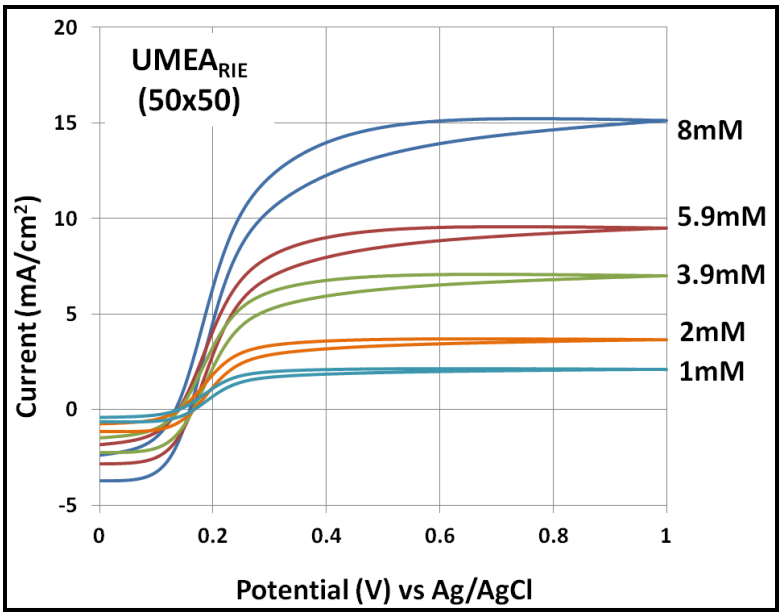

Figure 4. 23 CVs recorded in 0.1M KCl at 100mV/s for increasing concentrations of ferrocyanide by using the nanodiamond UMEAs; (a) UMEA1- 50x50 array, (b) UMEA2- 20x20 array and (c) UMEA3- 10x10 array.

The slope of the calibration curve also represents the sensitivity of that electrode and can be used to compare the response between multiple electrodes. Based on the calibration plots seen in figure 4.24, UMEA$_{RIE}$ sensitivity for ferrocyanide detection is nearly **2.0396mA/cm^2.mM**. This is almost ***24x*** that observed for electrode S_1. Also, since the difference in the equivalent radii for UMEA$_2$ (3.7µm) and UMEA$_{RIE}$ (3.6µm) is very small, the corresponding calibration plots show a close overlap.

These results are consistent with the observations made earlier, also seen in figure 4.9, i.e., as the UME dimensions decrease, their sensitivity values increase. UMEAs develop higher analyte flux densities at the surface than macroelectrodes by hemispherical diffusion due to their size and geometry and hence exhibit higher sensitivity.

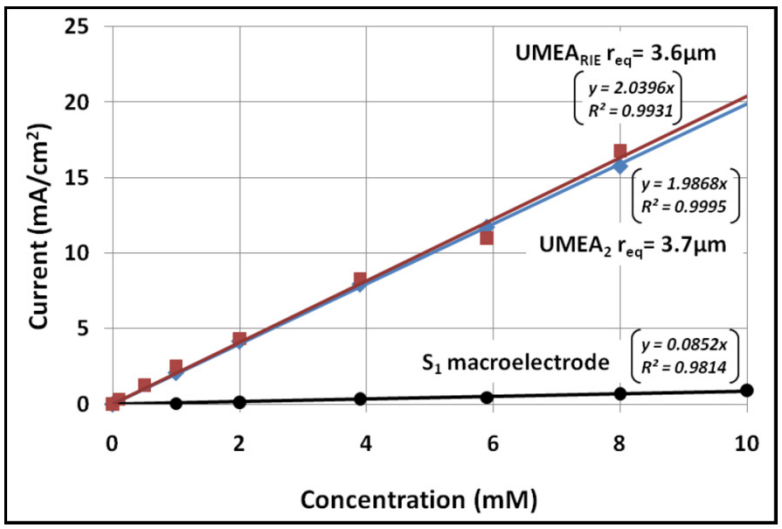

Figure 4. 24 Linear calibration plots obtained for $UMEA_{RIE}$, $UMEA_2$ and S_1 showing the improvement in ferrocyanide sensitivity with decrease in the electrode dimensions.

Electrochemical detection of bio-analytes with the UMEAs was examined by using **DA** in a 0.1M PBS solution at pH7.4. CVs recorded at 100mV/s for different DA concentrations (100µM, 200µM, 400µM, 600µM, 800µM, and 1000µM) can be seen in figure 4.25. Steady state limiting currents increased with increase in DA. Tomeš criterion, ($E_{3/4}$−$E_{1/4}$), which is the difference between the three-quarter wave potential and quarter wave potential, was found to be between 56 and (56/α) mV suggesting a quasi-reversible electrode kinetics [6].

The linear calibration curves plotted between the steady state currents (mA/cm^2) and DA concentration (µM) can be seen in figure 4.26. The enhancement in sensitivity by use of a UMEA over a macroelectrode is evident by the difference in the corresponding slopes. By virtue of comparable UME dimensions, $UMEA_{RIE}$ and $UMEA_2$ show a close overlap in their response. The sensitivity calculated for $UMEA_{RIE}$ was around **2.7µA/cm^2.µM**, which is nearly ***9x*** that obtained by S_1 macroelectrode.

Performance of nanodiamond electrodes have been compared with results from other electrode materials for detection of ferrocyanide and DA in appendix C, tables C.1 and C.2

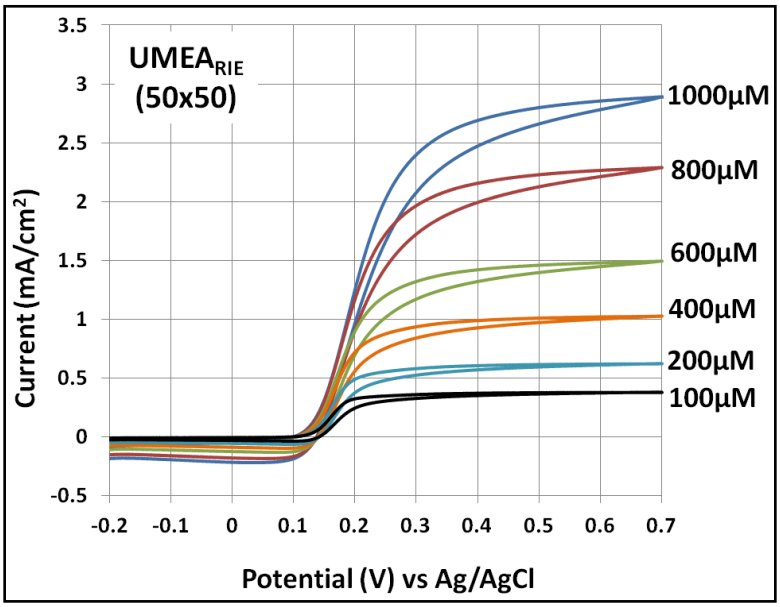

Figure 4. 25 CVs recorded for different DA concentrations at 100mV/s in 0.1M PBS solution at pH7.4 using UMEA$_{RIE}$.

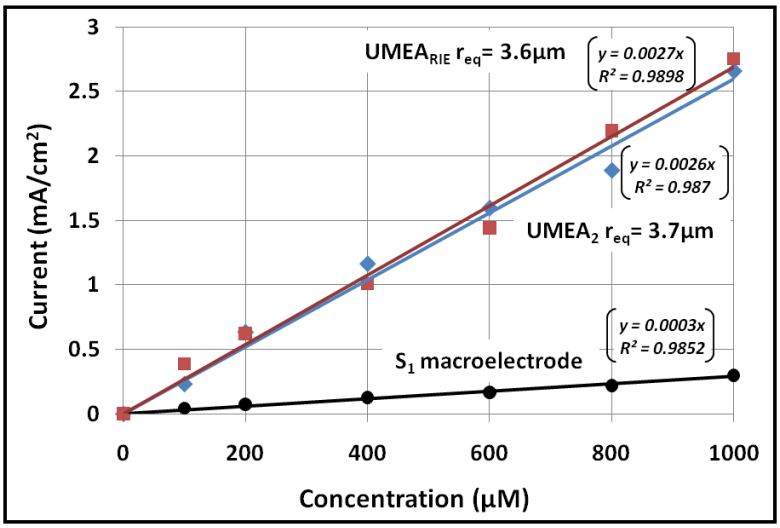

Figure 4. 26 Linear calibration plots obtained for UMEA$_{RIE}$, UMEA$_2$ and S$_1$ showing the improvement in sensitivity for DA detection with decrease in the electrode dimensions.

4.5 Summary

- Nitrogen incorporated nanodiamond UMEAs with pyramidal geometry were successfully fabricated on highly doped n-type silicon substrates with tips formed by a combination of thermal oxidation, UV photolithography and isotropic acid etch of silicon.
- In the first fabrication approach, the silicon substrate with tips was thermally oxidized (0.5μm), followed by a partial SiO_2 etch-back to expose underlying silicon at the tips. Nanodiamond was selectively grown on those silicon tips.
- The second fabrication process involved growth of nanodiamond film over the entire silicon substrate with tips followed by e-beam deposition of 0.2μm quartz which was then partially etched back.
- Nanodiamond UMEAs with pyramidal geometry did not exhibit good electrochemical response. The drawbacks included poor electrical conductivity of nanodiamond, difficulty in achieving selective nanodiamond growth on the tips, poor adhesion between the quartz and nanodiamond layers and susceptibility to mechanical damage due to fragile structure.
- Planar nanodiamond UMEAs were also successfully fabricated with each 'donut' shaped UME projecting above the surrounding SiO_2 insulating matrix.
- The fabrication process involved thermal oxidation of highly doped n-type silicon substrate (0.5μm), DC sputtering of molybdenum (0.5μm), defining the array layout by conventional UV photolithography followed by wet etch to remove the

exposed Mo and SiO_2. MPECVD nanodiamond was grown in the exposed silicon regions and then the protective Mo layer was lifted off.

- Three UMEAs were fabricated: $UMEA_1$- 50x50 array, 15µm edge, 100µm pitch; $UMEA_2$- 20x20 array, 5µm radius, 100µm pitch and $UMEA_3$- 10x10 array, 7.5µm radius, 200µm pitch.
- All three UMEAs exhibited quasi-reversible steady-state response for ferrocyanide and DA detection. $UMEA_2$ showed the highest sensitivity of 1.9868mA/cm^2.mM for ferrocyanide which was almost 23*x* times higher than that observed for the macroelectrode S_1. The sensitivity for DA detection using $UMEA_2$ was 2.6µA/cm^2.µM for DA, nearly 9*x* times the value for S_1.
- The performance of $UMEA_2$, which had the lowest equivalent radius of 3.7µm, is consistent with the fact that as the electrode dimensions decrease, the analyte flux density increases resulting in greater sensitivity.
- The nanodiamond $UMEA_1$ was also able to detect AA (0.99µA/cm^2.µM) and UA (1.3µA/cm^2.µM). In addition to this, the detection of DA in presence of AA was demonstrated with a sensitivity value of 1.2µA/cm^2.µM.
- High temporal resolution is critical for in-vivo study of neurotransmitters and can be simulated by using fast scan cyclic voltammetry at 300V/s on $UMEA_1$.
- Background subtracted FSCV was used to record CVs for dopamine detection by varying the anodic potential limit from 0.8V to 1.4V with a holding potential of −1V.

- Surface adsorption due to pre-concentration at -1V and semi-infinite linear diffusion conditions resulted in a dual peak CV only observed for the two largest scan windows.
- An average sensitivity value of 115μA/cm^2.μM was recorded using FSCV which is nearly 400*x* than that observed for S_1at slower scan rates, thus highlighting the benefits of this technique.
- Columnar $UMEA_{RIE}$ was fabricated by using a top-down approach in order to overcome drawbacks in the planar UMEA fabrication process.
- Planar nanodiamond film was grown on a silicon substrate followed by sputtering of aluminum. Conventional UV photolithography was used to delineate the array layout followed by a RIE process to dry etch the exposed nanodiamond film thus creating columns under the Al mask. A spin-on-glass was used to create an insulating matrix followed by Al lift-off.
- $UMEA_{RIE}$ exhibited steady state response with linear calibration plots for detection of ferrocyanide and DA consistent with hemispherical diffusion. The equivalent radius of 3.6μm was comparable to that calculated for $UMEA_2$, thus resulting in close electrochemical responses.
- All these results were achieved without any surface functionalization and/or modification.

CHAPTER V

CONCLUSIONS AND FUTURE WORK

5.1 Conclusions

5.1.1 Nanodiamond thin-film macroelectrodes

Nitrogen incorporated nanodiamond thin-film macroelectrodes were successfully fabricated by MPECVD synthesis process on highly doped silicon substrates. The input gas mixture in this process consisted of hydrogen, methane as the carbon source and nitrogen. Under fixed power, pressure and temperature conditions, the relative concentration of the three gases has a very strong influence on the nanodiamond growth, microstructure and material properties.

High percentage of CH_4 with respect to H_2, ranging from 12.5% to 20%, yielded a very sparse nanodiamond growth consisting of small gain clusters about 10μm in diameter randomly distributed on the silicon substrate. Short life-times of reaction intermediates in the MPECVD process could cause such a disrupted and random growth process. Thus, these samples could not be used as electrodes.

Continuous and uniform nanodiamond films were synthesized by using lower levels of CH_4, about 10% of H_2. However, variation of the nitrogen gas concentration in the input gas mixture from 9.1% to 37.5% produced variations in the corresponding nanodiamond films. Macroelectrodes S_1 (9.1% N_2) and S_2 (16.7%) had similar microstructures consisting of ridges/ nanoplatelets which were few nanometers wide by about 1μm long in case of S_1 and 500nm in case of S_2 and nanocrystallites in between

those platelets and on the sidewalls. As the N_2 flow rate was increased to 28.6% (S_3) and 37.5% (S_4), there was a transition from the platelet like microstructure to a more small grain clusters. Electrical resistance increased from 10-30Ω in case of S_1 and S_2 to 10-30MΩ for S_3 and S_4. Increase in N_2 flow rate resulted in an increase in the relative sp^2 hybridized carbon content as confirmed by the increase in the graphitic peak intensity in the Raman spectra and XPS data. There was also an increase in the carbon-nitrogen bond content, as observed in the C1s XPS data, which can explain the decrease in electrical conductivity with increase in nitrogen.

The CV response for detection of ferrocyanide in 0.1M KCl and dopamine in 0.1M PBS at pH7.4 using electrodes S_3 and S_4 exhibited broad peaks with poor definition and a large peak-peak separation consistent with poor electron transfer kinetics, making them unsuitable candidates for use in electroanalytical applications. This directly correlates to the poor electrical conductivities of the corresponding nanodiamond films. In contrast, S_1 and S_2 show sharp and well defined redox peaks with small peak-peak separation for ferrocyanide and dopamine suggesting rapid electron transfer kinetics and a quasi-reversible response.

Electrode S_1's sensitivity values for ferrocyanide and dopamine detection based on the respective linear calibration plots was 85μA/cm^2.mM and 0.3μA/cm^2.μM respectively. In addition to being able to independently detect interferant bio-analytes such as ascorbic acid and uric acid, S_1 was also able to successfully detect and quantify dopamine in their presence (1mM AA and 1mM UA) with a sensitivity value of 0.25μA/cm^2.μM.

These results have been achieved without any surface modification and/or functionalization and have been unmatched by boron-doped diamond electrodes.

5.1.2 Pyramidal Nanodiamond UMEAs

Nitrogen incorporated nanodiamond UMEAs with pyramidal geometry were successfully fabricated on highly doped n-type silicon substrates with tips formed by a combination of thermal oxidation, UV photolithography and isotropic acid etch of silicon. In the first fabrication approach, the silicon substrate with tips was thermally oxidized (0.5μm), followed by a partial SiO_2 etch-back to expose underlying silicon at the tips. Nanodiamond was selectively grown on those silicon tips. The second fabrication process involved growth of nanodiamond film over the entire silicon substrate with tips followed by e-beam deposition of 0.2μm quartz which was then partially etched back.

Nanodiamond UMEAs with pyramidal geometry did not exhibit good electrochemical response. The drawbacks included poor electrical conductivity of nanodiamond, difficulty in achieving selective nanodiamond growth on the tips, poor adhesion between the quartz and nanodiamond layers and susceptibility to mechanical damage due to fragile structure.

5.1.3 Planar Nanodiamond UMEAs

Planar nanodiamond UMEAs were also successfully fabricated with each 'donut' shaped UME projecting above the surrounding SiO_2 insulating matrix. The fabrication process involved thermal oxidation of highly doped n-type silicon substrate (0.5μm), DC

sputtering of molybdenum (0.5µm), defining the array layout by conventional UV photolithography followed by wet etch to remove the exposed Mo and SiO_2. MPECVD nanodiamond was grown in the exposed silicon regions and then the protective Mo layer was lifted off. Three UMEAs were fabricated: $UMEA_1$- 50x50 array, 15µm edge, 100µm pitch; $UMEA_2$- 20x20 array, 5µm radius, 100µm pitch and $UMEA_3$- 10x10 array, 7.5µm radius, 200µm pitch.

The response of an UMEA depends on the experimental time scale. At very slow scan rates or large time scales, the diffusion layer thickness is much larger than the UME dimensions resulting in a pseudo-macroelectrode response with peak shaped CVs consistent with semi-infinite linear diffusion dominated mass transport. At smaller time scales, the diffusion layer thickness grows larger than the UME dimension at which point hemispherical diffusion is dominant and a steady state CV response is observed. These steady state conditions were used for characterization of the UMEAs because higher analyte flux densities can be achieved and data analysis is less complicated.

All three UMEAs exhibited quasi-reversible steady-state response for ferrocyanide and DA detection. $UMEA_2$ showed the highest sensitivity of 1.9868mA/cm^2.mM for ferrocyanide which was almost 23*x* times higher than that observed for the macroelectrode S_1. The sensitivity for DA detection using $UMEA_2$ was 2.6µA/cm^2.µM for DA, nearly 9*x* times the value for S_1. Signal due to the Leucodopaminechrome/Dopaminechrome redox couple observed in case of S_1 is not seen in these experiments due to the use of a smaller potential scan window.

The performance of $UMEA_2$, which had the lowest equivalent radius of 3.7µm, is consistent with the fact that as the electrode dimensions decrease, the analyte flux density

increases resulting in greater sensitivity. The nanodiamond $UMEA_1$ was also able to detect AA (0.99μA/cm^2.μM) and UA (1.3μA/cm^2.μM). In addition to this, the detection of DA in presence of AA was demonstrated with a sensitivity value of 1.2μA/cm^2.μM. **These results indicate the superior electrochemical performance of UMEAs over the macroelectrodes and the capability of using nanodiamond UMEAs for bio-analyte detection.**

5.1.4 Fast Scan Cyclic Voltammetry

In-vivo electrochemical analyses of neurotransmitters whose concentrations may vary on a sub-second time scale require electrodes with high temporal and spatial resolution. The temporal resolution of an electrode depends on the *RC* time constant τ which varies linearly with the electrode dimensions. Thus, by using an ultramicroelectrode, higher temporal resolution can be easily achieved.

The time scale of rapid concentration fluctuations of neurotransmitters can be simulated by using fast scan cyclic voltammetry (FSCV) which involves use of scan rates in excess of 100V/s. The main drawback of this process is high background currents due to the double layer capacitance at the electrode/electrolyte interface. Thus, background subtracted FSCV at 300V/s was used to record CVs for dopamine detection by varying the anodic potential limit from 0.8V to 1.4V with a holding potential of −1V.

The anodic sweeps for the four potential scan windows; A -1V to +0.8V, B -1V to +1.0V, C -1V to +1.2V and D -1V to +1.4V, showed a close overlap. The only distinction was the appearance of a second peak or wave at potentials > +1.0V, i.e., in case of scan windows C and D. The presence of the first peak can be explained by the phenomenon of

surface adsorption due to pre-concentration at -1V. At neutral pH, dopamine exists as a cation and is adsorbed at negative holding potentials due to electrostatic forces of attraction. When a potential sweep is applied, the adsorbed species get oxidized first resulting in a current peak. The second peak or wave appears due to diffusion limited mass transport of dopamine. Distinction between the two peaks depends on the extent of surface adsorption. In cases where a less negative holding potential are used, the signals due to adsorption and diffusion coalesce into a single current peak.

An average sensitivity value of 115μA/cm^2.μM was recorded using FSCV which is nearly 400*x* than that observed for S_1 at slower scan rates, thus highlighting the benefits of this technique. Also, in case of $UMEA_1$, no enhancement in the signal was observed as the anodic potential limit was increased from +0.8V to +1.4V unlike that observed in case of other carbon based electrodes like carbon fibers. Signal due to the Leucodopaminechrome/ Dopaminechrome redox couple observed in case of S_1 at slower scan rates is not seen in these experiments because the transformation of dopamine-o-quinone to leucodopaminechrome has very slow reaction kinetics which is suppressed by the use of very high scan rates.

All these results clearly demonstrate the superior sensitivity of FSCV technique for DA detection and that nanodiamond UMEA provides a very stable platform as there is no change in the nanodiamond surface chemistry and/or microstructure.

5.1.5 Columnar Nanodiamond UMEA

Despite the successful detection of bio-analytes using planar nanodiamond UMEAs, there were still some drawbacks arising from the fabrication process. The bottom up approach required filling in of the $Mo/SiO_2/Si$ molds with nanodiamond resulting in UMEs with a donut profile. This occurred due to differential nanodiamond growth rates at the base and the side-walls/periphery of the molds owing to dissimilar surface roughness. The final UME dimensions would always be larger than that originally designed and could not be controlled accurately. The nanodiamond microstructure also showed minor variations between the different planar UMEAs. The last fabrication step consisting of molybdenum lift-off was difficult due to formation of carbide during the MPECVD process. These issues prompted successful design and fabrication of columnar nanodiamond UMEA labeled as $\mathbf{UMEA_{RIE}}$.

Planar nanodiamond film was grown on a silicon substrate with a ridge like microstructure similar to S_1, followed by sputtering of 0.5µm aluminum film which acts as a sacrificial mask layer. Conventional UV photolithography was used to delineate the array layout followed by a RIE process to dry etch the exposed nanodiamond film using a STS-AOE ICP machine thus creating nanodiamond columns under the Al mask. A liquid spin-on-glass was applied and cured to create an insulating matrix followed by Al lift-off. This process was used to fabricate a 50x50 UMEA with 9µm diameter of each UME and 100µm spacing. The height of each columnar UME was ~ 2µm with an estimated thickness of ~ 0.35µm-0.40µm of the dielectric matrix at its thinnest.

$UMEA_{RIE}$ exhibited steady state response consistent with hemispherical diffusion for detection of ferrocyanide in 0.1M KCl and DA in 0.1M PBS. The equivalent radius of

3.6μm was comparable to that calculated for $UMEA_2$. Consequently, the electrochemical results in terms of sensitivity showed a close match. The linear calibration plots yielded sensitivity value of 2.0396mA/cm^2.mM for ferrocyanide detection, nearly 24*x* than that recorded for the macroelectrode S_1 while that for DA was 2.7μA/cm^2.μM, a 9*x* enhancement over S_1.

These results confirm that the new fabrication process for columnar nanodiamond UMEAs can still achieve excellent sensitivity for DA detection while overcoming the drawbacks encountered in case of the planar UMEAs. No surface modifications and/or functionalization were required in these experiments.

5.2 Recommendations for future work

Nitrogen-incorporated nanodiamond has demonstrated excellent properties making it suitable for application as an electrode material, be it in the form of a macroelectrode or an UMEA. There are a lot of possibilities for future work based on the information gleaned from this research. Some recommendations for future work include:

a) The electrochemical technique focused on in this work is cyclic voltammetry. Despite its advantages of providing rapid qualitative and quantitative information, the sensitivity and detection limits achievable are not the best. Alternative techniques such as differential pulse voltammetry for identification and quantification can be examined. Amperometry can be used for monitoring analyte concentrations with respect to time and changes in concentrations due to the same specie or an interferant can also be quantified.

b) The sensitivity of nanodiamond increased with reduction in the electrode dimensions as it is inversely proportional to r^2. So far, the smallest dimension achieved in this work is about 3.6μm. Fabrication and characterization of nanodiamond UMEAs with micron and sub-micron dimensions should yield interesting results.

c) In-vitro applications require electrodes with high aspect ratio, e.g. microprobes, in order to minimize tissue damage and achieve high spatial resolution. A new microprobe with a narrow form-factor should be designed and fabricated which incorporates individually addressable nanodiamond UMEAs in order to achieve high spatial resolution and also functionality, e.g., use 2 adjacent UMEs, one for stimulating neurotransmitter release and its neighbor for detection.

d) Electrochemically inactive neurotransmitters such as choline, acetylcholine, glutamate, GABA and compound such as glucose cannot be detected by direct electrochemical measurements. These biomolecules require surface modification such as immobilization of an enzymatic layer which can catalyze the reactions to enable indirect measurement of those analytes. This approach can be used to evaluate nanodiamond performance in detecting such bio-analytes.

e) Application of nanodiamond UMEAs and macroelectrodes in areas other than electroanalysis such as water treatment, organic and inorganic electrosynthesis and electrochemical energy storage technology can be examined.

PUBLICATIONS

1. Supil Raina, W. P. Kang, J. L. Davidson, A. B. Bonds, D. E. Cliffel, M. Howell. "A novel "coral" carbon microprobe with and without N_2 incorporation." *Diamond and Related Materials* 15 (2006): 1844-1848.

2. Supil Raina, W. P. Kang, J. L. Davidson. "Field emission from nanodiamond grown with 'ridge' type geometrically enhanced features." *Diamond and Related Materials* 17 (2008): 790-793.

3. Supil Raina, W. P. Kang, J. L. Davidson. "Nanodiamond film with 'ridge' surface profile for chemical sensing." *Diamond and Related Materials* 17 (2008): 896-899.

4. Supil Raina, W. P. Kang, and J. L. Davidson. "Nitrogen incorporated nanodiamond film with 'ridge' surface morphology for detection of bio-analyte." *Diamond and Related Materials* 18 (2009): 574-577.

5. Supil Raina, W. P. Kang, and J. L. Davidson. "Optimizing nitrogen incorporation in nanodiamond film for bio-analyte sensing." *Diamond and Related Materials* 18 (2009): 718-721.

6. Supil Raina, X. C. LeQuan, W. P. Kang, and J. L. Davidson. "Effect of Nitrogen Concentration on Nanodiamond Film Characteristics for Electrode Application." *ECS Transactions* 19, no. 21 (2009): 23-35.

7. Y. M. Wong, W. P. Kang, J. L. Davidson, Supil Raina, and J. H. Huang. "Carbon nanostructures as thermal field emitters for waste heat recovery." *Diamond and Related Materials* 18 (2009): 563-566.

8. Supil Raina, W. P. Kang, and J. L. Davidson. "Nanodiamond macro- and microelectrode array bio-sensor." *Sensors* (2009):1780-1783.
9. Supil Raina, W. P. Kang, and J. L. Davidson. "Fabrication of nitrogen-incorporated nanodiamond ultra-microelectrode array for Dopamine detection." *Diamond and Related Materials* 19 (2010): 256-259.

10. Supil Raina, W. P. Kang, J. L. Davidson, and J. H. Huang. "Electrochemical Biosensor Utilizing Nitrogen Incorporated Nanodiamond Ultra-Microelectrode Array." *ECS Transactions* 28, no. 34 (2010): 21-28.

11. N. Ghosh, W. P. Kang, J. L. Davidson, and Supil Raina. "Enhanced electron-field emission from nanodiamond ridge-structured emission arrays capped on micropatterned silicon pillars." *Journal of Vacuum Science and Technology B* 28, no.5 (2010): 1016-1019.

12. N. Ghosh, W. P. Kang, J. L. Davidson, and Supil Raina. “The effect of ballast-resistor and field-screening on electron-emission from nanodiamond emitters fabricated on micropatterned silicon pillar arrays.” *Journal of Vacuum Science and Technology B*, submitted.

APPENDIX A

PROPOSED REACTION PATHWAY FOR UA OXIDATION

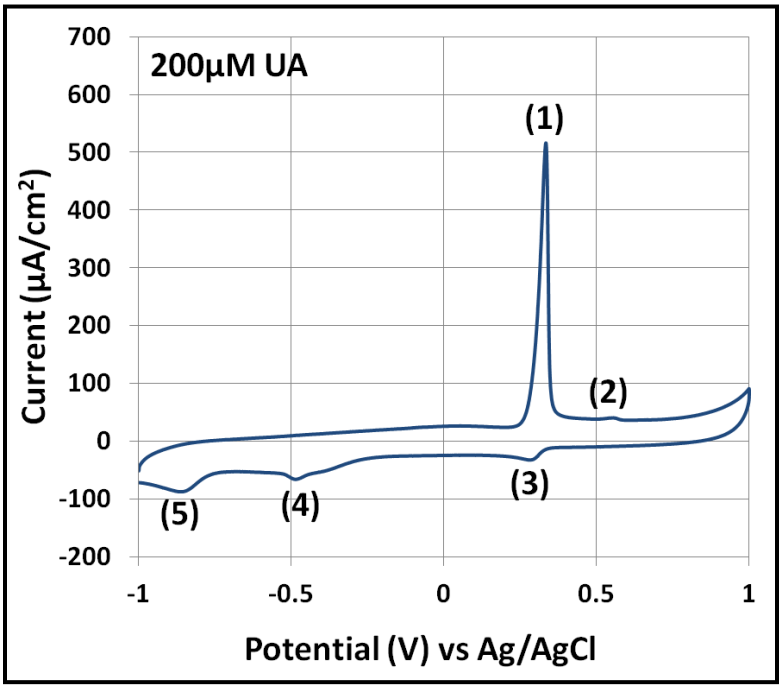

Figure A. 1 CV recorded for 200µM UA in 0.1M PBS at 100mV/s.

Cyclic voltammogram recorded from macroelectrode S_1 using a 200µM solution of UA in 0.1M PBS at 100mV/s can be seen in figure A.1. From this data, one can identify 2 oxidation peaks and 3 reduction peaks suggesting a complex set of reactions downstream of UA oxidation. The proposed reaction pathway for electrochemical oxidation of UA has been elucidated in figure A.2. The roman numerals in the parentheses correspond to the chemicals depicted in figure A.2.

UA (I) can be oxidized to form a diimine quinonoid (II) along with transfer of two electrons and two protons. The **peak 1**, at around 0.331V, can be assigned to this oxidation step with the **peak 3** at around 0.281V, being assigned to the reduction step on

the reverse sweep. A ΔE_p value of 54mV suggests a quasi-reversible redox process with fast electron transfer kinetics. This product is unstable and at slow scan rates, undergoes a hydration reaction to form an imine alcohol (III) which is a more stable intermediate. The imine alcohol (III) can follow two paths depending on the reaction conditions. At slower scan rates, it can undergo an irreversible 2 e^- and $2H^+$ reduction and regenerate UA (I) after a dehydration step, which is responsible for **peak 5**.

The other sequence includes formation of BCA (V) by ring contraction followed by hydration to form HDC (VII). Allantoin (VIII) is produced from HDC (VII) after ring opening and decarboxylation. BCA (V) also undergoes a $2e^-$ and $2H^+$ reduction to form a bi-cyclic carboxylic acid (VI) which contributes to the signal at **peak 5**. In these experiments, peak 5 increased in height with increase in UA concentration, but the peak position shifted towards more negative potential. This would suggest very sluggish reaction kinetics. In addition, BCA (V) undergoes reversible deprotonation producing the carboxylate ion (IX) which can be oxidized to a bi-cyclic alcohol (X) along with the transfer of $2e^-$ and $2H^+$. This results in the oxidation **peak 2** seen in figure A.1. This alcohol (IX) or its tautomer (XII) can be reduced to form allantoin (VIII), both the reduction steps contributing to **peak 4** [126-128]. These secondary reactions can be suppressed by using fast scan rates which thus leaves just peak 1 and peak 3 in the CV plot. The IUPAC names of these chemicals are included in the figure A.2 caption.

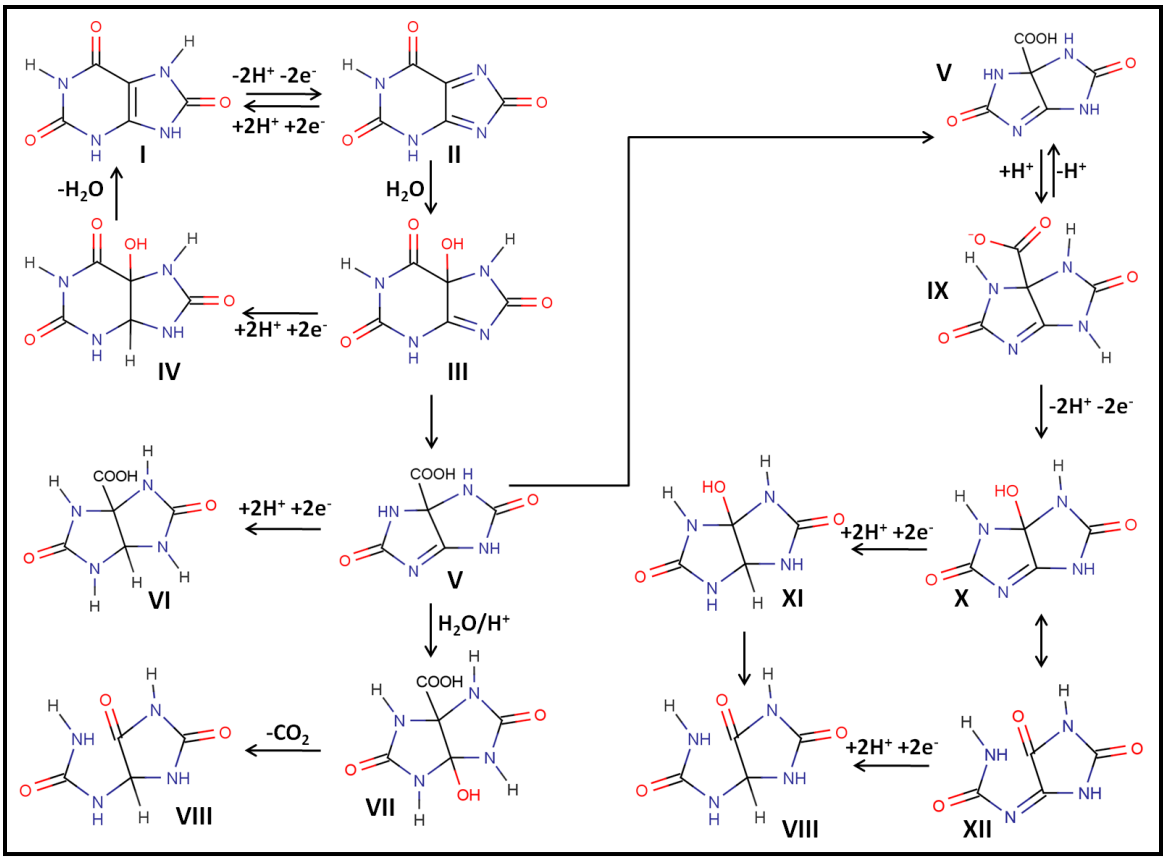

Figure A. 2 Proposed reaction pathway of UA oxidation [126-128].

The chemical structures and their IUPAC names were derived using a Java based program available on a chemical supplies company website.
http://www.molport.com/buy-chemicals/find-chemicals.

I- 2,3,6,7,8,9-hexahydro-1H-purine-2,6,8-trione or UA.
II- 2,3,6,8-tetrahydro-1H-purine-2,6,8-trione.
III- 5-hydroxy-2,3,5,6,7,8-hexahydro-1H-purine-2,6,8-trione.
IV- 5-hydroxy-octahydro-1H-purine-2,6,8-trione.
V- 2,5-dioxo-octahydroimidazo[4,5-d]imidazolidine-3a-carboxylic acid or BCA.
VI- 2,5-dioxo-1H,2H,3H,3aH,4H,5H-imidazo[4,5-d]imidazolidine-3a-carboxylic acid,
VII- 6a-hydroxy-2,5-dioxo-octahydroimidazo[4,5-d]imidazolidine-3a-carboxylic acid or HDA.
VIII- (2,5-dioxoimidazolidin-4-yl)urea or Allantoin.
IX- 2,5-dioxo-1H,2H,3H,3aH,4H,5H-imidazo[4,5-d]imidazolidine-3a-carboxylate.
X- 3a-hydroxy-1H,2H,3H,3aH,4H,5H-imidazo[4,5-d]imidazolidine-2,5-dione.
XI- 3a-hydroxy-octahydroimidazo[4,5-d]imidazolidine-2,5-dione.
XII- [(4E)-2,5-dioxoimidazolidin-4-ylidene]urea.

APPENDIX B

ELECTROCHEMICAL SENSING PERFORMANCE

Table B. 1 Electrochemical detection of ferrocyanide.

Electrode	Analyte	Technique	Sensitivity ($mA/cm^2.mM$)	Linear Dynamic Range
BDD film[71]	Ferrocyanide	CV	0.0847	0.25mM-4.9mM
BDD UMEA[71]	Ferrocyanide	CV	0.4576	0.25mM-4.9mM
BDD UMEA[152]	Ferrocyanide	CV	0.693	0.05mM-4.9mM
Nanodiamond powder electrode[153]	Ferrocyanide	CV	0.1476	1mM-20mM
BDD UMEA[72]	Ferrocyanide	CV	0.6364	0.05mM-4.9mM
BDD microelectrode[142]	Ferrocyanide	CV	1.33	0.2µM-1.2µM
THIS WORK				
Nanodiamond film S_1	Ferrocyanide	CV	0.0852	1mM-10mM
Nanodiamond $UMEA_1$	Ferrocyanide	CV	1.145	1mM-8mM
Nanodiamond $UMEA_2$	Ferrocyanide	CV	1.986	1mM-8mM
Nanodiamond $UMEA_3$	Ferrocyanide	CV	1.311	1mM-8mM
Nanodiamond $UMEA_{RIE}$	Ferrocyanide	CV	2.0396	1mM-8mM

Table B. 2 Electrochemical detection of dopamine

Electrode	Analyte	Technique	Sensitivity ($\mu A/cm^2.\mu M$)	Linear dynamic range	LOD
Carbon ceramic electrode[154]	DA	CV	0.028	100µM -800µM	-
Oxidized BDD Film[155]	DA	CA	0.46557	5µM-120µM	1.5µM
Oxidized BDD[156]	DA	CA	0.725	0.1µM-1µM	50nM
BDD Nanograss Array[155]	DA	CA	0.64214	5µM-120µM	0.8µM
Ceramic Based UMEA[157] Uncoated→ Nafion Coated→	DA	CA	0.126 0.164	-	0.267µM 0.225µM
BDD UMEA[72]	DA	CV	2.19	20µM-1000µM	-
Oxidized BDD[156]	DA in presence of 0.1M AA	CA	0.45	0.1µM-1µM	50nM
Tyrosine modified boron doped diamond film[158]	DA in presence of 1mM AA	CA	0.0686	5µM-120µM	-
4-pentenoic acid modified boron doped diamond[159]	DA in presence of 200µM AA	CA	0.55	1µM-10µM	-
		DPV	1.42	1µM-10µM	-
THIS WORK					
Nanodiamond film S_1	DA	CV	0.3	100µM-1000µM	3.6µM
Nanodiamond film S_1	DA in presence of 1mM AA+ 1mM UA	CV	0.25	100µM-1000µM	4.1µM
Nanodiamond $UMEA_1$	DA	CV	1.8	100µM-1000µM	-
Nanodiamond $UMEA_1$	DA in presence of 1mM AA	CV	1.2	100µM-1000µM	-
Nanodiamond $UMEA_1$	AA	CV	0.99	100µM-1000µM	-
Nanodiamond $UMEA_1$	UA	CV	1.3	100µM-1000µM	-
Nanodiamond $UMEA_2$	DA	CV	2.6	100µM-1000µM	-
Nanodiamond $UMEA_3$	DA	CV	1.8	100µM-1000µM	-
Nanodiamond $UMEA_{RIE}$	DA	CV	2.7	100µM-1000µM	-
Nanodiamond $UMEA_{RIE}$	DA	FSCV	115	100µM-1000µM	-

.

REFERENCES

1. Swain, Greg M. . "Solid Electrode Materials: Pretreatment and Activation." In *Handbook of Electrochemistry*. Edited by Cynthia G. Zoski. Amsterdam: Elsevier, 2007. 111-153.

2. Rao, Tata N., Akira Fujishima, and John C. Angus. "Historical Survey of Diamond Electrodes." In *Diamond Electrochemistry*. Edited by A. Fujishima, et.al.. UK: Elsevier Science, 2005. 1-10.

3. Swain, Greg M.. "Electroanalytical Applications of Diamond Electrodes." In *Thin Film Diamond II*. Edited by C. Nebel, J. Ristein. New York: Elsevier, 2004. 121-148.

4. Bard, Allen J., and Larry R. Faulkner. "Potential Sweep Methods." In *Electrochemical Methods: Fundamentals and Applications*. 2 ed. New York, NY: Wiley, 2001. 226-260.

5. Wang, Joseph. "Study of Electrode Reactions." In *Analytical Electrochemistry*. 2 ed. New York: Wiley-VCH, 2001. 28-59.

6. Bard, Allen J., and Larry R. Faulkner. "Basic Potential Step Methods." In *Electrochemical Methods: Fundamentals and Applications*. 2nd ed. New York: Wiley, 2001. 156-225.

7. Forster, Robert J., and Tia E. Keyes. "Behavior of Ultramicroelectrodes." In *Handbook of Electrochemistry*. Edited by Cynthia G. Zoski. Amsterdam: Elsevier, 2007. 155-171.

8. Wang, Joseph. "Practical Considerations." In *Analytical Electrochemistry*. New York: Wiley-VCH, 2001. 100-139.

9. Pierson, Hugh O.. "Structure and Properties of Diamond and Diamond Polytypes." In *Handbook of Carbon, Graphite, Diamond and Fullerenes: Properties, Processing and Applications*. New Jersey: Noyes Publications, 1993. 244-277.

10. Yoder, Max N.. "Diamond Properties and Applications." In *Diamond Films and Coatings*. Edited by Robert F. Davis. New Jersey: Noyes Publications, 1993. 1-30.

11. Sque, Steve. "Structure of Diamond." Physics at Exeter. http://newton.ex.ac.uk/research/qsystems/people/sque/diamond/structure/ (accessed January 15, 2010).

12. Ramdas, A. K.. "Optical, Mechanical and Transport Properties." In *Properties, Growth and Applications of Diamond*. Edited by M. H. Nazare and A. J. Neves. London: INSPEC, 2001. 1- 244.

13. Pleskov, Y. V et. al.. "Photoelectrochemical properties of semiconductor diamond ." *Journal of Electroanalytical Chemistry* 228, no. 1-2 (1987): 19-27.

14. Kraft, Alexander. "Doped Diamond: A Compact Review on a New, Versatile Electrode Material." *International Journal of Electrochemical Science* 2 (2007): 355-385.

15. Xu, J., and G. M. Swain. "Oxidation of Azide Anion at Boron-Doped Diamond Thin-Film Electrodes." *Analytical Chemistry* 70 (1998): 1502-1510.

16. Swain, G. M., and R. Ramesham. "The Electrochemical Activity of Boron-Doped Polycrystalline Diamond Thin Film Electrodes." *Analytical Chemistry* 65 (1993): 345-351.

17. Fujishima, A., Y. Einaga, T. N. Rao, and D. A. Tryk. "Fundamental and Applied Aspects of Diamond Electrodes." In *Diamond Electrochemistry*. Edited by A. Fujishima, et.al. UK: Elsevier Science, 2005. 556- 574.

18. Yano, T., D. A. Tryk, K. Hashimoto, and A. Fujishima. "Electrochemical Behavior of Highly Conductive Boron-Doped Diamond Electrodes for Oxygen Reduction in Alkaline Solution." *Journal of Electrochemical Society* 145, no. 6 (1998): 1870-1876.

19. Rao, T. N., I. Yagi, D. A. Tryk, and A. Fujishima. "Electrochemical Oxidation of NADH at Highly Boron-Doped Diamond Electrodes." *Analytical Chemistry* 71 (1999): 2506-2511.

20. Sarada, B. V., T. N. Rao, D. A. Tryk, and A. Fujishima. "Electrochemical Oxidation of Histamine and Serotonin at Highly Boron-Doped Diamond Electrodes." *Analytical Chemistry* 72 (2000): 1632-1638.

21. Raina, Supil, W. P. Kang, and J. L. Davidson. "Nitrogen incorporated nanodiamond film with ‘ridge’ surface morphology for detection of bio-analyte." *Diamond and Related Materials* 18 (2009): 574-577.

22. Kraft, A., M. Stadelmann, and M. Blaschke. "Anodic oxidation with doped diamond electrodes: a new advanced oxidation process." *Journal of Hazardous Materials* 103, no. 3 (2003): 247-261.

23. Comninellis, C., M. M. Chowdhry, and L. Quattara. "Electrochemical Treatment of Industrial Wastewater." *New Diamond and Frontier Carbon Technology* 14 (2004): 239-247.

24. Faouzi, M., et. al.. "Electrochemical degradation of anthraquinone dye Alizarin Red S by anodic oxidation on boron-doped diamond." *Dyes and Pigments* 73 (2007): 86-89.

25. Reuben, C. et. al.. "Efficient reduction of nitrite and nitrate to ammonia using thin-film B-doped diamond electrodes." *Journal of Electroanalytical Chemistry* 396 (1995): 233-239.

26. Wurm, J.. "Use of Diamond-Coated Anodes in Electroplating and for Treating Electroplating Waste Solutions." *New Diamond and Frontier Carbon Technology* 12 (2002): 107-114.

27. Andel, Y. Van, and L. J. J. Janssen. "Electrochemical regeneration of chrome etching solution ." *Journal of Applied Electrochemistry* 32 (2002): 481-486.

28. Arihara, K., C. Terashima, and A. Fujishima. "Application of Freestanding Perforated Diamond Electrodes for Efficient Ozone-Water Production ." *Electrochemical and Solid State Letters* 9, no. 8 (2006): D17-D20.

29. Kraft, A., M. Stadelmann, M. Weunsche, and M. Blanschke. "Electrochemical ozone production using diamond anodes and a solid polymer electrolyte." *Electrochemistry Communications* 8, no. 5 (2006): 883-886.

30. Lee, J., Y. Einaga, A. Fujishima, and S. Park. "Electrochemical Oxidation of Mn2+ on Boron-Doped Diamond Electrodes with Bi3+ Used as an Electron Transfer Mediator ." *Journal of Electrochemical Society* 151 (2004): E265.

31. Honda, K. et. al.. "Electrochemical Characterization of the Nanoporous Honeycomb Diamond Electrode as an Electrical Double-Layer Capacitor ." *Journal of Electrochemical Society* 147 (2000): 659-664.

32. Honda, K. et. al.. "Electrochemical Characterization of Carbon Nanotube/Nanohoneycomb Diamond Composite Electrodes for a Hybrid Anode of Li-Ion Battery and Super Capacitor." *Journal of Electrochemical Society* 151, no. 4 (2004): A532-A541.

33. Szunerits, S. , and L. Thouin. "Microelectrode Arrays." *Handbook of Electrochemistry*. Edited by Cynthia G. Zoski. Amsterdam: Elsevier, 2007. 391-428.

34. Bard, A. J., and L. R. Faulkner. "Basic Potential Step Methods." *Electrochemical Methods: Fundamentals and Applications*. 2nd ed. New York: Wiley, 2001. 156-225.

35. Huffman, M. L., and B. J. Venton. "Carbon-fiber microelectrodes for in vivo applications." *Analyst* 134 (2009): 18-24.

36. Michael, A. C., and R. M. Wightman. "Microelectrodes." In *Laboratory Techniques in Electroanalytical Chemistry*. Edited by P. T. Kissinger and W. R. Heineman. New York: Marcel Dekker, Inc., 1996. 367- 402.

37. Ewing, A. G., M. A. Dayton, and R. M. Wightman. "Pulse Voltammetry with Microvoltammetric Electrodes." *Analytical Chemistry* 53 (1981): 1842-1847.

38. Olivia, H., B. V. Sarada, T. N. Rao, and A. Fujishima. "Diamond Microelectrodes." In *Diamond Electrochemistry*. Edited by A. Fujishima, et.al. UK: Elsevier Science, 2005. 396-413.

39. Heien, M. L. A. V. et. al.. "Overoxidation of carbon-fiber microelectrodes enhances dopamine adsorption and increases sensitivity." *Analyst* 128 (2003): 1413-1419.

40. Hashemi, P. et. al.. "Voltammetric Detection of 5-Hydroxytryptamine Release in the Rat Brain." *Analytical Chemistry* 81 (2009): 9462-9471.

41. Strand, A. M., and B. J. Venton. "Flame Etching Enhances the Sensitivity of Carbon-Fiber Microelectrodes." *Analytical Chemistry* 80, no. 10 (2008): 3708-3715.

42. Zhang, M. et. al.. "Carbon Nanotube-Modified Carbon Fiber Microelectrodes for In Vivo Voltammetric Measurement of Ascorbic Acid in Rat Brain." *Analytical Chemistry* 79, no. 17 (2007): 6559-6565.

43. Ferreira, Nuno R. et. al.. "Electrochemical measurement of endogenously produced nitric oxide in brain slices using Nafion/o-phenylenediamine modified carbon fiber microelectrodes." *Analytica Chimica Acta* 535 (2005): 1-7.

44. Zhang, B. et. al.. "Spatially and Temporally Resolved Single-Cell Exocytosis Utilizing Individually Addressable Carbon Microelectrode Arrays." *Analytical Chemistry* 80, no. 5 (2008): 1394-1400.

45. Liu, J. et. al.. "Detection of Hydrazine, Methylhydrazine, and Isoniazid by Capillary Electrophoresis with a Palladium-Modified Microdisk Array Electrode." *Analytical Chemistry* 68 (1996): 3350-3353.

46. Fletcher, Stephen, and Michael David Horne. "Random assemblies of microelectrodes (RAM™ electrodes) for electrochemical studies ." *Electrochemistry Communications* 1, no. 10 (1999): 502-512.

47. Cheng, I. Francis, Lisa D. Whiteley, and Charles R. Martin. "Ultramicroelectrode ensembles. Comparison of experimental and theoretical responses and evaluation of electroanalytical detection limits." *Analytical Chemistry* 61, no. 7 (1989): 762-766.

48. Cheng, I. Francis, and Charles R. Martin. "Ultramicrodisk electrode ensembles prepared by incorporating carbon paste into a microporous host membrane." *Analytical Chemistry* 60, no. 19 (1988): 2163-2165.

49. O'Hare, Danny, Julie V. Macpherson, and Alison Willowa. "On the microelectrode behaviour of graphite–epoxy composite electrodes ." *Electrochemistry Communications* 4, no. 3 (2002): 245-250.

50. Jin, Wenrui, Qiangfeng Weng, and Jianren Wu. "Determination of bovine serum albumin by capillary zone electrophoresis with end-column amperometric detection at the carbon fiber microdisk array electrode ." *Analytica Chimica Acta* 342, no. 1 (1997): 67-74.

51. Jin, Wenrui, Huiying Wei, and Xin Zhao. "Determination of adenine and guanine by capillary zone electrophoresis with end-column amperometric detection at a carbon fiber microdisk array electrode." *Electroanalysis* 9, no. 10 (1997): 770-774.

52. Zachek, Matthew K. et. al.. "Simultaneous Decoupled Detection of Dopamine and Oxygen Using Pyrolyzed Carbon Microarrays and Fast-Scan Cyclic Voltammetry." *Analytical Chemistry* 81, no. 15 (2009): 6258-6265.

53. Yan, Jie et. al.. "An electrochemical sensor for 3,4-dihydroxyphenylacetic acid with carbon nanotubes as electronic transducer and synthetic cyclophane as recognition element ." *Chemical Communications* (2008): 4330-4332.

54. Xu, Han et. al.. "Carbon post-microarrays for glucose sensors ." *Biosensors and Bioelectronics* 23, no. 11 (2008): 1637-1644.

55. Fiaccabrino, G. C., X. M. Tang, N. Skinner, N. F. de Rooij, and M. Koudelka-Hep. "Analytica Chimica Acta." *Electrochemical characterization of thin-film carbon interdigitated electrode arrays* 326 (1996): 155-161.

56. Wu, H. P.. "Fabrication and Characterization of a New Class of Microelectrode Arrays Exhibiting Steady-State Current Behavior." *Analytical Chemistry* 65 (1993): 1643-1646.

57. Lee, Chong-Yong, Yong-Jun Tan, and Alan M. Bond. "Identification of Surface Heterogeneity Effects in Cyclic Voltammograms Derived from Analysis of an Individually Addressable Gold Array Electrode." *Analytical Chemistry* 80, no. 10 (2008): 3873-3881.

58. Szunerits, S., and D. R. Walt. "Fabrication of an Optoelectrochemical Microring Array." *Analytical Chemistry* 74, no. 7 (2002): 1718-1723.

59. Cui, Hui-Fang, Jian-Shan Ye, Y. Chen, Ser-Choong Chong, and Fwu-Shan Sheu. "Microelectrode Array Biochip: Tool for In Vitro Drug Screening Based on the Detection of a Drug Effect on Dopamine Release from PC12 Cells." *Analytical Chemistry* 78, no. 18 (2006): 6347-6355.

60. Cui, Hui-Fang et. al.. "In situ temporal detection of dopamine exocytosis from l-dopa-incubated MN9D cells using microelectrode array-integrated biochip ." *Sensors and Actuators B: Chemical* 115, no. 2 (2006): 634-641.

61. Pai, R. S. et. al.. "Fully Integrated Three-Dimensional Electrodes for Electrochemical Detection in Microchips: Fabrication, Characterization, and Applications." *Analytical Chemistry* 81, no. 12 (2009): 4762-4769.

62. Robinson, D. L., A. Hermans, A. T. Seipel, and R. M. Wightman. "Monitoring Rapid Chemical Communication in the Brain." *Chemical Reviews* 108 (2008): 2554-2584.

63. Orozco, J., C. Fernandez-Sanchez, and C. Jimenez-Jorquera. "Ultramicroelectrode Array Based Sensors: A Promising Analytical Tool for Environmental Monitoring." *Sensors* 10 (2010): 475-490.

64. Huang, X., A. M. O'Mahony, and R. G. Compton. "Microelectrode Arrays for Electrochemistry: Approaches to Fabrication." *Small* 5, no. 7 (2009): 776-788.

65. Tsunozaki, K. , Y. Einaga, T. N. Rao, and A. Fujishima. "Fabrication and Electrochemical Characterization of Boron-Doped Diamond Microdisc Array Electrodes." *Chemistry Letters* 31, no. 5 (2002): 502-503.

66. Provent, C., W. Haenni, E. Santoli, and P. Rychen. "Boron-doped diamond electrodes and microelectrode-arrays for the measurement of sulfate and peroxodisulfate." *Electrochimica Acta* 49 (2004): 3737-3744.

67. Lawrence, N. S. et. al.. "Electroanalytical applications of boron-doped diamond microelectrode arrays ." *Talanta* 69, no. 4 (2006): 829-834.

68. Madore, C., A. Duret, W, Haenni, and A. Perret. "Detection of Trace Silver and Copper at an Array of Boron- Doped Diamond Microdisk Electrodes." *Electrochemical Society Proceedings (Microfabricated Systems and MEMS IV)* 19 (2000): 159-168.

69. Pagels, M. et. al.. "All-Diamond Microelectrode Array Device." *Analytical Chemistry* 77, no. 11 (2005): 3705-3708.

70. Simm, A. O. et. al.. "Boron-doped diamond microdisc arrays: electrochemical characterisation and their use as a substrate for the production of microelectrode arrays of diverse metals (Ag, Au, Cu) via electrodeposition." *The Analyst* 130 (2005): 1303-1311.

71. Soh, K. L. et. al.. "Diamond-derived microelectrodes array for electrochemical analysis." *Diamond and Related Materials* 13 (2004): 2009-2015.

72. Soh, K. L. et. al. . "Diamond-derived ultramicroelectrodes designed for electrochemical analysis and bioanalyte sensing." *Diamond and Related Materials* 17 (2008): 900-905.

73. Carabelli, V. et. al.. "Nanocrystalline diamond microelectrode arrays fabricated on sapphire technology for high-time resolution of quantal catecholamine secretion from chromaffin cells ." *Biosensors and Bioelectronics* 26, no. 1 (2010): 92-98.

74. Michael, A. C., and L. M. Borland. "An Introduction to Electrochemical Methods in Neuroscience." In *Electrochemical Methods for Neuroscience*. Edited by A. C. Michael and L. M. Borland. Boca Raton, Florida: CRC Press, 2007. 1-16.

75. Kuhar, M. J., K. Minneman, and E. C. Mully. "Catecholamines." In *Basic Neurochemistry: Molecular, Cellular, and Medical Aspects*. 7th ed. Edited by G. J Siegel, R. W. Albers, S. T. Brady and D. L. Price. Canada: Elsevier Academic Press, 2006. 211-226.

76. Venton, B. J., and R. M. Wightman. "Psychoanalytical Chemistry: Dopamine and Behavior." *Analytical Chemistry* 75, no. 19 (2003): 414A-421A.

77. Eisenhofer, G., T. Huynh, M. Hiroi, and K. Pacak. "Understanding Catecholamine Metabolism as a Guide to the Biochemical Diagnosis of Pheochromocytoma." *Reviews in endocrine & metabolic disorders* 2, no. 3 (2001): 297-311.

78. Wild, G. C., and E. C. Benzel. "Catecholamine Neurotransmitters." In *Essentials of Neurochemistry*. Boston: Jones and Bartlett Publishers, 1994. 58-66.

79. Hermann, N., K. L. Lanctot, and L. R. Khan. "The Role of Norepinephrine in the Behavioral and Psychological Symptoms of Dementia ." *Journal of Neuropsychiatry and Clinical Neurosciences* 16 (2004): 261-276.

80. Sircar, S.. *Principles of Medical Physiology* . Stuttgart: Thieme, 2008.

81. Sherwood, L. . *Human Physiology: From Cells to Systems* . Canada : Cengage Learning, 2010.

82. Li, Q., C. Batchelor-McAuley, and R. G. Compton. "Electrooxidative Decarboxylation of Vanillylmandelic Acid: Voltammetric Differentiation between the Structurally Related Compounds Homovanillic Acid and Vanillylmandelic Acid." *Journal of Physical Chemistry* 114, no. 29 (2010): 9713-9719.

83. Peaston, R. T. et. al.. "Performance of plasma free metanephrines measured by liquid chromatography–tandem mass spectrometry in the diagnosis of pheochromocytoma." *Clinica Chimica Acta* 411, no. 7-8 (2010): 546-552.

84. Rebec, G. V.. "From Interferant Anion to Neuromodulator: Ascorbate Oxidizes its Way to Respectability." In *Electrochemical Methods for Neuroscience*. Edited by A. C. Michael and L. M. Borland. Boca Raton, Florida: CRC Press, 2007. 149-166.

85. Liu, A. et. al.. "Simultaneous voltammetric determination of norepinephrine, ascorbic acid and uric acid on polycalconcarboxylic acid modified glassy carbon electrode." *Biosensors and Bioelectronics* 23 (2008): 1488-1495.

86. Huang, S., H. Liao, and D. Chen. "Simultaneous determination of norepinephrine, uric acid, and ascorbic acid at a screen printed carbon electrode modified with polyacrylic acid-coated multi-wall carbon nanotubes ." *Biosensors and Bioelectroncis* 25, no. 10 (2010): 2351-2355.

87. Mazloum-Ardakani, M. et. al.. "Electrochemical and catalytic investigations of dopamine and uric acid by modified carbon nanotube paste electrode." *Bioelectrochemistry* 75 (2009): 1-8.

88. Hasoň, S., V. Vetterl, F. Jelen, and M. Fojta. "Improved sensitivity and selectivity of uric acid voltammetric sensing with mechanically grinded carbon/graphite electrodes." *Electrochimica Acta* 54 (2009): 1864-1873.

89. Ciolkowski, E. L. et. al.. "Disproportionation During Electrooxidation of Catecholamines at Carbon-Fiber Microelectrodes." *Analytical Chemistry* 66 (1994): 3611-3617.

90. Mo, J., and B. Ogorevc. "Simultaneous Measurement of Dopamine and Ascorbate at Their Physiological Levels Using Voltammetric Microprobe Based on Overoxidized Poly(1,2-phenylenediamine)-Coated Carbon Fiber." *Analytical Chemistry* 73 (2001): 1196-1202.

91. Ciszewski, A., and G. Milczarek. "Polyeugenol-Modified Platinum Electrode for Selective Detection of Dopamine in the Presence of Ascorbic Acid." *Analytical Chemistry* 71, no. 5 (1999): 1055-1061.

92. Safavi, A., N. Maleki, O. Moradlou, and F. Tajabadi. "Simultaneous determination of dopamine, ascorbic acid, and uric acid using carbon ionic liquid electrode." *Analytical Biochemistry* 359 (2006): 224-229.

93. Pachla, L. A., D. L. Reynolds, D. S. Wright, and P. T. Kissinger. "Analytical methods for measuring uric acid in biological samples and food products." *Journal - Association of Official Analytical Chemists* 70 (1987): 1-14.

94. Grove, R. A., R. Bildfell, C. J. Henny, and D. R. Buhler. "Bilateral Uric Acid Nephrolithiasis and Ureteral Hypertrophy in a Free-ranging River Otter (Lontra canadensis)." *Journal of Wildlife Diseases* 39, no. 4 (2003): 914-917.

95. Flag, L., and R. Roederscheimer. "Renal Calculi." In *Food and Nutrients in Disease Management*. Edited by Ingrid Kohlstadt. Boca Raton, Florida: CRC Press, 2009. 337-350.

96. Stapleton, F. B.. "Acute Uric Acid Nephropathy." In *Primer on Kidney Diseases*. Edited by A. Greenberg and A. K. Cheung. China: Saunders, 2005. 301-303.

97. Peters, J. L., L. H. Miner, A. C. Michael, and S. R. Sesack. "Ultrastructure of carbon fiber microelectrode implantation sites after acute voltammetric measurements in the striatum of anesthetized rats." *Journal of Neuroscience Methods* 137, no. 1 (2004): 9-23.

98. Wightman, R. M. et. al.. "Real-time characterization of dopamine overflow and uptake in the rat striatum." *Neuroscience* 25, no. 2 (1988): 513-523.

99. Wang, S., Q. Xu, and G. Liub. "Differential Pulse Voltammetric Determination of Uric Acid on Carbon-Coated Iron Nanoparticle Modified Glassy Carbon Electrodes." *Electroanalysis* 20, no. 10 (2008): 1116-1120.

100. Bachmann, P. K.. "Plasma CVD techniques for low pressure synthesis of diamond: an overview." In *Properties and Growth of Diamond (E M I S Datareviews Series)*. Edited by J. Davies. Stevenage, U.K.: Institution of Electrical Engineers, 1994. 349-353.

101. Bachmann, P. K.. "Plasma CVD synthesis of diamond." In *Properties and Growth of Diamond (E M I S Datareviews Series)*. Edited by J. Davies. Stevenage, U.K.: Institution of Electrical Engineers, 1994. 354-363.

102. Liu, H., and David S. Dandy. *Diamond Chemical Vapor Deposition, Nucleation and Early Growth Stages*. New Jersey: Noyes Publications, 1996.

103. Ivandini, T. A., Y. Einaga, K. Honda, and A. Fujishima. "Preparation and Characterization of Poly crystalline Chemical Vapor Deposited Boron-doped Diamond Thin Films." In *Diamond Electrochemistry*. Edited by A. Fujishima, et.al..UK: Elsevier Science, 2005. 11-25.

104. Ascarelli, P. , and S. Fontana. "Dissimilar Grit Size Dependence of the Diamond Nucleation Density on Substrate Surface Pretreatments." *Applied Surface Science* 64 (1993): 307-311.

105. May, Paul W.. "Diamond thin films: a 21st-century material." *Philosophical Transactions of the Royal Society A* 358 (2000): 473-495.

106. Pierson, H. O.. "CVD Diamond." In *Handbook of Carbon, Graphite, Diamond and Fullerenes: Properties, Processing and Applications*. New Jersey: Noyes Publications, 1993. 302-336.

107.Martin, H. B., S. C. Eaton, U. Landau, and J. C. Angus. "Electrochemical Effects on Diamond Surfaces: Wide Potential Window, Reactivity, Spectroscopy, Doping Levels and Surface Conductivity." In *Diamond Electrochemistry*. Edited by A. Fujishima, et.al..UK: Elsevier Science, 2005. 26-50.

108. Pehrsson, Pehr E., Frances G. Celii, and James E. Butler. "Chemical Mechanisms of Diamond CVD." In *Diamond Films and Coatings: Development, Properties and Applications (Materials Science and Process Technology Series)*. Edited by Robert F. David. New Jersey: Noyes Publication, 1993. 68-146.

109. Prawer, Steven , and Robert J. Nemanich. "Raman spectroscopy of diamond and doped diamond." *Philosophical Transactions of the Royal Society A* 362 (2004): 2537-2565.

110. Pickard, D.. "Crystalline quality assessment in diamond by micro-Raman spectroscopy." In *Properties, Growth and Applications of Diamond.* London: INSPEC, 2001. 66-70.

111. Filik, Jacob. "Raman spectroscopy: a simple, non-destructive way to characterize diamond and diamond-like materials." *Spectroscopy Europe* 17, no. 5 (2005): 10-17.

112. Ferrari, Andrea Carlo , and John Robertson. "Raman spectroscopy of amorphous, nanostructured, diamond-like carbon, and nanodiamond." *Philosophical Transactions of the Royal Society A* 362 (2004): 2477-2512.

113. Ferrari, A. C., and J. Robertson. "Interpretation of Raman spectra of disordered and amorphous carbon." *Physical Review B* 61 (2000): 14095–14107.

114. Castiglioni, Chiara , Matteo Tommasini, and Giuseppe Zerbi. "Raman spectroscopy of polyconjugated molecules and materials: confinement effect in one and two dimensions." *Philosophical Transactions of the Royal Society A* 362 (2004): 2425-2459.

115. Raina, S., W. P. Kang, and J. L. Davidson. "Nanodiamond film with 'ridge' surface profile for chemical sensing." *Diamond and Related Materials* 17 (2008): 896-899.

116. Zhu, Wei, Hua-Shuang Kong, and Jeffrey T Glass. "Characterization of Diamond Films." In *Diamond Films and Coatings: Development, Properties and Applications (Materials Science and Process Technology Series)*.Edited by Robert F. David. New Jersey: Noyes Publication, 1993. 244-338.

117. Raina, S., X. C. LeQuan, W. P. Kang, and J. L. Davidson. "Effect of Nitrogen Concentration on Nanodiamond Film Characteristics for Electrode Application." *ECS Transactions* 19, no. 21 (2009): 23-35.

118. McFeely, F. R. et. al.. "X-ray photoemission studies of diamond, graphite, and glassy carbon valence bands." *Physical Review B* 9, no. 12 (1974): 5268-5278.

119. Choi, B. G. et. al.. "Effect of the addition of nitrogen gas and annealing on the electrical properties of DLC films deposited by radio frequency plasma enhanced chemical vapor deposition (RF-PECVD)." *Journal of Ceramic Processing Research* 8, no. 6 (2007): 411-416.

120. Snis, A., and S. F. Matar. "Core ionization energies of carbon–nitrogen molecules and solids." *Journal of Chemical Physics* 111, no. 21 (1999): 9678-9686.

121. Smith, T. J., and K. J. Stevenson. "Reference Electrodes." In *Handbook of Electrochemistry*. Edited by Cynthia G. Zoski.Amsterdam: Elsevier, 2007. 73-110.

122. Wang, J.. "Fundamental Concepts." In *Analytical Electrochemistry*. 2nd ed. New York: Wiley-VCH, 2001. 1-27.

123. Notsu, H., T. Tatsuma, and A. Fujishima. "Characterization of oxygenated diamond." In *Diamond Electrochemistry*. Edited by A. Fujishima, et.al..UK: Elsevier, 2005. 218-237.

124. Norouzi, P., F. Faridbod, E. Nasali-Esfahani, B. Larijani, and M. R. Ganjali. "Cholesterol Biosensor Based on MWCNTs-MnO2 Nanoparticles Using FFT Continuous Cyclic Voltammetry." *International Journal of Electrochemical Science* 5 (2010): 1008-1017.

125. Granger, M. C. et.al.. "Standard Electrochemical Behavior of High-Quality, Boron-Doped Polycrystalline Diamond Thin-Film Electrodes." *Analytical Chemistry* 72 (2000): 3793-3804.

126. Goyal, R. N., A. Brajter-Toth, and G. Dryhurst. "Further insights into the electrochemical oxidation of uric acid." *Journal of Electroanalytical Chemistry* 131 (1982): 181-202.

127. Chen, T. R., and G. Dryhurst. "The second voltammetric oxidation peak of 7,9-dimethyl uric acid." *Journal of Electroanalytical Chemistry* 144 (1983): 191-206.

128. Dryhurst, G. et. al.. "Elucidation of the Biological Redox Chemistry of Purines Using Electrochemical Techniques." *Journal of Chemical Education* 60, no. 4 (1983): 315-319.

129. Pleskov, Y. V., M. D. Krotova, A. V. Saveliev, and V. G. Ralchenko. "The effects of nitrogenation on the electrochemical properties of nanocrystalline diamond films." *Diamond and Related Materials* 16 (2007): 2114-2117.

130. Ma, K. L. et. al.. "Electrical properties of nitrogen incorporated nanocrystalline diamond films." *Diamond and Related Materials* 15 (2006): 626-630.

131. Liu, Y. K. et. al.. "Structural and electrical properties of nanocrystalline diamond (NCD) heavily doped by nitrogen." *Diamond and Related Materials* 15 (2005): 2059-2063.

132. Liu, Y. K. et. al.. "Structural and electrical properties of nanocrystalline diamond (NCD) heavily doped by nitrogen." *Diamond and Related Materials* 15 (2005): 2059-2063.

133. Bhattacharyya, S. et. al.. "Synthesis and characterization of highly-conducting nitrogen-doped ultrananocrystalline diamond films." *Applied Physics Letters* 79 (2001): 1441-1443.

134. Chen, Q. et. al.. "The Structure and Electrochemical Behavior of Nitrogen-Containing Nanocrystalline Diamond Films Deposited from $CH_4/N_2/Ar$ Mixtures." *Journal of Electrochemical Society* 148 (2001): E44-E51.

135. Bhattacharyya, S., C. Cardinaud, and G. Turban. "Spectroscopic determination of the structure of amorphous nitrogenated carbon films." *Journal of Applied Physics* 83, no. 8 (1998): 4491-4500.

136. Snis, A., and S. F. Matar. "Electronic density of states, 1s core-level shifts, and core ionization energies of graphite, diamond, C_3N_4 phases, and graphitic $C_{11}N_4$." *Physical Review B* 60, no. 15 (1999): 10855-10863.

137. Badzian, A., T. Badzian, and S. Lee. "Synthesis of diamond from methane and nitrogen mixture." *Applied Physics Letters* 62, no. 26 (1993): 3432-3434.

138. Hwang, M., and C. Lee. "Effects of oxygen and nitrogen addition on the optical properties of diamond-like carbon films ." *Materials Science and Engineering B* 75, no. 1 (2000): 24-28.

139. Morf, W. E.. "Theoretical treatment of the amperometric current response of multiple microelectrode arrays." *Analytica Chimica Acta* 330 (1996): 139-149.

140. Morf, W. E., and N. F. de Rooij. "Performance of amperometric sensors based on multiple microelectrode arrays." *Sensors and Actuators B* 44 (1997): 538-541.

141. Xie, X. et. al.. "Development of an ultramicroelectrode arrays (UMEAs) sensor for trace heavy metal measurement in water." *Sensors and Actuators B* 97 (2004): 168-173.

142. Sarada, B. V., T. N. Rao, D. A. Tryk, and A. Fujishima. "Electrochemical Characterization of Highly Boron-Doped Diamond Microelectrodes in Aqueous Electrolyte." *Journal of the Electrochemical Society* 146, no. 4 (1999): 1469-1471.

143. Raina, S., W. P. Kang, J. L. Davidson, and J. H. Huang. "Electrochemical Biosensor Utilizing Nitrogen Incorporated Nanodiamond Ultra-Microelectrode Array." *ECS Transactions* 28, no. 34 (2010): 21-28.

144. Zachek, M. K., J. Park, P. Takmakov, R. M. Wightman, and G. S. McCarty. "Microfabricated FSCV-compatible microelectrode array for real-time monitoring of heterogeneous dopamine release." *Analyst* 135 (2010): 1556-1563.

145. Heien, M. L. A. V., M. A. Johnson, and R. M. Wightman. "Resolving Neurotransmitters Detected by Fast-Scan Cyclic Voltammetry." *Analytical Chemistry* 76 (2004): 5697-5704.

146. Hafizi, S., Z. L. Kruk, and J. A. Stamford. "Fast cyclic voltammetry: improved sensitivity to dopamine with extended oxidation scan limits." *Journal of Neuroscience Methods* 33 (1990): 41-49.

147. Zachek, M. K., A. Hermans, R. M. Wightman, and G. S. McCarty. "Electrochemical dopamine detection: Comparing gold and carbon fiber microelectrodes using background subtracted fast scan cyclic voltammetry ." *Journal of Electroanalytical Chemistry* 614 (2008): 113-120.

148. Hermans, A. et. al.. "Dopamine Detection with Fast-Scan Cyclic Voltammetry Used with Analog Background Subtraction." *Analytical Chemistry* 80 (2008): 4040-4048.

149. Bard, A. J., and L. R. Faulkner. "Electroactive Layers and Modified Electrodes." In *Electrochemical Methods: Fundamentals and Applications*. 2 ed. New York: Wiley, 2001. 580-631.

150. Keithley, R. B. et. al.. "Higher Sensitivity Dopamine Measurements with Faster-Scan Cyclic Voltammetry." *Analytical Chemistry* 83 (2011): 3563-3571.

151. Koehne, J. E. et. al.. "Carbon nanofiber electrode array for electrochemical detection of dopamine using fast scan cyclic voltammetry." *Analyst* 136 (2011): 1802-1805.

152. Soh, K. L. et. al.. "Diamond Ultramicroelectrode Chemical Sensing Arrays." *IEEE SENSORS* (2006): 2009-2015.

153. Zang, J. B., Y. H. Wang, S. Z. Zhao, L. Y. Bian, and J. Lu. "Electrochemical properties of nanodiamond powder electrodes." *Diamond and Related Materials* 16 (2007): 16-20.

154. Salimi, A., H. Mamkhezri, and R. Hallaj. "Simultaneous determination of ascorbic acid, uric acid andneurotransmitters with a carbon ceramic electrode prepared by sol–gel technique." *Talanta* 70 (2006): 823-832.

155. Einaga, Y., and A. Fujishima. "Applications of Polycrystalline and Modified Functional Diamond Electrodes." In *Synthetic Diamond Films Preparation, Electrochemistry, Characterization, and Applications*. Hoboken, New Jersey: John Wiley and Sons, 2011. 109-132.

156. Fujishima, A. et. al.. "Electroanalysis of dopamine and NADH at conductive diamond electrodes." *Journal of Electroanalytical Chemistry* 473 (1999): 179-185.

157. Burmeister, J. J., K. Moxon, and G. A. Gerhardt. "Ceramic-Based Multisite Microelectrodes for Electrochemical Recordings." *Analytical Chemistry* 72 (2000): 187-192.

158. Zhou, Y. L., R. H. Tian, and J. F. Zhi. "Amperometric biosensor based on tyrosinase immobilized on a boron-doped diamond electrode." *Biosensors and Bioelectronics* 22 (2007): 822-828.

159. Kondoa, T. et. al.. "Enhanced electrochemical response in oxidative differential pulse voltammetry of dopamine in the presence of ascorbic acid at carboxyl-terminated boron-doped diamond electrodes." *Electrochimica Acta* 54 (2009): 2312-2319.